UNIVERSITY OF CALIFORNIA
RIVERSIDE

Engineering Responsiveness in Nanostructured Materials

A Dissertation submitted in partial satisfaction
of the requirements for the degree of

Doctor of Philosophy

in

Chemistry

by

Rashed Mohammad Aleisa

September 2020

Dissertation Committee:
Dr. Yadong Yin, Chairperson
Dr. Pingyun Feng
Dr. De-en Jiang

The Dissertation of Rashed Mohammad Aleisa is approved:

Committee Chairperson

University of California, Riverside

Acknowledgments

I would like to express first my profound gratitude to my advisor, Prof. Yadong Yin. Without his guiding and help, I wouldn't complete my Ph.D. After these five years, I become amazed at how much he cares about his students' future success. His passion and love for chemistry have opened my eyes to pursue a career in research. He directed us to explore research in a way that led us to think differently and creatively. He taught us to be always self-independent and take the original approach when solving problems, which are the essential skills for being a world-class researcher. I am also very thankful to my other committee members, Prof. Pingyun Feng, and Prof. De-en Jiang, for their time and valuable insights during my Ph.D. tenure.

I am also grateful to all my lab colleagues for all their help and collaborations: Dr. Ji Feng, Dr. Yaocai Bai, Dr. Jinxing Chen, Dr. Wenshou Wang, Dr. Wenjing Xu, Dr. Xiaojing Wang, Dr. Zhiwei Li, Fan Yang, Rui Li, Qingsong Fan, Chaolumeng Wu, Ye Zuyang, Chen Chen, Zepeng Cai, Dr. Dilong Liu, Xin Chen, Bo Jiang, Fenglian Qi, Lan Peng, Wenwen Yin, Dr. Yongqing Wang, Dr. Aiwei Tang, Dr. Dawei Wang, Dr. Shichuan Li, Dr. Aiqin Gao, Dr. Panpan Xu, Bo Li, Xiaojun Zeng, et. al. I also would like to thank the undergraduate and high school students who have worked with me: Laura Noronha, Christopher Taitano, and Xiang Zhao. I am very grateful to all my friends at UCR for all the great times and assistance during my study.

I would also like to express my gratitude to Prof. Francisco Zaera and Dr. Ilkeun Lee for their great help during my work in their lab. I would like to thank Dr. Krassimir N. Bozhilov, Dr. Mathias Rommelfanger, and Dr. Michael Pigeon for their assistance in

the CFAMM facilities. I also want to thank Dr. Jinghua Guo and Dr. Feipeng Yang in Lawrence Berkeley National Laboratory for their help in conducting the EXAFS analysis. I would also like to thank Dr. Kevin Simpson for his guidance during my TA teaching.

I am also incredibly thankful to Saudi Aramco for its financial support and assistance. Without their support, I would not reach this great achievement in my life.

Last but not least, I express my most profound appreciation for my family, my parents, my sisters, and my brothers, for all the things they did to me during the years that made me become who I am.

Most importantly, I would like to express my gratitude to my beloved wife, Ameera Albakr. She was the one who stood by me during my lows. She is the one that always reminds me of the light at the end of the tunnel. Without her, I would not finally write this acknowledgment.

Dedication

To Mohammad, Tameem, and Tala.

ABSTRACT OF THE DISSERTATION

Engineering Responsiveness in Nanostructured Materials

by

Rashed Mohammad Aleisa

Doctor of Philosophy, Graduate Program in Chemistry
University of California, Riverside, September 2020
Dr. Yadong Yin, Chairperson

Stimuli-responsive nanomaterials are engineered nanostructures that change their properties in response to external stimuli, such as mechanical stress, electric and magnetic fields, temperature, and light. They have potential applications in sensors, actuators, smart windows, optical devices, and drug delivery. Introducing responsive features into nanomaterials requires advanced synthetic and post-synthetic techniques such as structural engineering, ligand functionalization, chemical vapor deposition, and self-assembly. These methods are usually time-consuming, materials-specific, and lacking the controllability and rational-design of specific responsive-functionality. This dissertation discusses different strategies of responsiveness-engineering unrestricted to the nature of the nanomaterials comprising rationally-designed colloidal synthetic approaches.

The dissertation starts with introducing the development of a rapid, reversible, and stable light-responsive system based on nitrogen-doped titanium dioxide (N-TiO_2) nanocrystals. The synthetic method involves TiO_2 structural engineering through nitrogen doping in a hydrolysis reaction and *in-situ* surface functionalization with organic glycols

acting as sacrificial electron donors (SEDs). The photoreversible system showed excellent color-switching from white to black under light irradiation, corresponding to the surface self-reduction of Ti(IV) to Ti(III). Nitrogen doping and surface functionalization accelerated and stabilized the system responsive-coloration. This system was implemented as a rewritable paper showing a reversible color-switching that could retain writing for hours in ambient conditions without the need for redox dyes or chromic polymers. This functionalization strategy possesses vital advantages in its low cost, rapid response, and excellent reversibility and stability, that could be applied to several photo-responsive systems.

In the second part, a rational-design strategy of synthesizing mechanically-responsive Au@Ag@void@TiO_2 nanoparticles to fabricate a colorimetric stress sensor is introduced. The sensor changes color from yellow to dark orange/red under a mechanical force based on the deformation of the nanoparticles. The color-changing mechanism consists of shifting the plasmonic absorption of Au@Ag@void@TiO_2 by changing the surrounding environment of Au@Ag nanostructures from air to TiO_2 after deforming the outer particle shell by a mechanical force. The pressure sensor could be applied to static and impact forces, showing potentials as instantaneous impact detectors in sports and bicycle helmets, sports mouth guards, and automobile crash dummies. Increasing the thickness of the TiO_2 outer shell enhanced the mechanical strength of the materials, thereby withstanding different pressure thresholds directly correlated with shell thickness. This pre-designed synthetic approach could be employed in the future developments of smart materials.

Finally, the development of a universal magnetizing method of nanomaterials utilizing amorphous molybdenum sulfide (a-MoS_x) as a transitional layer to anchor magnetic iron oxide particles is presented. The underlying mechanism relies on the strong bonding between molybdenum sulfide and iron oxide nanoparticles, which is found to occur through (Mo-O) interaction. The applicability and versatility of the magnetizing technique are endowed by developing a colloidal coating method of a-MoS_x on silicon dioxide (SiO_2) that could be induced on various nanostructured materials. The colloidal coating method consists of SiO_2 surface modification with (3-aminopropyl)triethoxysilane (APTES), followed by the acidification of $(NH_4)_2MoS_4$ to produce APTES-SiO_2@a-MoS_x nanostructures. The instantaneous attachment of iron oxide nanoparticles on APTES-SiO_2@a-MoS_x could be achieved by mixing both materials in polar solvents. The practicality and advantage of this technique were demonstrated by magnetizing Au microplates to fabricate a magnetically-tunable micromirror. The versatility, practicality, rapid functionalization, and low toxicity are crucial advantages in introducing magnetic-responsiveness in nanostructured materials, especially for biomedical applications.

Table of Contents

List of Figures

Chapter 1. Introduction to Stimuli-Responsive Nanomaterials

1.1 Introduction

Stimuli-responsive nanomaterials are nanostructured materials that can change their mechanical (e.g., stiffness), thermal, optical, or electromagnetic properties in response to external stimuli.[1] These switchable smart materials are abundant in nature. Cuttlefish, a subclass of cephalopods, performs camouflage as they alter their body patterns and colors in response to surrounding environmental changes, through a neurally driven chromatophore apparatus.[2] Examples of external inputs include mechanical forces (stress, strain, pressure), physical and environmental changes (light, temperature, sound), chemical changes (pH, surface charges, concentration), and electromagnetic stimuli (electrical and magnetic field). These various responses, which also include thermal, optical, or electromagnetic responses, provide excellent tunability of materials engineering to meet new demands of applications.[3]

Among the most studied stimuli-responsive nanomaterials are optically, mechanically, and magnetically-responsive ones. A variety of optically responsive nanomaterials display color changes in response to light energy. In particular, light-responsive color-switching redox-driven inorganic/organic hybrid system showed great promise for applications such as rewritable paper, smart windows, and display devices. These systems are mainly based on combining a large band gap semiconductor nanomaterial that can absorb light energy when the absorbed energy is equal or greater than its band gap, and a chromic organic molecule than can change color in its reduced and oxidized states. In contrast to single organic redox systems, engineering inorganic

materials and redox molecules into hybrid systems has recently demonstrated significant advantages in terms of high coloration efficiency, fast response time, excellent reversibility and life-span, and high contrast ratio.[4–8]

Nevertheless, mechano-responsive materials are not widely exploited as other stimulants-responsive ones, which is in contrast to the diverse mechano-responsive systems found in nature.[9–11] Specifically, mechanochromic materials have attracted considerable attention in areas such as sensors, color display, and solid-state luminescence. These materials absorb or fluorescence color when deforming in response to mechanical stress. Such a mechanism is exceedingly useful in in-situ sensing of material failure due to stress fracture or fatigue.[12] They also could be useful for detecting impact forces in many safety gears such as bicycle helmets and sport mouthguards.

Magnetically responsive materials are the most widely studied among all stimuli-responsive materials owing to the significant progress in synthesizing magnetic nanoparticles or nanostructures with controllable sizes, shapes, and magnetic properties. Magnetic force can orient ordered anisotropic structures or induce order within assembled structures with precise control over crystal symmetry or lattice constant. The magnetic particles can be synthesized through direct chemical approaches, post-treatment methods, or attachments to functionalized particles. Various applications have been demonstrated for magnetically-responsive nanomaterials, including photonic crystals, soft robotics, actuators, smart windows, and display devices.[13–15]

In this chapter, an overview of optically, mechanically, and magnetically-responsive nanomaterials will be discussed. Firstly, optically-responsive nanomaterials will be introduced while focusing on the mechanism and applications of redox-driven color-switching hybrid systems. We will discuss next the fundamentals and applications of mechanochromic materials with the emphasis on their applications in pressure sensing. Finally, magnetically-responsive nanomaterials will be discussed while focusing on their synthetic protocols and potential applications. The scope of this dissertation will be outlined at the end of this chapter.

1.2 Light-responsive nanomaterials

1.2.1 Redox driven color-switching of organic-inorganic hybrid systems (RCHS)

Chromism defines as the ability of a material to switch color under external stimuli reversibly.[16,17] This property, when combined with excellent controllability and rapid response, provides a wide range of technological opportunities for human needs. Previous commercial exploitation of this phenomenon resulted in few successful developments of thermal printers, battery testers, and color-changing lenses that darkened upon sunlight exposure. Nevertheless, there are still great potentials for this technology. Developing a dynamic display device for computer screens and flat-panel television and smart windows/textiles materials are just a few examples. However, the main limitations of such systems are their long duration in achieving coloration and decoloration, poor lifespan, and low contrast.[4,5,16,18,19]

Chromism usually induces through a change in the electron states of a molecule, often in the π- or d-electron state- by an electron-transfer (redox) process. Several

inorganic compounds and organic molecules possess this property. The presence of mixed redox states of the metallic center in inorganic compounds such as WO_3, V_2O_5, MoO_3, IrO_2, and Co_2O_3 are responsible for this reversible color-switching property.[18] Although they usually have good stability under visible and UV light, the rates of their coloration and bleaching are slow, yielding color display devices with switching times of the order of tens of seconds. They also require high processing costs and tedious fabrication procedures such as sputtering and film control techniques. They also, by nature, are non-flexible materials, presenting a substantial obstacle for implementation in flexible devices or textiles.[4,18,20,21] On the other hand, organic compounds such as viologens, a well-known class of redox chromophore, endow rapid coloration and bleaching performance, and good cyclability and reversibility. Nevertheless, they suffer from bad contrast, attributed to the insufficient electron transfer that initiates the redox (coloring/bleaching) mechanism.[4,20,21]

One method to overcome the current limitations of redox color-switching materials is to combine both organic and inorganic components into a one color-switchable hybrid system. This more logical approach will integrate the unique features of both materials into one system.[6,8,30,22–29] RCHS consist of redox organic molecules and inorganic materials. The redox organic molecules are usually chromophores, while the functionality of the inorganic materials is to enhance the system performance, such as increasing electrons transfer efficiency or introducing stimuli-active features.[5,6,8,25] For instance, inorganic molecules contain a higher surface area and maintain faster electron movement (i.e., better conductivity). The electrons transfer from the inorganic

compounds into the organic species, prompting the redox reactions and the coloration process. RCHS maintains better coloration efficiency, color-switching cyclability, and recyclability.[4,7,8,20,21,31] The higher contrast is achieved because the inorganic components absorb a great number of organic molecules through its high surface area.[4,5,20,21,31]

Inorganic materials and organic molecules are predominantly in physical contact through an interface (Figure 1.1). In most cases, organic molecules are absorbed onto the surfaces of the inorganic materials. These redox chromophores exhibit two or more redox states with distinct electronic absorption spectra, which arise from an intervalence optical charge transfer in which different oxidations states are available.[16] The underlying mechanism relays on providing electrons on the inorganic components through external stimuli such as light and electrical voltages. These electrons will transfer into the redox organic molecules through the interface (Figure 1.1).

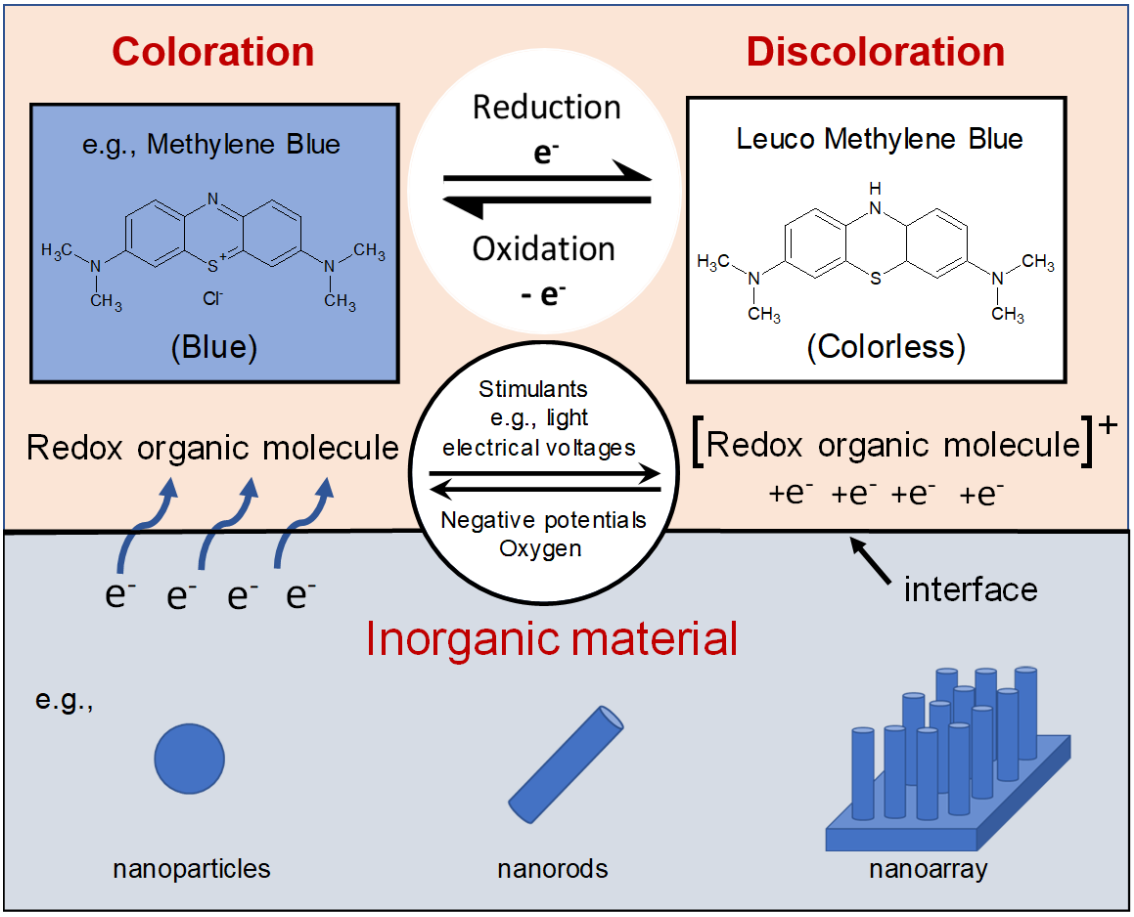

Figure 1.1 Schematic representation of components, mechanism, and structures of redox-driven color-switchable organic-inorganic hybrid systems.

A reduction reaction of the organic component will occur, leading to the system coloration. A reversible oxidation reaction of the chromophore through either oxygen molecules or negative applied potentials will generate the discoloration process. This mechanism is reversible and could be repeated for several cycles. Examples of organic molecules that exhibit two or more coloration states (oxidation) include viologens, polyaniline (PANI), polypyrroles, and poly(3,4-ethylene dioxythiophene) (PEDOTs).[19,32–36] Most exploited inorganic components in RCHs are semiconductor materials that can generate electrons in their conduction band or conductive material, such as WO_3, NiO, TiO_2, and SnO_2.[35,37] The inorganic materials could be synthesized with various nanostructures including nanoparticles [21,38], nanocrystals [39,40], nanorods [41,42], and nanowires [43].

1.2.2 Photocatalytic RCHS

Photocatalytic RCHS are systems that undergo reduction (i.e., coloration) through photocatalytic reactions (in the visible and UV light regions) and reversibly oxidized by oxygen molecules (i.e., decoloration).[4,25,26,29,39,44] The complete process is summarized in Figure 1.2. Photocatalytic semiconductor materials absorb light energy if their bandgap energy is equal or less than the energy of irradiated light. When excited, they produce electrons in their conduction band and electron holes in their valence band. In RCHS, the photo-generated electrons in the inorganic material's conduction band will reduce the organic molecules into its reduced state, producing the coloration of the system. However, these colored states are usually less efficient because of the much rapid recombination of generated electrons and holes. Sacrificial electron donor (SED)

molecules are usually used to scavenge the generated holes during the excitation step. Examples of SEDs include aliphatic amines, aromatic amines, ascorbic acid, carboxylic acids, thiols, and others.[45] Adding methanol, for example, as an electron donor to react irreversibly with the photogenerated valence band (VB) holes, can enhance the photocatalytic electron/hole separation efficiency. However, the yield of H_2 can be subsequently reduced by competing reduction reactions with the products formed upon the oxidation of the sacrificial reagents.[45] Because electron donors are consumed in the photocatalytic reaction, their continuous addition is required to sustain RCHS performance, or the degradation of the photo-RCHS performance will decrease eventually.[45] The reversible decoloration process, in this case, will occur mainly by the oxygen molecules in the atmosphere, which is also subjected to the concentration of the oxygen and surrounding temperature.

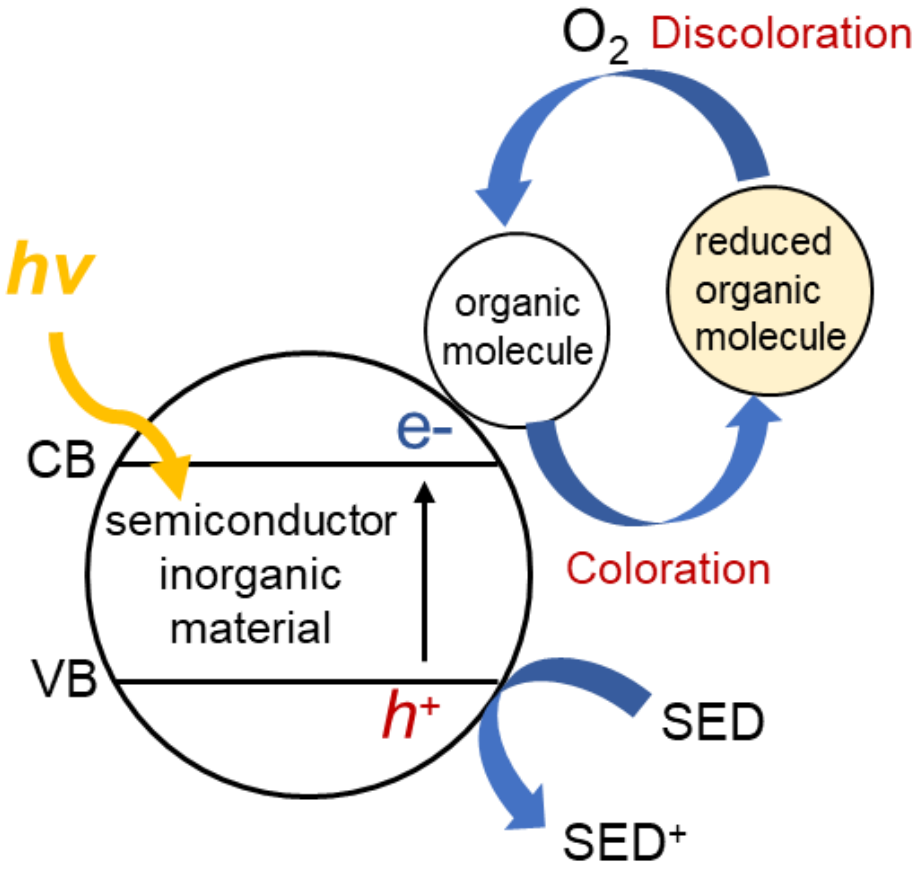

Figure 1.2 Primary strategy of photocatalytic redox-driven color-switchable hybrid systems under light irradiation in which sacrificial electron donors are incorporated.

1.2.3 Applications in rewritable papers

A new type of photoreversible color switching system was developed by using photo-reductive semiconductor nanoparticles to initiate photocatalytic redox reactions of methylene blue (MB).[46] As a typical heterocyclic redox dye, MB can switch from bright blue color in its oxidized form to colorless MB (LMB) upon reduction, and then revert to the initial blue MB upon oxidation. Semiconductor nanoparticles, such as titanium dioxide (TiO_2), have been extensively studied as photocatalysis for selective oxidation/reduction in degradation of organic pollutants and water splitting. The key to the design of the proposed photoreversible color switching system is to endow TiO_2 nanoparticles' photo-reductive activity to drive photocatalytic color-switching upon UV illumination. Two strategies have been developed in these systems: (i) binding capping ligands or/and (ii) creating oxygen vacancies in TiO_2 nanoparticles as efficient SEDs to scavenge the photogenerated holes, thus ensuring the survived photogenerated electrons to reduce the redox dyes. By using diethylene glycol (DEG) as a model SED, the authors demonstrated that it's binding to the TiO_2 nanoparticles' surface significantly enhances the nanoparticles photo-reductive activity (Figure 1.3a).[47] Upon UV illumination, the photogenerated holes will be captured by the surface-bounded DEG moieties to produce alkoxy radicals, which can be further oxidized to aldehydes. Nucleophilic attack of water will take place to recover the active sites and release the oxidized SEDs.[46,48–51]

In order to increase the photo-reductive activity, a polymeric capping ligand (i.e., poly(ethylene glycol)-b-poly(propylene glycol)-b-poly(ethylene glycol) (P123)) was introduced into the synthetic procedure of the TiO_2 nanoparticles to enhance their hole

scavenging capability. Anatase phased TiO_2 nanoparticles with small sizes (several nanometers) were obtained, as shown in Figure 1.3b. The Fourier transform infrared (FT-IR) spectrum of the TiO_2 nanoparticles illustrated that abundant hydroxyl groups derived from P123 and glycolate species were successfully bonded onto the surface of the nanoparticles. Upon UV illumination, the blue color of the aqueous dispersion of TiO_2/MB/H_2O switched to colorless in 10s. The colorless dispersion of TiO_2/LMB/H_2O switched back to blue color naturally in the ambient conditions through oxidation by oxygen molecules. Interestingly, the recovered blue color of the colorless dispersion could be accelerated into 15 min by using visible light illumination in ambient conditions.[46] Owing to the enhanced photo-reductive activity by abundant hydroxyl groups, the dispersion of TiO_2/LMB/H_2O could be cycled for about 11 times upon repeated UV and visible light illumination (Figure 1.3b).

As demonstrated in Figure 1.3a, the surface bonded-SEDs can gradually be consumed by the photogenerated holes, resulting in limited cycling properties of the TiO_2/MB/H_2O system. A new strategy was developed, therefore, based on utilizing oxygen vacancies in TiO2 to serve as internal SEDs. A highly efficient photocatalytic color switching of MB was realized by using Ba^{2+}-doped TiO_2 nanoparticles incorporating abundant oxygen vacancies. Anatase phased Ba^{2+}-doped TiO_2 nanoparticles with sizes of 3-10 nm were synthesized by colloidal hydrolysis reaction. Both the energy-dispersive X-ray spectroscopy and X-ray photoelectron spectroscopy (XPS) results demonstrated that Ba2+ ions were successfully doped in TiO2 nanoparticles with an atomic ratio of 1.2 at%, indicating the existence of oxygen

vacancies to preserve charge neutrality.[51] The X-ray absorption near-edge spectra (XANES) of O K-edge of Ba^{2+}-doped TiO_2 nanoparticles with different UV irradiation time were investigated to confirm the existence of oxygen vacancies further. The relative intensity of t_{2g} and e_g peaks gradually increased with increasing UV irradiation time (Figure 1.3c). The changes in O K-edge spectra indicated an enhancement of the transitions from O 1s orbital to the hybridized orbitals of O 2p and Ti 3d, which is attributed to the reduced amount of oxygen vacancies in Ba^{2+}-doped TiO_2 nanoparticles, indicating the oxidation of TiO_2 nanoparticles upon UV illumination. Therefore, the oxygen vacancies in the Ba^{2+}-doped TiO_2 nanoparticles scavenged the photogenerated holes and thus enhanced the transitions from O 1s orbital to the hybridized orbital between O 2p and Ti 3d during UV irradiation. The oxygen vacancies created in Ba^{2+}-doped TiO_2 nanoparticles are superior to TiO_2 nanoparticles bounded with hydroxyl groups. The Ba^{2+}-doped TiO_2 nanoparticles/MB/H_2O system exhibited excellent color-switching properties: the blue color disappeared in a short period of (10s) upon UV illumination and switched back in ~ 2.5 min upon visible light irradiation, and more importantly, the system could reversibly switch color for more than 45 cycles (Figure 1.3c). Ba^{2+} doping could blue shift the absorption of TiO_2 nanoparticles (about 16 nm), effectively repressing the partial reduction of MB to LMB under visible light irradiation, leading to a higher recoloration rate (2.5 min) than undoped system (15 min).[51]

Although the TiO_2/MB/H_2O system has significant advantages in rapid photo-response, excellent repeatability, non-toxicity, and low cost, the reliance on UV light to drive color-switching might burden its applications where UV light has detrimental

effects. Therefore, visible-light-responsive color-switching systems are more desirable because visible-light possesses far less damaging to organic molecules and comprises a large portion of the solar spectrum. A self-doping strategy to shift the absorption bands of SnO_{2-x} nanoparticles to the visible region and simultaneously produce oxygen vacancies to act as SEDs was developed by self-doping SnO_2 nanoparticles (Figure 1.3d). SnO_{2-x} nanoparticles self-doped with Sn^{2+} with sizes of 5-10 nm were synthesized by a solvothermal reaction using Sn powder and $SnCl_4$ as precursors. The decreased binding energy of Sn 3d of Sn^{2+} in SnO_{2-x} nanoparticles was attributed to the formation of oxygen vacancies to preserve charge neutrality. The SnO_{2-x} nanoparticles showed strong absorption from UV to the visible region because of the oxygen vacancies, while the undoped SnO2 nanoparticles showed absorption in the UV region (Figure 1.3b).

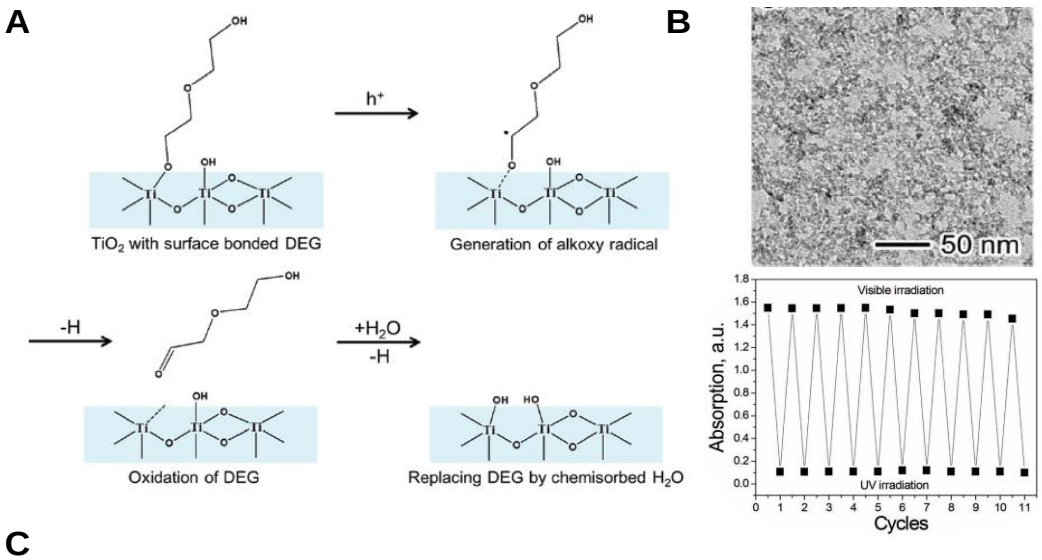
A
h+
TiO2 with surface bonded DEG
Generation of alkoxy radical
-H
+H2O
-H
Oxidation of DEG
Replacing DEG by chemisorbed H2O
B
50 nm
Visible irradiation
UV irradiation
Absorption, a.u.
Cycles

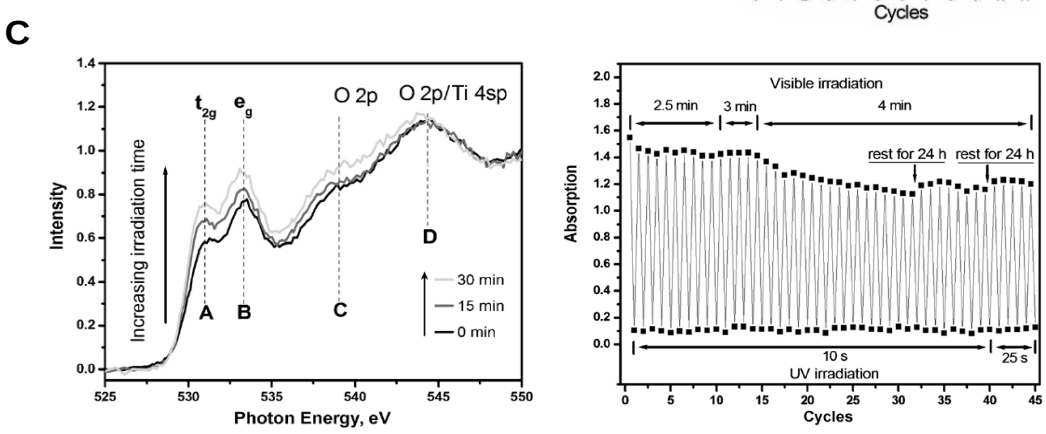
C
Intensity
Increasing irradiation time
t2g
eg
O 2p
O 2p/Ti 4sp
A
B
C
D
30 min
15 min
0 min
Photon Energy, eV
Visible irradiation
2.5 min
3 min
4 min
rest for 24 h
rest for 24 h
Absorption
10 s
25 s
UV irradiation
Cycles

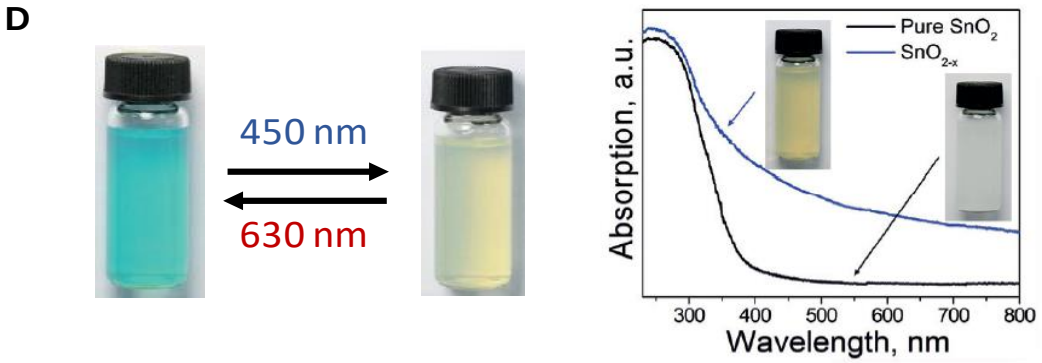
D
450 nm
630 nm
Pure SnO2
SnO2-x
Absorption, a.u.
Wavelength, nm

Figure 1.3 (a) Schematic mechanism of TiO_2 surface bounded with DEG molecules upon UV irradiation. It was adapted with permission from ref. 47 and 39. (b) TEM image of TiO_2 nanocrystals and the overall performance of TiO_2/MB/H_2O system under repeated cycles of visible and UV light irradiations. (c) XANES spectra of the O K-edge of Ba-doped TiO_2 nanocrystals with increasing irradiation time in vacuum and absorption intensity at 660 nm of Ba-doped TiO_2/MB/H_2O under UV and visible light irradiations for 45 cycles. Adapted with permission from ref. 26. (d) Digital images of SnO_{2-x}/MB/H_2O aqueous mixtures upon illumination with blue and red-light sources and the UV/vis spectra of SnO_{2-x} and SnO_2 nanocrystals solutions. Adapted with permission from ref. 40.

These oxygen vacancies act as effective SEDs to scavenge photogenerated holes during visible light irradiation, enabling excellent color switching of redox dyes. The blue color of the SnO_{2-x} nanoparticles/MB/H2O system disappeared rapidly in 10 s upon blue light (λ = 450 nm) irradiation and switched back in 3 min upon red light (λ = 630 nm) irradiation (Figure 1.3d). This color-switching process could be cycled for 20 times under repeated blue light and red-light illumination. Additionally, green and red colors were obtained by using different redox dyes instead of MB, such as methylene green (MG) and neutral red (NR). The self-doping strategy had the great advantage of synthesizing SnO_{2-x} nanoparticles with a tunable amount of Sn^{2+} dopant to control the number of oxygen vacancies. As expected, SnO_{2-x} nanoparticles with a high amount of Sn^{2+} dopant showed enhanced the photoreduction activity, resulting in the further improvement of color switching speed and cycling properties.[48]

1.3 Mechanochromic nanomaterials

Mechanochromic materials are nanostructures that alter their optical properties in response to mechanical stimuli. The change occurs in their transmission or emission intensity and lifetime (i.e., color), accompanied with excitation by a UV or visible light source. The light interacts with the systems after a molecular or macromolecular-change occurs in response to mechanical stress. At the molecular level, most mechanochromic mechanisms occur through either rearrangement of bonds, disruption of molecular arrangements, or changing in periodically ordered structures.[52]

Various mechanical sensitive molecules are prone to optical changes due to bond breakage or rearrangement. For example, diacetylenes can undertake a cross-linking

reaction based on 1,4-cyclo-addition upon applying mechanical stress, changing the un-crosslinked phase known as the non-fluorescent ‘blue phase’ to a crosslinked phase with fluorescent emission ‘red phase’. Moore et al. have illustrated the breakage of the C-O bond in spiropyran molecules under mechanical pressure. The activation resulted in optical changes from colorless spiropyran to red merocyanine dye. Additionally, various organic and organometallic molecular dyes in the form of liquid crystals or crystalline solids undergo emission color change upon grinding, smearing, or pressing. The mechanical force endows alterations in their intermolecular interactions, including the weak π-π stacking or hydrogen bonding. Dispersion of these dyes within a polymer matrix resulted in forming aggregates that confine a molecular conformation, which breaks upon applying mechanical stress.

Xu et al. synthesized a zinc-complex with tetraphenylethyleneand terpyridine ligands that switch their emission color through grinding or exposure to a pH-sensitive stimulus. Photonic gels, which are photonic crystals constructed by two or more ordered arrays of soft materials, are another class of mechanochromic molecules comprising different dielectric constants, mechanical moduli, or layer thicknesses. Deformation in the soft layer substantially arises with mechanical force, changing the layer spacing that consequently modulates the reflected color (based on optical pathlengths changing). The most common type is based on a one-dimensional photonic gel, by altering layers of two different soft polymers with different dielectric properties. For example, photonic gels of alpha-olefin block interpolymers are constructed through tuning the transparency of multi-layer films and layers’ thickness.[52]

1.3.1 Applications

The potential applications of mechanochromic materials involve biomedicine, electronics, sensors, personal care devices, and coatings fields. Their biological and healthcare applications are vital since stress and strain exerted by the human body can be measured and monitored as personal care devices. Combining the biological reagents with functionalized mechanochromic components in vitro allows measuring the biological systems by transducing the mechanical force into optical readings. For instance, cross-linked polydiacetylene (PDA) lipid, a non-fluorescent material in their self-assembled ribbons and sheets form, can produce fluorescent emission in response to conformational changes (i.e., external mechanical stimulus) in the membranes such as membrane structural disruptions, transmembrane signaling, and enzyme activities.[52]

Mechanochromic materials could also be incorporated with garments to measure pressure exertion from human body motions visually. Bowlin et al. fabricated a shoe base based on PDA-polyurethane composite to detect the distribution of pressure accumulated by the feet. Such flexible composite could also be integrated with tight-fitting clothing such as sportswear and spandex to evaluate muscle and joint movements. Avobenzene and difluoroboron molecules, when coordinated as solid crystalline materials, could be employed in sunscreen formulations as mechanochromic compound. This composite possesses three different crystalline structures (prism, needle, and solid dendritic forms) emitting green, cyan, and blue, respectively. The sunscreen color changes to yellow-orange when smeared on the skin, owing to the destruction of its crystalline structure. The emission color returns to its original color when heated at room temperature.

Additionally, difluoroboron fluorescence molecules are found in biomechanical sensor as a soft surface that sensitively detects 0.1 to 5 kPa pressure. When mechanically active cells and tissues settle on the soft surface, the detection of force by the fluorescent molecules could impart information on the cellular micro-movements using fluorescence microscopy.[52]

Mechanochromic materials could also be used as a safety and packaging indicator for shipments and luxury items. For example, any mechanical deformation that occurs during processing and storing of perishable food products could be monitored by mechanochromic materials incorporated within the packaging's materials. The processing and storage quality could then be assessed by the consumers based on the color-change of the mechanochromic labels. Mechanochromic PDA-polymers based materials were implemented as an impact indicator for the food packaging industry.[52] Another system used for food packaging is based on incorporating nanoparticles within flexible opal films using transverse pressure or extrusion technique. Polyethylacrylate (PEA) was coated on polymethylmethacrylate (PMMA) containing crosslinked polystyrene (PS) to create the structure of a core-shell nanoparticle for the flexible opal films. The longer free paths led to photons scattering in the undoped opal films. Doped opal film generates color appearance because light scatters from the ordered small nanoparticles with short separation distance. The generated color is related to the nanoparticles' size, distribution, and orientation, in addition to the light source. This system can detect volatile gases produced from food during packaging since these gases change the pressure within the films, hence altering the nanoparticles distribution distance. Sagara et al. fabricated

luminescence-active crystals that respond to mechanical forces such as elongation or shearing, which were tested to indicate the quality of items handling and shipment.[53]

1.3.2 Pressure sensors based on responsive plasmonic nanomaterials

1.3.2.1 Mechanism of responsive plasmonic nanomaterials

Localized surface plasmon resonance (LSPR) is a phenomenon that consists of collective oscillation of conduction electrons in nanostructured materials that are excited with electromagnetic filed. The excitation leads to a strong enhancement of the electrical fields surrounding the nanostructures, which augments the extinction at certain resonant wavelength. The proximity of plasmonic nanoparticles initiates “plasmon coupling” due to resonance interactions between the excited plasmons, which results in plasmon hybridization by either shifting or reshaping the plasmonic bands. Noble metals nanostructures possess unique colorimetric functionality owing to their intriguing LSPR properties, which are mainly influenced by their shapes, sizes, compositions, and surrounding environments. Plasmonic colors are generated from the interaction of light resonances corresponding to the discrete energy states for plasmonic nanomaterial. A collective oscillation of free conduction electrons in metals creates the plasmons that generate color resonances.[54–56] Tuning the plasmonic color of inorganic materials can be controlled when the optical properties of the surrounding media are dynamically stimulated. Plasmonic metasurfaces, combined with redox organic electrochromic molecules, show on/off switch when the charge states of the electrochromic organic molecules are changed. These systems demonstrated better refresh rates and optical contrast up to twofold compared to only electrochromic materials.[57,58] The concept is

illustrated in Figure 1.4. Color can be generated by changing the refractive index of the surrounding medium of the nanomaterial to shift the LSPR plasmonic peak. The corresponding color can be tuned based on the LSPR sensitivity:

$$S_n = \frac{\Delta\lambda^*}{\Delta n} = \frac{-2\chi n}{(d\varepsilon_m/d\lambda)_{\lambda^*}}$$

where λ^* is the resonant wavelength, χ is a shape factor of the metal nanoparticle ($\chi = 2$ for spheres), ε_m is the dielectric permittivity of the metal nanoparticle, and n is the refractive index of the medium surrounding the nanoparticle. Ideally, Δn should be large while ensuring $n \sim 1$ to keep the LSPR resonance in the middle of the visible region and allowing $\Delta\lambda^*$ to tune over the whole visible spectrum.[58,59] One rational design of a responsive plasmonic system is to employ organic molecules as a surrounding medium for plasmonic inorganic material. These systems can change their optical properties (Δn) by changing the organic molecules dielectric under external stimuli. For example, inorganic nanomaterials could be integrated with redox organic molecules that can actively change their dielectric constant through an applied electrical field.[41,58–64] Indeed, individual inorganic plasmonic phase-change materials have large (Δn), which made them suitable for the electroactive-plasmonic color-change system. However, they have n larger than 2, so their LSPR resonances are in the near-infrared region (NIR); hence they are not suitable for plasmonic dynamic coloring. As seen in Figure 1.4, the basic design of these electro-responsive plasmonic systems is based on creating a center with metallic nanomaterials covered with a redox organic molecule. The organic molecules could be electrochromes or conductive polymers that perform on/off switching

when their charge state changes. A typical example shown in Figure 1.4 consists of gold nanoparticles coated with polyaniline conductive shell. Once an applied voltage is applied, the oxidation state of PANI will change from $PANI^{+2}$ to $PANI^{0}$ through the oxidation reaction (i.e., coloration), shifting the LSPR peak position of AuNPs, altering the dielectric constant of the gold nanoparticles by changing the refractive index surrounding the AuNPs. The reversible process (i.e., discoloration) is also controlled by applying a reversible voltage causing the $PANI^{0}$ to oxidize into $PANI^{+2}$, hence returning the plasmonic peak of AuNP into its initial state. Through this method, several color dynamics system could be obtained.

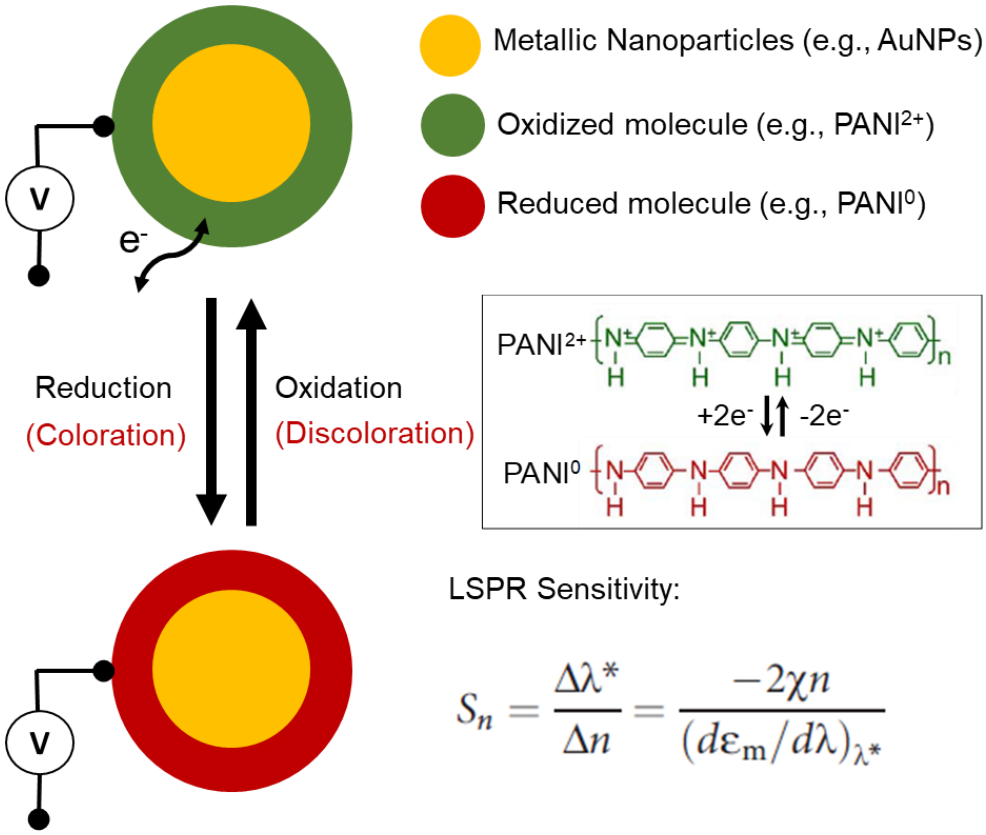

Figure 1.4 Primary strategy of color-switchable responsive-plasmonic nanomaterials. The electro-responsive plasmonic color-switchable hybrid system is used here as an example comprises of Au@PANI core-shell nanostructure. LSPR sensitivity equation is included to demonstrate the correlation between the dielectric constant of the surrounding and the absorption band of the metallic nanoparticle.

1.3.2.2 Applications in pressure sensors

Responsive plasmonic nanomaterials are based on the dynamical change of plasmonic peak and its consequential perceivable color in response to external stimuli such as heat, light, or mechanical stress. Many colorimetric applications have been developed based on that mechanism, including camouflage, anticounterfeiting, encryption, sensing, and others. The main advantages of sensing techniques based on responsive plasmonic nanomaterials are namely: (i) more straightforward fabrication and detection methods; (ii) higher compatibility with various fabrication processes; and (iii) comparable sensitivity with lower cost.[65] Specifically, mechano-responsive plasmonic nanomaterials have extensively investigated recently for their unlimited potentials. In this section, we focus on their synthesis and applications for static and dynamic pressure sensing.

Han et al. have developed a colorimetric pressure sensor using AuNP chain-polymer composite film that can memorize the applied mechanical force. Under mechanical stress, the film deforms and accordingly disassembles the embedded AuNP chains, shifting the plasmonic peak in conjunction with the force strengths. The composites system utilizes the time-dependent viscosity of polymers matrixes in response to mechanical perturbations. Figure 1.5a demonstrates the working mechanism of the system. The composite film is fabricated by homogeneously mixing AuNP chains and a polymer solution. Applying sufficient force for a prolonged period leads to irreversible deformation of the film. The interparticle distance in the AuNP chains widens as the film expands (i.e., deformation), weakening the plasmonic coupling of the particles and

therefore changing the film color. The plasmonic band position can then be correlated to the film expansion extent, producing a proportional colorimetric response.[12]

When polyvinylpyrrolidone (PVP) was used in the composite film, the casted film displayed a deep blue color correlated with an absorption coupling peak at 650 nm of the AuNP chains (Figure 1.5b). Han et al. found that increasing the applied force intensity and duration yielded in increasing the film deformation degrees, which is also proportional to the disassembly extent (i.e., color shift) of the AuNP chains because of the strong adhesion between PVP and AuNP chains in the matrix. Figure 1.5c plots the coupling peak position versus the static pressure applied under different times. A blue shift trend is observed with the increment of the film deformation (i.e., higher pressing times), which is consistent with the working mechanism for the further displacement of AuNPs with more significant film deformations that induce more substantial plasmon band shift.[12]

A colorimetric stress sensor that memorizes applied stress can be fabricated by correlating the pressing pressure at a fixed duration and the observed color-change. This feature is introduced by adding plasticizers to the film composite to extend the pressure response range and sensitivity, hence lowering the film hardness. Short-chains poly(ethylene glycol) (PEG-400) was used as a plasticizer because it reduces the cross-linking degree and improves the viscosity of PVP. As seen in Figure 1.5d, applying different pressures (X 10^4 psi) for a fixed duration (1 min) produced various color-changes in a film doped with 11 wt% PEG-400. The authors argue that this colorimetric stress sensor could be used for car crashes dummies and safety helmets applications.[12]

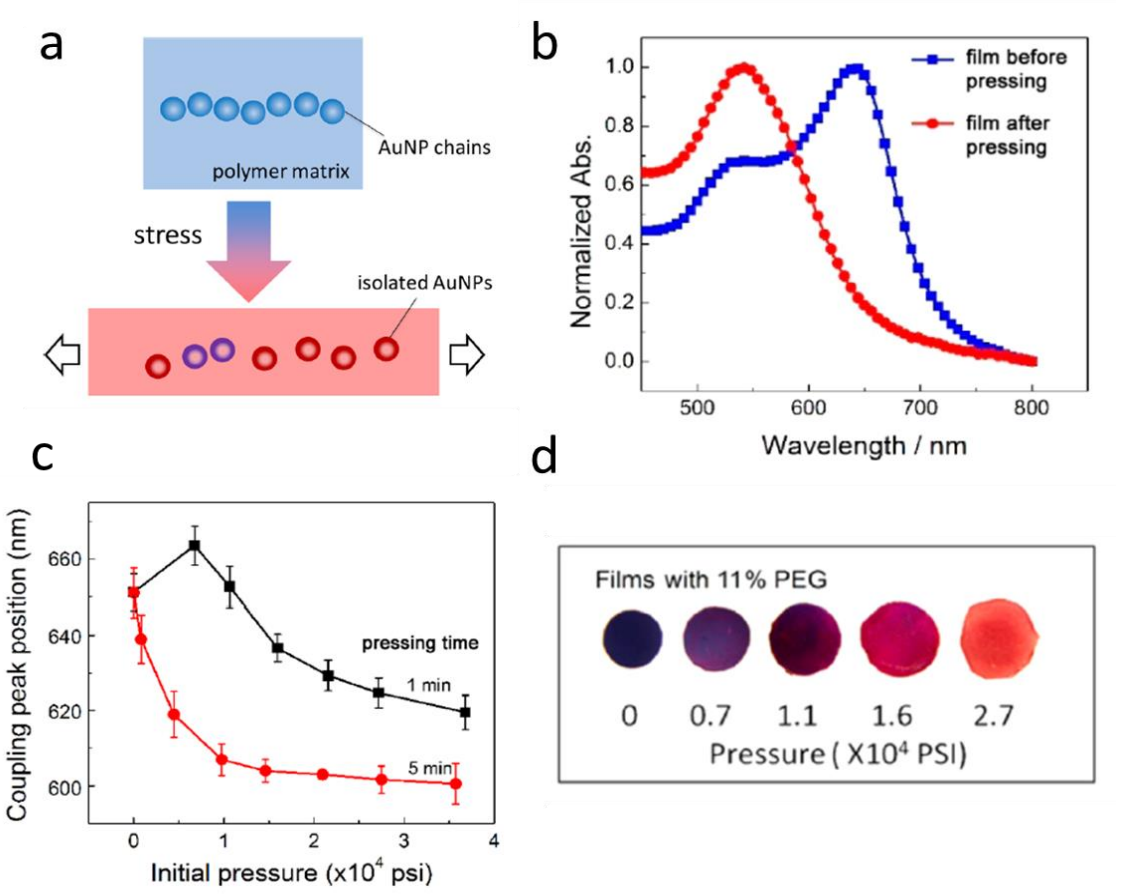

Figure 1.5 (a) Schematic illustration of the mechanism of the colorimetric pressure sensor based on the disassembly of gold nanoparticles. (b) Normalized UV-vis extinction for the AuNP chains before and after pressing. (c) Coupling peak position shift of AuNP chains film under different pressures and pressing times. (d) Images of AuNP chains film doped with 11 wt% PEG after applying different pressures and fixing pressing time (1 min). Adapted with permission from ref. 12.

A similar pressure sensor system was developed by Fu et al. based on noble metal nanorods. Because of their anisotropic shapes, metallic nanorods possess two LSPR modes in their transverse and longitudinal modes, which can be selectively excited by controlling their orientation to incident light. Orienting the nanorods perpendicularly to the incident light excites both modes, producing two LSPR bands in the nanorods extinction spectrum. However, only the transverse mode and its corresponding resonance band are excited and appeared respectively when the nanorods are parallel to the incident angle. Figure 1.6a illustrates the simulated extinction spectra of gold nanorod (AuNR) under different orientations corresponding to the direction of the incident light. The results indicate that the intensity of the AuNR longitudinal mode decreases monotonically when the angles between the AuNR and incident light varies from 90 to 0^{o}.[66]

Fu et al. were able to develop a pressure sensor using the orientational dependence of AuNRs LSPR properties to the ordinary light. Figure 1.6b represents the working mechanism of the proposed sensor. The sensor comprises a composite film based on a polymer matrix embedding highly dispersed AuNRs. The initial orientation of AuNRs will change from random to more ordered states upon applying external pressure to the composite film. The induction pressure causes the polymer to flow perpendicular to the force directions rotating the AuNRs and thus orderly realigning them, which will change the relative intensity of the two LSPR bands of AuNRs correspondingly. Hence, the pressure sensor can be developed by correlating the induced force with the variation of the LSPR properties of the composite film.[66]

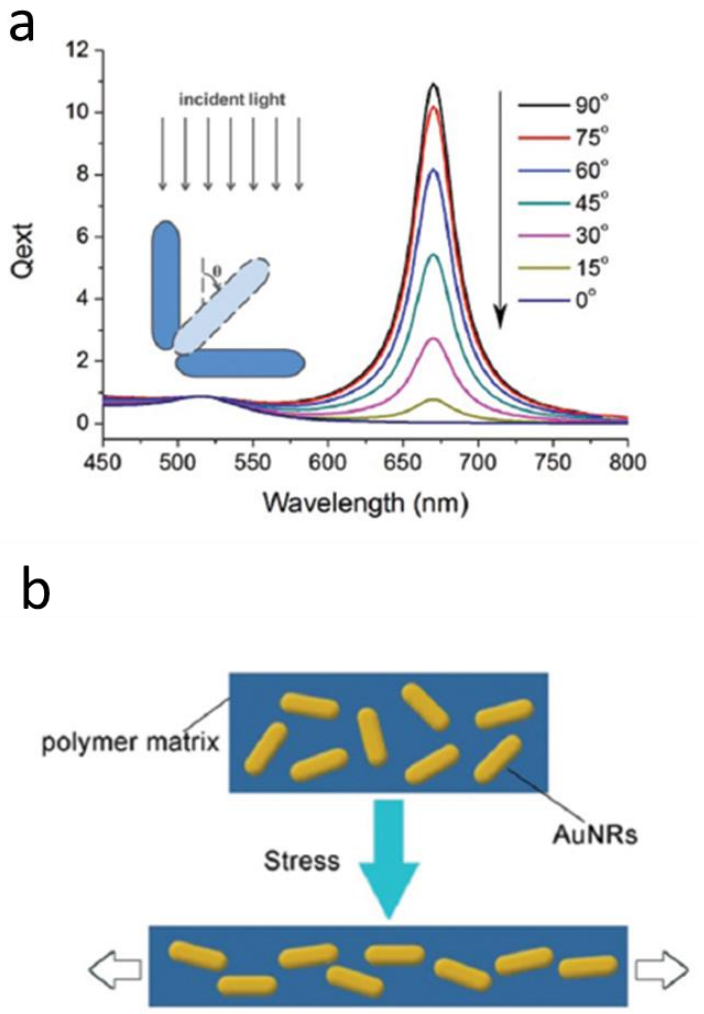

Figure 1.6 (a) Discrete dipole approximation simulations of AuNR extinction spectra in different orientations under unpolarized incident light (cylinder with hemispherical endcaps with L: 24 nm and d:16 nm). (b) Schematic representation of the working mechanism of the pressure responsive composite film based on the directional dependence of AuNRs LSPR. Adapted with permission from ref. 66.

1.4 Magnetic nanoparticles

1.4.1 Physical properties and types

The movements of particles that contain mass and electrical charges (electrons, holes, protons, and positive and negative ions) are responsible for the magnetic properties of materials. Magnetic nanoparticles (MNPs) are particles which have an ordered magnetic structure. MNPs are generally dispersed in a colloidal solution or a medium that resists the particle's movements. Magnetism differs drastically at the nanoscale lengths, presenting a very special type of interaction. In ferromagnetic materials, magnetons are aligned in the same direction by the exchange forces. The domain structure of ferromagnetic materials (also called Weiss domain) relates to its size dependence and magnetic properties. Single domain feature of ferromagnetic materials occurs when their sizes are below a critical value. This critical size is influenced by the strength of crystal anisotropy, exchange forces, surface or domain-wall energy, magnetic saturations, and shape of the particles.[67] The exchange interaction that rises the order of ferromagnetism and its associated energy is expressed as follows:

$$E = -JS_1S_2$$

where J is the exchange integral or the constant between the atomic spins S_1 and S_2. The exchange interaction favors the atomic spins or magnetic moments to be antiparallel or parallel to each other, respectively, depending on the negative or positive sign of J.[68]

Further reduction of the size of single-domain particles below a critical diameter changes them into superparamagnetic ones. Superparamagnetism is governed by thermal

fluctuations effects, that are when strong enough, spontaneously demagnetize the saturated particles assembly.[67]

Ferromagnetic, paramagnetic, antiferromagnetic, and ferrimagnetic particles are composed of materials that contain unpaired electrons in their atomic shells, usually in the 3*d* and 4*f* orbitals. Paramagnetic particles have atomic magnetic moments with no long-range order with small positive magnetic susceptibility (e.g., pyrite). Materials with aligned atomic magnetic moments of equal magnitude and direct coupling interactions between the moments are ferromagnet (e.g., Fe, Ni, and Co). Antiferromagnetism observes in materials with atomic magnetic moments of equal magnitude that are arranged in an antiparallel structure (e.g., troilite FeS). Lastly, ferrimagnetic materials have atoms or ions that induce ordered in a nonparallel arrangement in a zero applied field below a specific characteristic temperature (Néel temperature) such as Fe_3O_4 and Fe_3S_4.[67]

Fe and Fe oxides with uniform compositions are the most common types of MNPs. However, ferrites materials consist of Zn, Co, Ni, and rare earth metals are also MNPs that commonly used for biomedical applications. Pure metal particles such as pure Fe and FeCo alloy particles possess large magnetization. In contrast, rare earth metals alloys such as Nd-Fe-B and Sm-Co are usually permanent magnets.

1.4.2 Applications

MNPs have various potential applications in biomedical, industrial, energy, and environmental fields. For example, hematite and magnetite have been used as catalysts for NH_3 production, desulfurization of natural gas, high-temperature water-gas shift

reaction, dehydrogenation of ethylbenzene to styrene, oxidation of alcohols, and large-scale production of butadiene. However, MNPs are extensively used in catalysis applications to recover the catalyst in heterogeneous reactions, which are more efficient than using cross-flow filtration or centrifugation. Magnetic separation of catalysts is favorable than all established methods, especially for sub-micrometer size catalysts. The separation ease of magnetic catalysts in a quasi-homogeneous system allows for the advantageous recycling of expensive catalysts or ligands. Such systems include using MNP-supported catalyst in enzymatic reaction for carboxylate resolution, ester hydrolysis, and Knoevenagel reactions.[67]

MNPs have also shown great potentials for *in vitro* and *in vivo* biomedical applications. In vitro applications include diagnostic separation, selections, and magnetorelaxometry, while in vivo include therapeutic (e.g., drug delivery) and diagnostic applications (nuclear magnetic resonance (NMR) imaging). Specifically, dragging MNPs with a magnetic field into the targeted area allows the delivery of medication or drug to be released locally. Delivering the drugs to the specific sites could eliminate unwanted side effects and reduce the required dosages. The same approach could be used in NMR imaging for clinical diagnosis. The administrated drugs could be delivered to the specific area to enhance the NMR image contrast between normal and diseased tissues, or indicate the functionality of organs or blood flow.[67,69]

Particles with magnetic vortex features are assumed to be beneficial for information storage technologies and spintronic oscillators. They are fabricated and patterned into the proper shapes by thin-film fabrication methods and lithography,

respectively. Permalloy ($Ni_{80}Fe_{20}$) vortex disks can be modified to bind to cancer cells, which then employed to destruct these cells by magneto-mechanical actuation, namely by producing a torque by a low-amplitude (10mT) and low-frequency (around 10Hz) alternating magnetic field, initiating cancer membrane apoptosis process (programmed cell death). Compared to magnetic hyperthermia, apoptosis treatment eliminates damaging the associated healthy tissues with the targeted cells. It avoids inflammatory side effects and the aggregation of particles inside the blood vessels owing to the lack of disks' remanence in the vortex state.[68]

Additionally, MNPs possess great potentials in the remediation of contaminants in groundwater, soil, and air, by magnetically removing organic or inorganic pollutants. Dyes removal for water purification could be employed by synthesizing magnetic dye-adsorbent for industrial sectors that produce wastewater streams with dyes contamination such as the textile, tanneries, and paint industries. MNPs also show high capacity and performance for the removal of metal ions in wastewater. The key advantages of magnetic separation of contaminants are their low cost and continuous and contaminant-specific separation operation.[68,69]

1.4.3 Chemical synthesis and functionalization

Chemical synthesis of MNPs provides the ability to control the composition, shape, morphology, crystallinity, size, colloidal stability, and magnetic properties of the particles by modulating the reaction reagents, time, stabilizing ligands, pH and temperature.[68] Figure 1.7 presents the general workflow design of MNPs. For example, iron oxide magnetic nanoparticles can be synthesized by various synthetic approaches,

including co-precipitation, micelle formation, hydrothermal, polyol, thermal decomposition, and laser pyrolysis methods.[69]

Iron oxide nanoparticles have been widely synthesized through the solution precipitation method by adding a precipitation agent into an aqueous solution of metal precursor to generate an insoluble solid product. This method is capable of producing MNPs with high yields and uniformity. Additionally, it is simple and cost-effective, while only self-nucleation must be avoided during the growth step to produce monodisperse MNPs. However, co-precipitation methods consider more effective in synthesizing MNPs (especially iron oxide NPs) by adding a base under anaerobic condition at ambient or high temperatures to aqueous Fe(II) and/or Fe(III) solutions. Unlike the acidic environment of the precipitation method, nanoscale magnetite doesn't decompose into maghemite when dissolving in basic medium, preventing the quick oxidation of magnetite to maghemite. The co-precipitation approach also ensures the high reproduction quality of MNPs, as long the synthetic conditions are maintained. There are several factors such as temperature and pH of the reaction, type of iron salts, volume and ionic strength of the solution, and Fe(II):Fe(III) ratio that significantly influence the shape, size, and composition of MNPs during their co-precipitation synthesis.[69]

Thermal decomposition of organometallic precursors in organic solvents and in the presence of capping ligands produces colloidal MNPs. However, they are usually associated with safety concerns, including high temperatures and pressure during the synthesis, and the presence of toxic organic liquids and vapors. Annealing temperature governs the size distribution, structural shapes, and the magnetic properties of MNPs.

Monodispersed iron oxide magnetic nanoparticles (6-20 nm) were synthesized by the thermal decomposition of $Fe(CO)_5$ in the presence of surfactants as capping ligands. Thermal decomposition of precursors containing zero-valent metal like $Fe(CO)_5$ forms metallic nanoparticles followed by an oxidation reaction to produce monodisperse magnetic nanoparticles.[69]

The hydrothermal or solvothermal route is commonly used to synthesize MNPs in high yield. High temperatures in the range of 125 to 250ºC and high pressures ranging from 0.3 to 4 MPa are usually required for the hydrothermal synthesis. For example, iron oxide nanoparticles with 40 nm size and saturation magnetization of 85.8 emu. g^{-1} were hydrothermally synthesized at 140 ºC degree, significantly lower than bulk iron oxide materials. In hydrothermal methods, generally, the precursors' concentration and, more importantly, the reaction kinetics govern the average size distribution of the produced particles.[69]

Polyol synthesis is another method that uses a liquid-phase approach to synthesize iron oxide nanoparticles in the presence of polyol molecules under high temperatures. Polyol molecules such as ethylene glycol, diethylene glycol, triethylene glycol, and tetraethylene glycol are usually used during the synthesis. Polyols are excellent in controlling the particle size, distribution, and dispersity because they can instantaneously coordinate with the nuclei during the particle's formation. Highly crystalline oxide nanoparticles can also be synthesized using the polyol method, which rules-out post-sintering treatment of the particles. Adjusting the reaction temperature during the polyol

synthesis of metal oxides can produce elemental metals particles by restricting the reduction nature of the polyols.[69]

MNPs are often functionalized through surface coating by either magnetic or nonmagnetic materials. This functionalization is intended to (i) enhance the chemical and colloidal stability of MNPs; (ii) introduce another layer for further functionalization; (iii) change the magnetic properties of the particles; and (iv) prevent MNPs from aggregation, oxidation, corrosion, and toxicity. Commonly used materials for MNPs surface coating include silica (SiO_2), Au, organic stabilizers (e.g., oleic acid, stearic acid, etc.), and polymer stabilizers (e.g., polyethylene glycol, and polyvinyl pyrrolidone (PVP)). Organic ligands are often coated on MNPs during their chemical synthesis by chemical or physical attachment. However, they are not compatible with highly reactive MNPs (e.g., Fe MNPs), and they usually degrade at high temperatures. On the other hand, inorganic materials such as carbon and SiO_2 provide better stability and compatibility as coating layers than organic or polymeric coatings.[68]

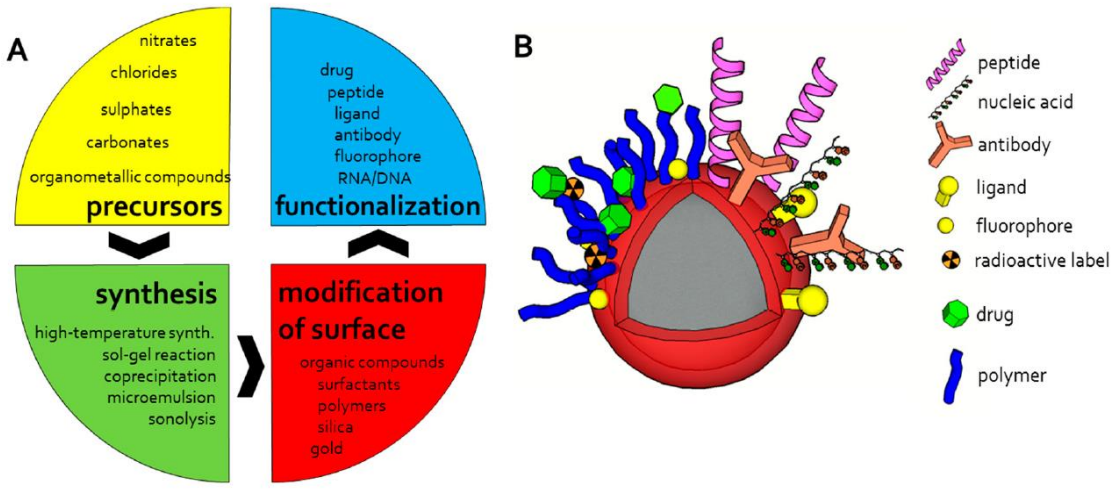

Figure 1.7 (a) Scheme flow of magnetic particle design. (b) possible modifications and functionalization of magnetic particles. Adapted with permission from ref. 70.

1.4.4 Magnetizing nanostructured materials

The ability to introduce magnetic properties into nonmagnetic particles can provide new functionalities to nanomaterials. There are currently two routes for incorporating magnetic properties into nanostructured materials: (i) coating the functional nonmagnetic materials or molecules into a magnetic core; and (ii) attachment of magnetic particles into the nonmagnetic structures. These two methods are represented in Figure 1.8. In the first route, the targeted materials, including a metallic, metal oxide, polymeric, and dendrimeric shells, can be coated on magnetic core particles such as Co, Ni, Mn, Fe, and their alloys and oxides. The coating procedure is well developed following wet chemistry or physical, synthetic methods. In order to perform the coating of nonmagnetic materials on magnetic cores, there should be a strong affinity between the two structures, which could be achieved either by performing surface modification of the magnetic cores or adding a transitional layer that binds both surfaces. The synthesis of the magnetic particles also follows the same synthetic methods, as described in the previous section. This coating route is represented in Figure 1.8a. Additionally, the surface attachment of magnetic nanostructures into nonmagnetic materials generally follows surface modification of magnetic particles or the nonmagnetic materials.[68–70]

Goebl et al. have developed a magnetically tunable colloidal micromirror based on the attachment of small magnetic iron oxide nanoparticles into nonmagnetic Au microplates. Superparamagnetic maghemite nanocrystals were synthesized first using a high-temperature oil-phase reaction. The surface of the particles was treated using tetramethylammonium hydroxide (TMAH) to obtain water solubility of the particles.

Then, the magnetic particles were coated with a thin layer of SiO_2 via a modified Stöber process followed by its functionalization with amine groups (APTES). The amine-functionalized superparamagnetic nanoparticles were attached to the surface of the microplate through the strong affinity between the amine groups and the Au surface. This attachment procedure is schematically summarized in Figure 1.8b. The reflective system exhibits a strong response and alignment with the direction of the applied magnetic field. The transmittance and reflectance of the system can vary by a factor of 2 and 6, respectively, through varying the magnetic field angles. This responsive system is believed to work as an optically-responsive micromirror.[71]

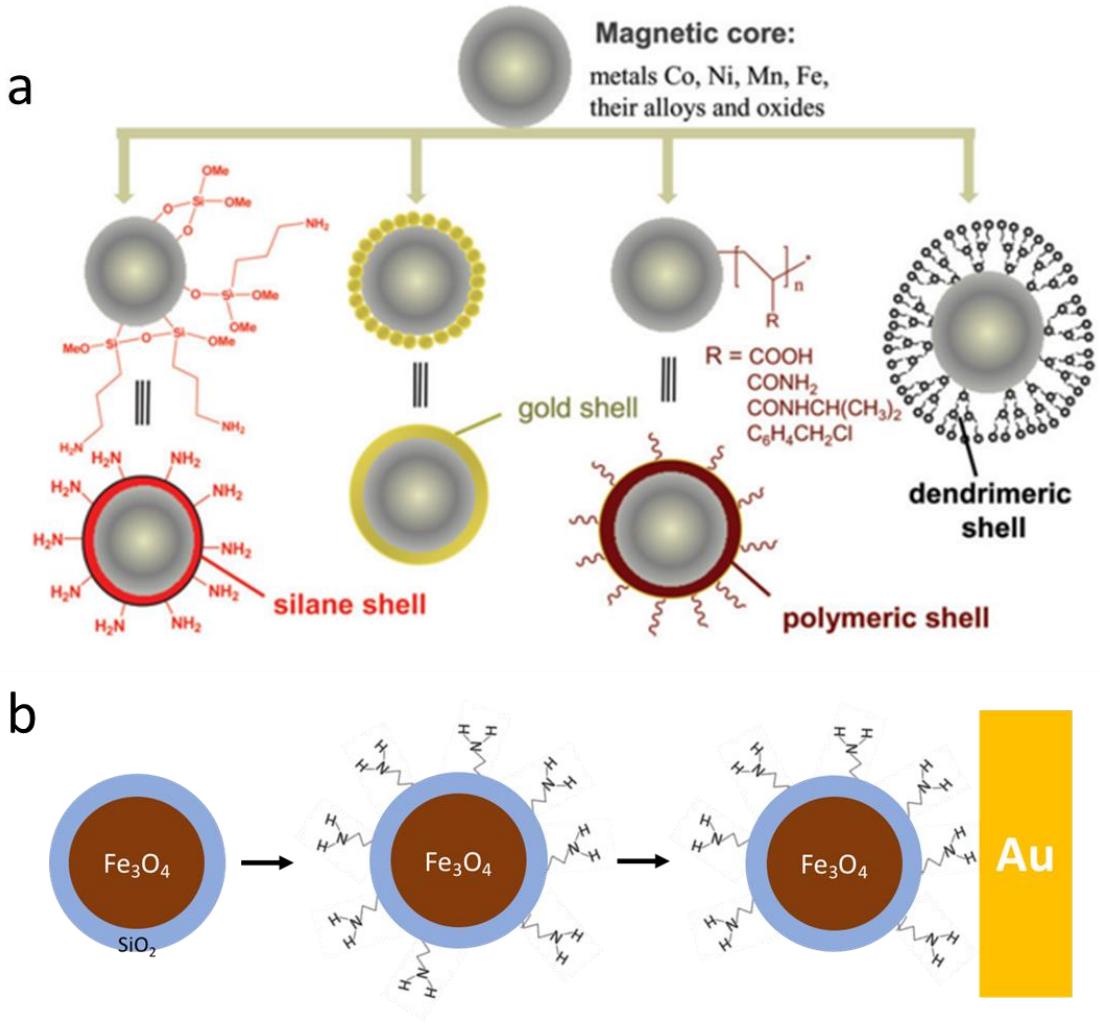

Figure 1.8 (a) Schematic approach for magnetizing nonmagnetic materials by coating nonmagnetic materials shells on magnetic cores. (b) The second approach of magnetizing materials by attaching magnetic particles into their surface. Adapted with permission from ref. 69.

1.5 Scope of the dissertation

This dissertation summarizes different strategies of engineering responsive-properties in nanostructured materials. The dissertation focuses on three types of responsive nanomaterials: optically, mechanically, and magnetically-responsive. Each type is presented in a different chapter, titled: (i) photocatalytic black-coloring of N-TiO_2 for reversible light-printing; (ii) colorimetric stress sensor based on nanoparticles deformation; and (iii) anchoring magnetic iron oxide through molybdenum sulfide transitional layer: a universal magnetizing method.

Chapter 2 introduces a new photoreversible color-switching system based on nitrogen-doped TiO_2 nanocrystals. The synthetic method involves the structural engineering of TiO_2 through nitrogen doping in a high-temperature hydrolysis reaction and bounding organic glycols molecules onto the titania surfaces to act as SEDs. The photocatalytic system showed excellent response to light-irradiation producing an apparent black color under light irradiation, corresponding to the surface self-reduction of Ti(IV) to Ti(III). The new system was implemented as a rewritable paper platform showing a reversible color-switching that could retain writing for hours without the need for any redox dyes or polymeric molecules. It also allowed freehand writing using a visible-light laser pen or printing with a photomask due to its rapid-response and strong absorption features. The overall mechanism, performance, and the physical and chemical properties of the nanocrystals are discussed in this chapter.

Chapter 3 discusses the fabrications of colorimetric pressure sensor based on the deformation of Au@Ag@void@TiO_2 nanostructured materials. This chapter starts by

introducing the concept of LSPR peak shift by changing the environment surrounding the nanostructured plasmonic materials. The design and proposed method are outlined with the focus on using the yolk-shell nanostructure for the proposed mechanism. The colorimetric mechanism consists of changing the plasmonic absorption of Au@Ag@void@TiO_2 by changing the surrounding environment of Au@Ag nanostructure from air to TiO_2 after deforming the outer particle shell. The prospects of choosing Au@Ag@void@TiO_2 nanostructures are investigated through experimental and simulated measurements. The development of a confined-seeded growth of Ag, the overall performance of different thickness sizes of Ag and TiO_2 shells, the fabrication process of the pressure sensor, and the utilization of the material as an impact and dynamic force sensors are discussed in this chapter.

Chapter 4 presents a new method of attaching iron oxide magnetic nanoparticles onto nonmagnetic nanomaterials by using molybdenum sulfide as a transitional layer. The primary motivation of this work is to create a universal, rapid, simple, cost-effective, and robust method for magnetizing nanostructured materials. Firstly, the binding between molybdenum sulfide and iron oxide is investigated using XPS, EXAFS, Raman, and FTIR measurements. Secondly, a universal colloidal coating method of molybdenum sulfide on SiO_2 is developed. The controllability parameters, mechanism, and characterization of the colloidal coating of SiO_2@a-MoS_x are investigated and discussed in this chapter. Additionally, the attachments of various iron oxide materials onto SiO_2@a-MoS_x nanostructures are demonstrated. A magnetically-tunable micromirror

system is fabricated using a-MoS_x/Fe_3O_4 magnetizing method to illustrate the practicality and usefulness of the universal magnetizing strategy.

Chapter 5 presents the outlook and future directions of the work presented in this dissertation.

1.6 References

[1] F. Davis, F. M. Shimizu, Z. Altintas, *Biosens. Nanotechnol.* **2018**, 219–276.

[2] M. Yoshida, J. Lahann, *ACS Nano* **2008**, *2*, 1101–1107.

[3] U. Jeong, Y. Yin, *Adv. Funct. Mater.* **2020**, *30*, 1907059.

[4] P. Bonhôte, E. Gogniat, F. Campus, L. Walder, M. Grätzel, *Displays* **1999**, *20*, 137–144.

[5] M. Grätzel, *Nature* **2001**, *409*, 575–576.

[6] Y. Wang, E. L. Runnerstrom, D. J. Milliron, *Annu. Rev. Chem. Biomol. Eng.* **2016**, *7*, 283–304.

[7] B. O'Regan, M. Grätzel, *Nature* **1991**, *353*, 737–740.

[8] J.-J. Wu, M.-D. Hsieh, W.-P. Liao, W.-T. Wu, J.-S. Chen, *ACS Nano* **2009**, *3*, 2297–2303.

[9] C. Weder, *J. Mater. Chem.* **2011**, *21*, 8235–8236.

[10] J. Wang, J. A. Kaplan, Y. L. Colson, M. W. Grinstaff, *Adv. Drug Deliv. Rev.* **2017**, *108*, 68–82.

[11] Y. Zhang, S. Sinha-Ray, A. L. Yarin, *J. Mater. Chem.* **2011**, *21*, 8269–8281.

[12] X. Han, Y. Liu, Y. Yin, *Nano Lett.* **2014**, *14*, 2466–2470.

[13] Z. Li, F. Yang, Y. Yin, *Adv. Funct. Mater.* **2020**, *30*, 1903467.

[14] M. Grzelczak, L. M. Liz-Marzán, R. Klajn, *Chem. Soc. Rev.* **2019**, *48*, 1342–1361.

[15] Z. Li, Y. Yin, *Adv. Mater.* **2019**, *31*, 1807061.

[16] R. J. Mortimer, *Chem. Soc. Rev.* **1997**, *26*, 147–156.

[17] P. Bamfield, *Chromic Phenomena*, The Royal Society Of Chemistry, **2010**.

[18] V. K. Thakur, G. Ding, J. Ma, P. S. Lee, X. Lu, *Adv. Mater.* **2012**, *24*, 4071–4096.

[19] J. M. Wang, X. W. Sun, Z. Jiao, *Mater.* **2010**, *3*, DOI 10.3390/ma3125029.

[20] D. Cummins, G. Boschloo, M. Ryan, D. Corr, S. N. Rao, D. Fitzmaurice, *J. Phys. Chem. B* **2000**, *104*, 11449–11459.

[21] H. K. Jheong, Y. J. Kim, J. H. Pan, T.-Y. Won, W. I. Lee, *J. Electroceramics* **2006**, *17*, 929–932.

[22] S.-K. Lee, A. Mills, A. Lepre, *Chem. Commun.* **2004**, 1912–1913.

[23] W. Weng, T. Higuchi, M. Suzuki, T. Fukuoka, T. Shimomura, M. Ono, L. Radhakrishnan, H. Wang, N. Suzuki, H. Oveisi, et al., *Angew. Chemie Int. Ed.* **2010**, *49*, 3956–3959.

[24] P. Zhang, F. Zhu, F. Wang, J. Wang, R. Dong, X. Zhuang, O. G. Schmidt, X. Feng, *Adv. Mater.* **2017**, *29*, 1604491.

[25] W. Wang, N. Xie, L. He, Y. Yin, *Nat. Commun.* **2014**, *5*, 5459.

[26] W. Wang, Y. Ye, J. Feng, M. Chi, J. Guo, Y. Yin, *Angew. Chemie Int. Ed.* **2015**, *54*, 1321–1326.

[27] D. K. Macharia, S. Ahmed, B. Zhu, Z. Liu, Z. Wang, J. I. Mwasiagi, Z. Chen, M. Zhu, *ACS Appl. Mater. Interfaces* **2019**, *11*, 13370–13379.

[28] G. Cai, P. Darmawan, X. Cheng, P. S. Lee, *Adv. Energy Mater.* **2017**, *7*, 1602598.

[29] A. Mills, J. Wang, S.-K. Lee, M. Simonsen, *Chem. Commun.* **2005**, 2721–2723.

[30] A. Mills, K. Lawrie, J. Bardin, A. Apedaile, G. A. Skinner, C. O'Rourke, *Analyst* **2012**, *137*, 106–112.

[31] Y. Rong, S. Kim, F. Su, D. Myers, M. Taya, *Electrochim. Acta* **2011**, *56*, 6230–6236.

[32] R. Cinnsealach, G. Boschloo, S. Nagaraja Rao, D. Fitzmaurice, *Sol. Energy Mater. Sol. Cells* **1999**, *57*, 107–125.

[33] L. Striepe, T. Baumgartner, *Chem. – A Eur. J.* **2017**, *23*, 16924–16940.

[34] P. Camurlu, *RSC Adv.* **2014**, *4*, 55832–55845.

[35] A. L.-S. Eh, A. W. M. Tan, X. Cheng, S. Magdassi, P. S. Lee, *Energy Technol.* **2018**, *6*, 33–45.

[36] X. Li, K. Perera, J. He, A. Gumyusenge, J. Mei, *J. Mater. Chem. C* **2019**, *7*, 12761–12789.

[37] L. Shao, X. Zhuo, J. Wang, *Adv. Mater.* **2018**, *30*, 1704338.

[38] J.-H. Ryu, J.-H. Lee, S.-J. Han, K.-D. Suh, *Macromol. Rapid Commun.* **2006**, *27*, 1156–1161.

[39] W. Wang, M. Ye, L. He, Y. Yin, *Nano Lett.* **2014**, *14*, 1681–1686.

[40] D. Han, B. Jiang, J. Feng, Y. Yin, W. Wang, *Angew. Chemie Int. Ed.* **2017**, *56*, 7792–7796.

[41] N. Jiang, L. Shao, J. Wang, *Adv. Mater.* **2014**, *26*, 3282–3289.

[42] W. Lu, N. Jiang, J. Wang, *Adv. Mater.* **2017**, *29*, 1604862.

[43] X. W. Sun, J. X. Wang, *Nano Lett.* **2008**, *8*, 1884–1889.

[44] A. Mills, N. Wells, *Chem. Soc. Rev.* **2015**, *44*, 2849–2864.

[45] Y. Pellegrin, F. Odobel, *Comptes Rendus Chim.* **2017**, *20*, 283–295.

[46] W. Wang, M. Ye, L. He, Y. Yin, *Nano Lett.* **2014**, *14*, 1681–1686.

[47] J. Feng, F. Yang, Y. Ye, W. Wang, X. Yao, Q. Fan, L. Liu, R. M. Aleisa, J. Guo, Y. Yin, *Nanoscale* **2019**, *11*, 19512–19519.

[48] D. Han, B. Jiang, J. Feng, Y. Yin, W. Wang, *Angew. Chemie - Int. Ed.* **2017**, *56*, 7792–7796.

[49] X. Yu, B. Kim, Y. K. Kim, *ACS Catal.* **2013**, *3*, 2479–2486.

[50] W. Wang, N. Xie, L. He, Y. Yin, *Nat. Commun.* **2014**, *5*, 1–7.

[51] W. Wang, Y. Ye, J. Feng, M. Chi, J. Guo, Y. Yin, *Angew. Chemie - Int. Ed.* **2015**, *54*, 1321–1326.

[52] Y. Jiang, *Mater. Sci. Eng. C* **2014**, *45*, 682–689.

[53] K. Sadeghi, J.-Y. Yoon, J. Seo, *Polym. Rev.* **2019**, 1–51.

[54] A. Kristensen, J. K. W. Yang, S. I. Bozhevolnyi, S. Link, P. Nordlander, N. J. Halas, N. A. Mortensen, *Nat. Rev. Mater.* **2016**, *2*, 16088.

[55] M. Song, D. Wang, S. Peana, S. Choudhury, P. Nyga, Z. A. Kudyshev, H. Yu, A. Boltasseva, V. M. Shalaev, A. V Kildishev, *Appl. Phys. Rev.* **2019**, *6*, 41308.

[56] T. Lee, J. Jang, H. Jeong, J. Rho, *Nano Converg.* **2018**, *5*, 1.

[57] T. Xu, E. C. Walter, A. Agrawal, C. Bohn, J. Velmurugan, W. Zhu, H. J. Lezec, A. A. Talin, *Nat. Commun.* **2016**, *7*, 10479.

[58] J. Peng, H.-H. Jeong, Q. Lin, S. Cormier, H.-L. Liang, M. F. L. De Volder, S. Vignolini, J. J. Baumberg, *Sci. Adv.* **2019**, *5*, eaaw2205.

[59] M. M. Miller, A. A. Lazarides, *J. Phys. Chem. B* **2005**, *109*, 21556–21565.

[60] K. Xiong, G. Emilsson, A. Maziz, X. Yang, L. Shao, E. W. H. Jager, A. B. Dahlin, *Adv. Mater.* **2016**, *28*, 9956–9960.

[61] T. A. F. König, P. A. Ledin, J. Kerszulis, M. A. Mahmoud, M. A. El-Sayed, J. R. Reynolds, V. V Tsukruk, *ACS Nano* **2014**, *8*, 6182–6192.

[62] A. Baba, K. Tada, R. Janmanee, S. Sriwichai, K. Shinbo, K. Kato, F. Kaneko, S. Phanichphant, *Adv. Funct. Mater.* **2012**, *22*, 4383–4388.

[63] Z. Zhou, Y. Yu, N. Sun, H. Möhwald, P. Gu, L. Wang, W. Zhang, T. A. F. König, A. Fery, G. Zhang, *ACS Appl. Mater. Interfaces* **2017**, *9*, 35244–35252.

[64] J.-W. Jeon, J. Zhou, J. A. Geldmeier, J. F. Ponder, M. A. Mahmoud, M. El-Sayed, J. R. Reynolds, V. V Tsukruk, *Chem. Mater.* **2016**, *28*, 7551–7563.

[65] Z. Li, W. Wang, Y. Yin, *Trends Chem.* **2020**, DOI https://doi.org/10.1016/j.trechm.2020.03.008.

[66] L. Fu, Y. Liu, W. Wang, M. Wang, Y. Bai, E. L. Chronister, L. Zhen, Y. Yin, *Nanoscale* **2015**, *7*, 14483–14488.

[67] A. Akbarzadeh, M. Samiei, S. Davaran, *Nanoscale Res. Lett.* **2012**, *7*, 144.

[68] J. Alonso, J. M. Barandiarán, L. Fernández Barquín, A. García-Arribas, in *Micro Nano Technol.* (Eds.: A.A. El-Gendy, J.M. Barandiarán, R.L.B.T.-M.N.M.

Hadimani), Elsevier, **2018**, pp. 1–40.

[69] S. Gul, S. B. Khan, I. U. Rehman, M. A. Khan, M. I. Khan, *Front. Mater.* **2019**, *6*, 179.

[70] J. Kudr, Y. Haddad, L. Richtera, Z. Heger, M. Cernak, V. Adam, O. Zitka, *Nanomater. (Basel, Switzerland)* **2017**, *7*, 243.

[71] J. Goebl, Y. Liu, S. Wong, S. Zorba, Y. Yin, *Nanoscale Horizons* **2016**, *1*, 64–68.

Chapter 2. Photocatalytic Black-Coloring of N-TiO_2 for Reversible Light-Printing

2.1 Introduction

Consumption of papers has been linked to numerous environmental issues such as deforestation, production of hazardous waste, climate change, global warming, and high consumption of water.[1,2] "Rewritable paper", based on stimuli-responsive materials, has been proposed recently as an effective alternative that can undergo writing and erasing multiple times.[3] External stimulants such as light, pH, heat, mechanical force, and chemical reaction have been utilized to create color-switching processes in a fast and cyclable manner.[4–9] For instance, hydrochromic rewritable paper has been developed by Sheng et al. employing oxazolidine-based chromic dyes which exhibit color-switching abilities upon reacting with water.[10] Another rewritable system based on terpyridine ligand and metal salt solutions interactions has produced various colored pictures that could be erased by eliminating the interactions using tetrabutylammonium fluoride solution.[11] In our group, we have demonstrated several photoreversible color-switching systems based on photocatalytic TiO_2 nanocrystals that induce a reversible-redox reaction of colored dyes.[9,12] Through doping and surface engineering of the photoactive nanoparticles, we were able to introduce more robust rewritable systems with better cyclability and coloring duration.[13–15]

Although successful prototypes of rewritable papers were achieved, significant challenges associated with the technology still remain, namely: (i) developing a non-toxic, cheap, and abundant chromic material (i.e., eliminating the use of scarce metals doping, organic dyes, inorganic moieties, and conjugated polymers) that can perform

writing and erasing in a fast and precise manner; (ii) generating a coating method of the material that could be applied to various substrates, including glass, plastic, paper, and cardboard; (iii) utilizing a readily-available and controllable stimulant for writing and erasing that do not require tedious operating procedure and high cost, and do not present any harm to the people or the environment; (iv) maintaining high stability of the material over repeated cycles without losing functionality to external fluctuations such as heat, humidity, and air; and (v) having costly-effective large scale fabrication and coating methods.[3]

Previous studies have shown that pure TiO_2 can change color from white to black/dark blue after being irradiated with UV-light in the absence of oxygen, caused by the reduction of Ti(IV) to Ti(III) species by photo-excited electrons.[16–20] This property, if appropriately utilized, can make an ideal color switching system based on TiO_2, which is safe, earth-abundant, and widely used as a pigment, sunscreen, and food coloring. However, the black/dark blue color was found to be extremely unstable, disappearing within several seconds once the material exposes to air due to the autoxidation of Ti(III) to Ti(IV).[16–18,21–25] Furthermore, a high-energy light source (e.g., 500 W Xenon lamp) has to be used to irradiate the typical TiO_2 for several hours in order to reach a visible color change.[26]

In this work, we take on the above challenges and propose a new photoreversible color-switching system based on surface-functionalized N-doped TiO_2 nanocrystals. Driven by the surface self-reduction of Ti(IV) to Ti(III) by the light-excited electrons, these nanocrystals can change color from white to black rapidly (within seconds) in

response to a considerably low-power UV irradiation (3 W). In contrast, the black color can remain stable over hours in the air. In our design, nitrogen doping promotes the fast coloration response of the material. The presence of chemically- and physically-adsorbed glycol molecules on the titania surface also accelerates the coloration response by scavenging electron holes during light excitation and prolong the black color period to several hours by stabilizing the reduced Ti species. This new photoreversible color-switching TiO_2 nanocrystals can be deposited on various substrates to produce a rewritable paper to which high-resolution pictures and writings can be printed using a UV light and erased by heating at 50 ^oC under ambient conditions. The as-made rewritable paper possesses many advantages over previous color-switching systems owing to its rapid response, simplicity, and low cost in the synthesis and processing, low toxicity, and excellent stability and reversibility for consecutive writing and erasing steps exceeding 30 times. Beyond rewritable paper applications, we believe this new reversible color-switching performance of TiO_2 will help in developing more practical applications such as oxygen indicators, food labeling, data storage, and smart windows.

2.2 Materials and methods

2.2.1 Materials

Titanium (IV) chloride ($TiCl_4$), copper (II) chloride ($CuCl_2$), barium chloride ($BaCl_2$), diethylene glycol (DEG), tetraethyl ethylene glycol (EG), hydroxypropyl cellulose (HPC, Mw ~80,000), acetone, ethanol, and methylene blue (MB) were purchased from Sigma-Aldrich. Urea was purchased from Fisher Chemical. All chemicals were analytical grade and used as received without further purification.

Solutions were prepared with water (18.2 MΩ/cm) produced from Milli-Q system (Millipore).

2.2.2 Synthesis of TiO_2 nanocrystals

0.2 ml $TiCl_4$ was injected by a syringe into 20 ml DEG in a three-neck round-bottom flask. The mixture was then heated at 220 ^oC for 3 hours under reflux in the air (no flow of water). The reaction flask was exposed to the air during the first 2 hours of the synthesis, but it was capped in the last hour. The mixture was left to cool at room temperature. Finally, the product was collected through centrifuging (8000 rpm, 5 min), washed two times with acetone, and re-dispersed in water.

2.2.3 Synthesis of N-doped TiO_2 nanocrystals

0.05 g urea was added to 20 ml DEG in a three-neck round-bottom flask and stirred vigorously at 50 ^oC for 15 min until urea is completely dissolved. Then, 0.2 ml $TiCl_4$ was added, and the mixture was heated at 220 ^oC for 3 h under air refluxing. A brown/black solution was seen at the end of the reaction. The mixture was left to cool at room temperature. The product was collected through centrifuging (8000 rpm, 5 min), washed two times with acetone, and re-dispersed in 5 ml water.

2.2.4 Synthesis of Cu-TiO_2 nanocrystals

$CuCl_2$ (0.4 mmol) was dissolved in 20 mL DEG in a three-neck round-bottom flask under vigorous stirring. Then, 0.2 ml $TiCl_4$ was injected, and the mixture was heated at 220 ^oC for 3 h under air refluxing. The mixture was left to cool at room temperature. The product was collected through centrifuging (8000 rpm, 5 min), washed two times with acetone and ethanol, and then redispersed in water.

2.2.5 Synthesis of Ba-TiO_2 nanocrystals

$BaCl_2$ (2 mmol) was dissolved in 20 mL DEG in a three-neck round-bottom flask under vigorous stirring. Then, 0.2 ml $TiCl_4$ was injected, and the mixture was heated at 220 ^oC for 3 h under air refluxing. The mixture was left to cool at room temperature. A light-brown mud-like precipitate was obtained upon adding acetone and centrifuging at 11000 rpm for 10 minutes. The product was collected through centrifuging (8000 rpm, 5 min), washed two times with acetone and ethanol, and then redispersed in water.

2.2.6 Characterization

Transmission electron microscope (TEM) images were taken using Philips Tecnai T12 microscope at an accelerating voltage of 120 kV. The samples for TEM observation were supported on a copper grid with a carbon micro-grid. Before depositing samples onto the copper grid, the TiO_2 nanocrystals were washed at least 5 times with acetone to remove DEG from the samples thoroughly.

Powder X-ray diffraction (XRD) patterns were measured using a PANalytical Empyream diffractometer with Cu Kα radiation λ = 1.5406 Å with a graphite monochromator (40 kV, 40 mA). The Fourier transform infrared spectroscopy (FT-IR) spectra were acquired using a Nicolet 6700 FTIR spectrometer.

X-ray photoelectron spectroscopy (XPS) characterization was carried out on a Kratos AXIS ULTRADLD XPS system equipped with an Al Kα monochromated X-ray source and a 165-mm mean radius electron energy hemispherical analyzer. Absorption measurements were performed using a UV–vis spectrophotometer (HR2000CG-UV-NIR, Ocean Optics).

2.2.7 Bandgap calculation

The energy of the bandgap (E_g) was calculated for each sample using Tauc plot of $(\alpha h\nu)^2$ vs. $h\nu$, where α is the absorption coefficient, h is Plank constant, and ν is the wavenumber. The value of $h\nu$ is obtained by converting the wavelength (λ) value. The energy band gap was obtained from the intercept of the extrapolated linear part of the curve with the energy axis.

2.2.8 Preparation of N- TiO_2/HEC film on glass/paper substrate

An HEC stock solution was prepared by dissolving 1 g HEC in 30 ml H_2O and then heating the mixture at 80 ^oC for 3 h. Typically, the 5 ml N-doped TiO2 solution, 5 ml from the HEC stock solution, and 2 ml EG were mixed thoroughly and sonicated for 1 h before film deposition. The mixture was then drop-casted onto a 50 x 65 mm glass substrate (washed and sonicated in water, ethanol, and iso-propanol), or a thick white paper (blown only by air). The viscous mixture on top of the substrate was left at room temperature for one day to flatten. Afterward, the substrate was placed on a hot plate at 50 ^oC for 2-3 days to solidify the film. Additional HEC solution could be deposited on the top surface of the solid film and heated again at 50 ^oC, to create an additional layer of HEC that limits the diffusion of O_2 to the mixture.

2.2.9 Color-switching process

Photoirradiation was performed using a typical laboratory 365nm UV lamp. A laser diode (405 nm) operated with a power supplier (120 mΩ) was used for the UV-light handwriting. The letters and patterns were photo-printed on the rewritable film using

photomask upon UV-light irradiation. The photomask was produced by ink-jet printing on a plastic-transparent using a commercial laser-printer.

2.3 Results and discussion

2.3.1 Synthesis and characterization of N-doped TiO_2 nanocrystals

The synthesis of N-doped TiO_2 nanocrystals involves high-temperature hydrolysis of titanium tetrachloride ($TiCl_4$) in the presence of urea as a nitrogen source and diethylene glycol as a solvent. The mixture was heated at 220 ^oC for 3 hours to produce colloidal irregular nanocrystals with an average size approximately below 5 nm, as shown in the transmission electron microscopy (TEM) image in Figure 2.1a. The collected nanocrystals have an excellent dispersibility in polar solvents such as water, ethanol, and isopropanol. X-ray powder diffraction (XRD) analysis in Figure 2.1b confirms the anatase phase of the crystalline N-doped TiO_2 nanocrystals, where all diffraction peaks were indexed to anatase titania with cell constants of a= 3.7852 Å and c= 9.5139 Å (JCPDS card no. 21-1272). The broadening nature of the diffraction peaks in the XRD pattern is an indication of low crystallinity and small sizes of the nanocrystals. The Sherrer formula ($\tau = k\lambda/(\beta\cos\theta)$) was employed to calculate the domain size of the product, where τ is the average crystalline domain size, k is the shape factor with a typical value of 0.9, λ is the X-ray wavelength (0.1548 nm), β is the line broadening full width at half maximum (FWHM) peak height of the (101) peak, and θ is the Bragg angle. The calculated average domain size is approximately 3.38 nm, which is in good agreement with the observed nanocrystals' sizes on the TEM image (Figure 2.1a).

The formation mechanism of the N-doped TiO_2 nanocrystals is depicted in Figure 2.2. In a typical synthesis of colloidal TiO_2 nanocrystals,[12–14] $TiCl_4$ is injected into a DEG solution to release hydrochloric acid and form a clear mixture of stable glycolate precursor (Ti-DEG) (scheme S1).[27] The formation reaction is followed by the hydrolysis of the glycolate precursor at an elevated temperature to bind the hydroxyl group (-OH) with the Ti complex forming a new $Ti(OH)_n(OCH_2CH_2OCH_2CH_2OH)_{(4-n)}$ moieties. At the same time, urea starts to decompose at around 170 ^oC to produce NH_3 and isocyanic acid (HNCO), and the latter reacts with the OH groups in $Ti(OH)_n(OCH_2CH_2OCH_2CH_2OH)_{(4-n)}$ to replace it with amine groups ($Ti\text{-}NH_2$).[28–30] The last step of the formation of N-doped TiO_2 nanocrystals involves a condensation reaction of the $Ti\text{-}NH_2$ complexes to release a water molecule and form a new Ti-NH-Ti bond, as shown in reaction 5. In the absence of urea, the condensation reaction of Ti-DEG moieties will end-up with a Ti-O-Ti bonding between the complexes instead of the chemically attached NH molecules. It is worth noting that due to the short time and the presence of a minimal amount of water during the hydrolysis reaction, a large amount of DEG molecules will not be chemically bound to the titania nanocrystals, but instead physically absorbed onto the nanocrystal surface, as it will be elucidated later.

2.3.2 Photoreversible color switching of N-doped TiO_2 nanocrystals

When an aqueous dispersion of N-doped TiO2 nanocrystals was irradiated with a UV-light source (365 nm) for 1 min, the color of the solution has transformed immediately from whitish color to black/dark blue color, as shown in the inset of Figure 2.1c. The colloidal dispersion could retain this black color for a long duration (hours)

under ambient conditions before it returns to its original color. We noticed that this color-switching behavior occurs not only to the colloidal dispersion of N-doped TiO_2 nanocrystals but also to their thin-film coating on a glass slide, as demonstrated in Figure 2.1c. To prepare the composite film, we drop-casted a mixture of hydroxyethyl cellulose (HEC), ethylene glycol (EG), and the synthesized N-doped TiO_2 nanocrystals on a glass substrate, followed by drying in the air (Figure 2.1c).[9,14] The coated material showed a broadband absorption between 400-800 nm (Figure 2.1c). The solid film showed an increment of transmittance (up to 45 %) upon irradiating it with a 365 nm UV-light source for 30 min. In contrast, the transmission faded away after leaving the film at room temperature for 24 hours, returning to its original values. The photoresponsive color switching from whitish to black/dark blue could be repeated for more than 30 times without losing coloring ability or decreasing response time.

The coloration and decoloration time and reversibility of the N-doped TiO_2 solid-film were further investigated, as shown in Figure 2.3a. We measured the transmission of the solid-film under different UV-light irradiation time. The transmission intensity gradually increased with increasing irradiation time, reaching a maximum transmittance within ~60 s, demonstrating the rapid color-change response of the N-doped TiO_2 system. However, when the solid black film was heated in air at 50 ^oC, the transmission gradually decreased until it fully recovered to its original transmittance after 12 min (Figure 2.3b). The stability of the N-doped TiO_2 was also investigated by studying the reversibility of the coloring (UV irradiation) and decoloring (heating at 50 ^oC) of the solid film for more than 30 repeated cycles (Figure 2.3c). There were no noticeable changes in the film

transmittance after several consecutive coloration-decoloration cycles. These results elucidate the high stability and excellent reversibility of the N-doped TiO_2 film.

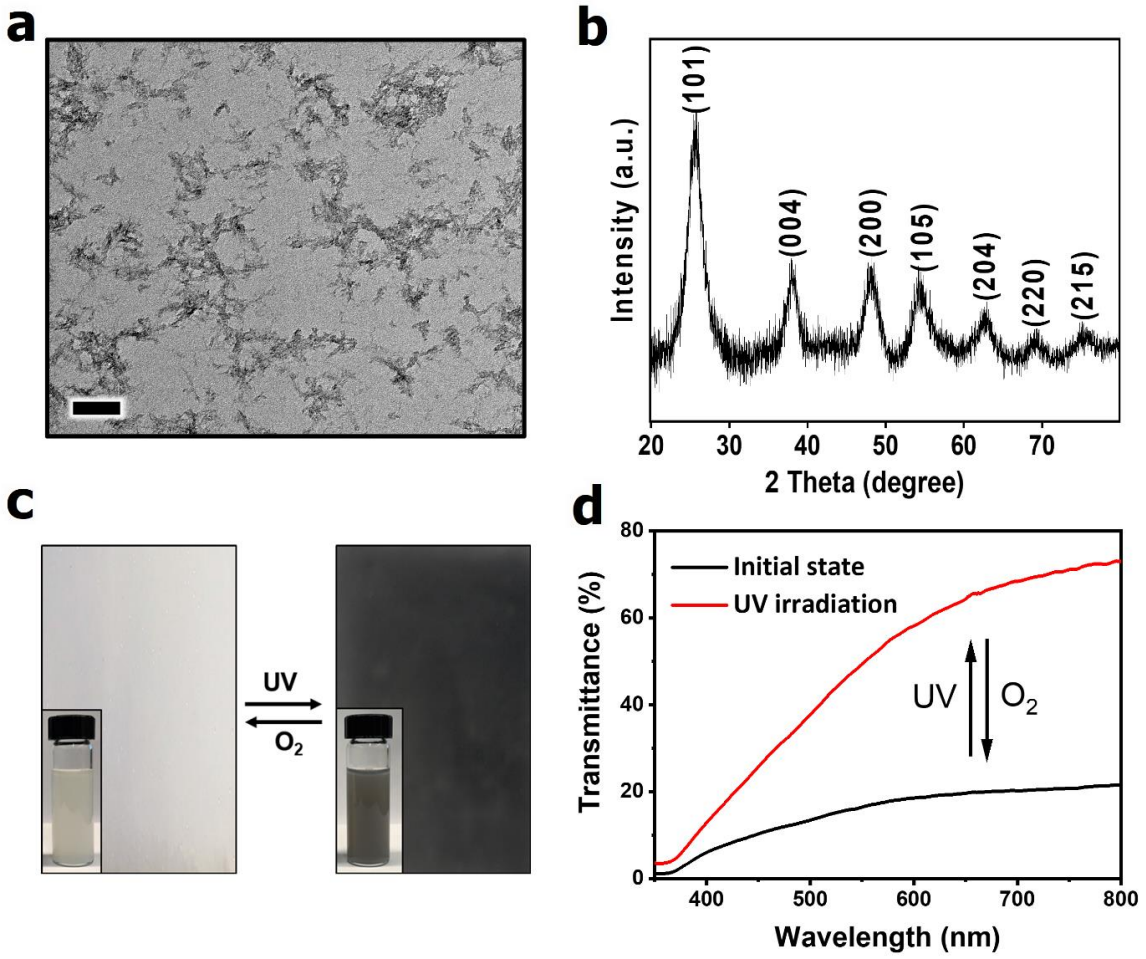

Figure 2.1 (a) TEM image of N-doped TiO_2 nanocrystals. (b) XRD pattern of N-doped TiO_2 nanocrystals indexed with anatase phase titania. (c) Digital photographs of N-doped TiO_2 film on a glass substrate, showing the film in its initial state under ambient condition (left) and after irradiation with UV-light for 1 min (right) (a paper background was used with the digital images of the films). Inset in (c): digital photographs of an aqueous dispersion of N-doped TiO_2 nanocrystals in a glass vial before irradiation and after irradiation for 1 min. (d) UV-vis transmission spectra of N-doped TiO_2 film before after UV-light irradiation for 1 min. The wavelength for the used UV-light is 365 nm. Scale bar: 50 nm.

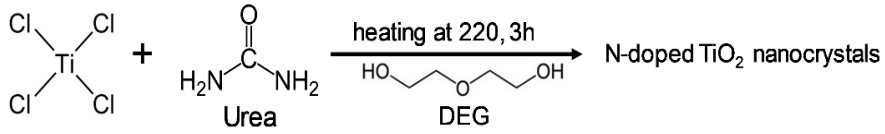

Formation of Ti-DEG precursor:

$TiCl_4 + 4HOCH_2CH_2OCH_2CH_2OH \rightarrow Ti(OCH_2CH_2OCH_2CH_2OH)_4 + 4HCl$ **(1)**

Hydrolysis of Ti-DEG precursor:

$Ti(OCH_2CH_2OCH_2CH_2OH)_4 + nH_2O \rightarrow Ti(OH)_n(OCH_2CH_2OCH_2CH_2OH)_{(4-n)} + nHOCH_2CH_2OCH_2CH_2OH$ **(2)**

Urea decomposition at 170 °C:

$NH_2CONH_2 \rightarrow HNCO$ (isocyanic acid) $+ NH_3$ **(3)**

$2Ti(OH)_n(OCH_2CH_2OCH_2CH_2OH)_{(4-n)} + HNCO \rightarrow (OH)_{(n-1)}(OCH_2CH_2OCH_2CH_2OH)_{(4-n)}Ti\text{-}NH_2 + CO_2$ **(4)**

Condensation reactions:

$2(OH)_{(n-1)}(OCH_2CH_2OCH_2CH_2OH)_{(4-n)}Ti\text{-}NH_2 \rightarrow (OH)_{(n-1)}(OCH_2CH_2OCH_2CH_2OH)_{(4-n)}Ti\text{-}NH\text{-}Ti(OCH_2CH_2OCH_2CH_2OH)_{(4-n)}(OH)_{(n-1)} + H_2O$ **(5)**

$2Ti(OH)_n(OCH_2CH_2OCH_2CH_2OH)_{(4-n)} \rightarrow (OH)_{(n-1)}(OCH_2CH_2OCH_2CH_2OH)_{(4-n)}Ti\text{-}O\text{-}Ti(OCH_2CH_2OCH_2CH_2OH)_{(4-n)}(OH)_{(n-1)} + H_2O$ **(6)**

Figure 2.2 Proposed schematic mechanism for the formation of N-doped TiO_2 nanocrystals in the DEG high-temperature reaction in the presence of urea.

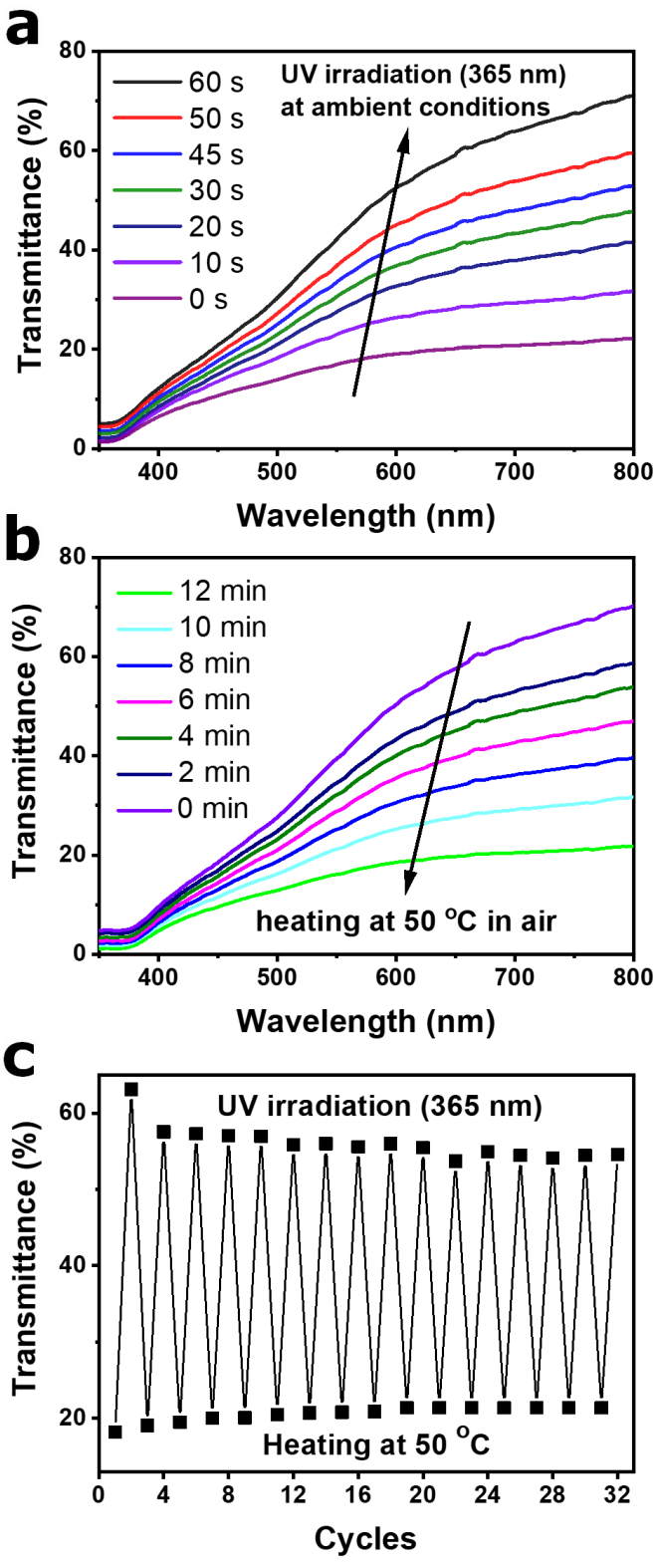
a
Transmittance (%)
Wavelength (nm)
60 s
50 s
45 s
30 s
20 s
10 s
0 s
UV irradiation (365 nm)
at ambient conditions
b
Transmittance (%)
Wavelength (nm)
12 min
10 min
8 min
6 min
4 min
2 min
0 min
heating at 50 °C in air
c
Transmittance (%)
Cycles
UV irradiation (365 nm)
Heating at 50 °C

Figure 2.3 (a) UV-vis absorption spectra of N-doped TiO_2 film under UV-light irradiation with evolving irradiation time, illustrating the decrease in film transmission with time. (b) UV-vis absorption spectra of N-doped TiO_2 film under heating at 50 ^oC in air, showing the decoloring process with time. (c) A plot of the absorption at 650 nm versus the number of cycles of repeating UV-light irradiation and heating at 50 ^oC of N-doped TiO_2 film.

2.3.3 Mechanism of photocatalytic color-switching of N-doped TiO_2 nanocrystals

To understand the color switching mechanism of N-doped TiO_2, we performed a series of fundamental studies to examine their intrinsic properties. Firstly, we measured the bandgap energies for various metal-doped and undoped TiO_2 nanocrystals, following the same high-temperature hydrolysis synthesis of N-doped TiO_2 nanocrystals (with only introducing a metal salt to the reaction to conduct metal doping or just reacting DEG and $TiCl_4$ to synthesize undoped TiO_2 nanocrystals, see supporting information).[13] Figure 2.4a shows the corresponding UV-vis diffuse reflectance spectra of TiO_2, Ba-doped TiO_2, Cu-doped TiO_2, and N-doped TiO_2 nanocrystals. All samples have an apparent absorption in the visible region between 400 and 600 nm.[31] With Kebelka-Munk function against photon energy, the band gaps of TiO_2, Ba-doped TiO_2, Cu-doped TiO_2, and N-doped TiO_2 nanocrystals were estimated as 3.18, 3.10, 3.08, and 2.96 eV, respectively (Figure 2.4b). The results suggest that the band gaps energy of TiO_2 nanocrystals follows the trend of undoped >Ba >Cu >N. Also, our estimated bandgap of N-doped TiO_2 agrees with the reported values of nitrogen-doped TiO_2 nanomaterials.[31–34] Our nitrogen doping method uses urea as a source of nitrogen molecules, which is known to dope N atoms in TiO_2 nanocrystals under high synthetic temperature, eventually decreasing the bandgap of TiO_2 and shifts its optical absorption to the visible region.[30,33,35]

XPS analysis provides valuable insights into the electronic and structural features of N-doped TiO_2. Both undoped and N-doped TiO_2 nanocrystals possess a carbon background peak at 284.8 eV, as shown in their C1s XPS spectrum (Figure 2.5a). This carbon peak could be attributed to the residual carbon obtained from DEG decomposition

during the high-temperature synthesis or adsorbed CO_2 molecules present in the air. The absence of carbon ion characteristics peak at around 281.8 eV confirms that carbon doping did not occur in the N-doped TiO_2 and TiO_2 nanocrystals.[36] The characteristic N 1s peak also confirmed nitrogen doping in the N-doped TiO2 nanocrystals at 398.28 eV (Figure 2.5b). The nitrogen characteristic peak was not present in the N 1S spectrum of the undoped TiO_2 nanocrystals. N 1s peak at 398.28 eV is attributed to the interstitial sites of N in the lattice structure of TiO_2 nanocrystals (in the form of O-Ti-N).[31,35] O 1s spectra for the undoped TiO_2 and N-doped TiO_2 nanocrystals were also compared in Figure 2.5c. The undoped TiO_2 nanocrystals showed three characteristic peaks at 530, 531.24, and 532.8 eV corresponding to Ti-O, Ti-OH, and C-O bonds, respectively. The N-doped TiO_2 nanocrystals showed three characteristic peaks at 529.8, 530.84, and 532.56 eV corresponding to Ti-O, Ti-OH, and C-O bonds, respectively. The C-O peak could be associated with the surface modification of N-doped TiO_2 with DEG molecules, which contain C-O bonds. The second peak corresponding to Ti-OH bonds on both samples indicates the formation of the hydroxyl group on TiO_2 nanocrystals, mainly due to the adsorbed glycol groups on TiO_2 nanocrystals surface.[37] Additionally, a small shift is noticed on the Ti-O peak from 530 eV of the undoped TiO_2 nanocrystals to 529.8 eV of the N-doped TiO_2 nanocrystals, which might indicate the presence of oxygen vacancies in the N-doped TiO_2 lattice structure.[38] Such features were previously proved to present in TiO_2 nanocrystals, especially when doping occurred during the synthesis.[14,15] Oxygen vacancies act as sacrificial electron donors in the photocatalytic TiO_2 color-switching

system, improving its performance by enhancing the charge separation during light excitation. [14,15]

To confirm the N-doped TiO_2 color-switching mechanism, we performed XPS Ti 2p measurements of N-doped TiO_2 nanocrystals before and after UV-irradiation (Figure 2.5d), which are expected to illustrate the chemical and electronic structures of Ti^{+4} species in the N-doped TiO_2 lattice structure. Two peaks attributed to the binding energies of Ti $2p_{3/2}$ and Ti $2p_{1/2}$ were observed for both samples (Figure S2). Upon UV irradiation, the original Ti $2p_{3/2}$ peak at 458.6 eV broadened and shifted to 458.17 eV, indicating the presence of multiple oxidation states of Ti on the surface of the nanocrystals. The narrow peak of Ti $2p_{3/2}$ before UV irradiation suggests that only the Ti^{4+} oxidation state exists. For the UV irradiated sample, two peaks were found after the deconvolution of the Ti $2p_{3/2}$ peak by Gaussian simulation, one of which at 458.07 eV can be attributed to the reduced species (Ti^{3+}).[21,22,38,39] By comparing both peak areas, we estimated the approximate content of Ti^{3+} on the N-doped TiO_2 nanocrystals surface to be ~ 64% when it was irradiated with UV light. These results confirm that the UV-induced color-switching of the N-doped TiO_2 system is associated with the reduction of Ti^{4+} to Ti^{3+} on the nanocrystal surfaces. At the same time, the reversible decoloration process is caused by the oxidation of Ti^{3+} to Ti^{4+} by ambient oxygen molecules.

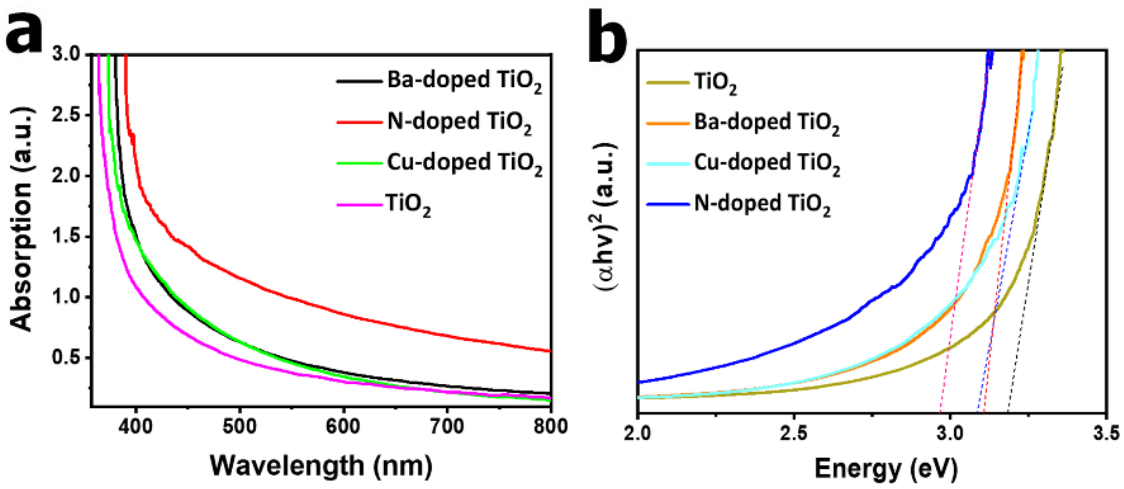

Figure 2.4 (a) Diffuse reflectance UV-vis absorption spectra of undoped TiO_2, and N, Cu, and Ba-doped TiO_2 nanocrystals. (b) Tauc plot of $(\alpha h\nu)^2$ vs. $h\nu$ for bandgap calculation of undoped TiO_2, and N, Cu, and Ba-doped TiO_2 nanocrystals.

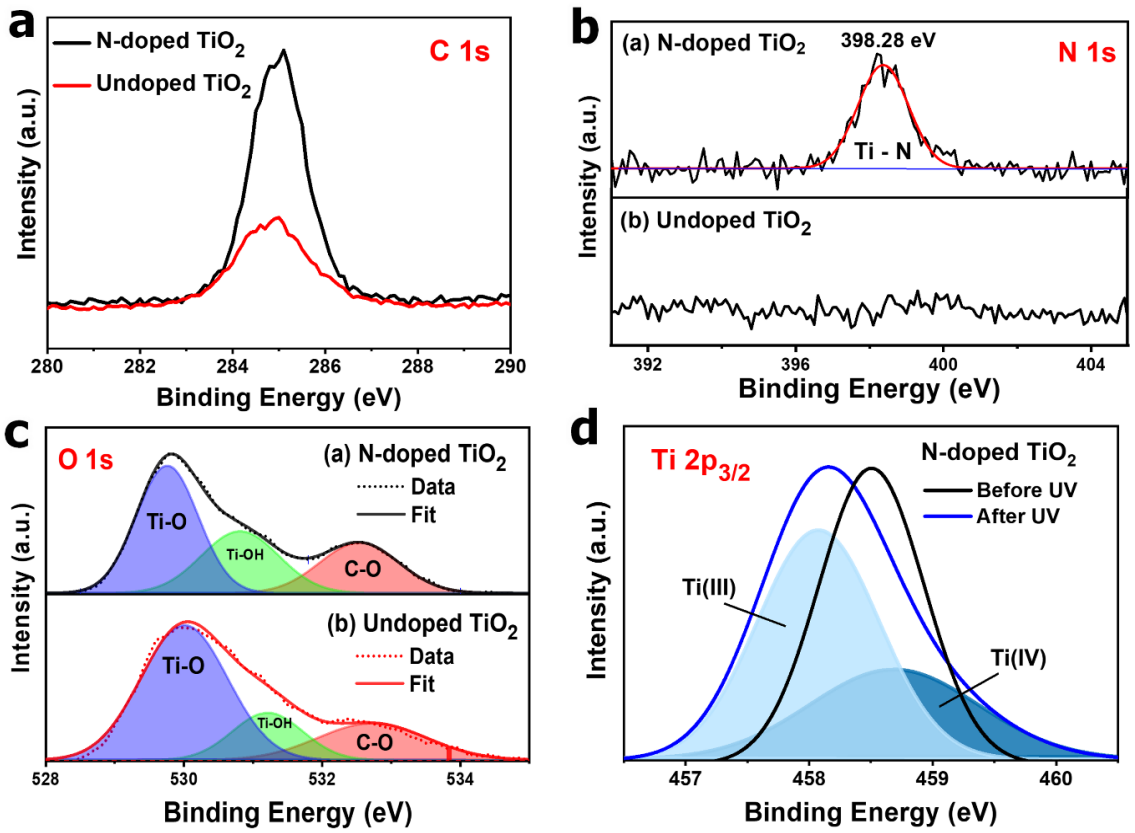

Figure 2.5 XPS spectra of (a) C 1s, (b) N 1s, (c) O 1s, and (d) Ti 2p orbitals of N-doped TiO_2 and undoped TiO_2 nanocrystals. A gaussian simulation was used to deconvolute XPS peaks.

.

Next, we investigated the key reasons for the rapid reduction of Ti^{4+} species and the higher stability of Ti^{3+} species in the N-doped TiO_2 system comparing to pristine samples. Our previous studies demonstrated that the DEG molecules bound to the surface of TiO_2 nanocrystals could act as internal sacrificial electron donors (SEDs).[40] To further understand the roles of these DEG molecules in the N-doped TiO_2 system, we employed FTIR measurements to characterize the functional groups of DEG and N-doped TiO_2 nanocrystals (Figure 2.6a). FTIR spectra of DEG molecules showed absorption peaks at 892, 1051, 1122, and 1230 cm-1 corresponding to $–OC_2H_4$, C-O, C-C-O, and C-O-C stretching modes, respectively. The FTIR peaks for DEG matched well with the major peaks in N-doped TiO_2, indicating the adsorption of DEG moieties on the N-doped TiO_2 surface. However, the peak at 1051 cm^{-1} for C-O stretching in pure DEG was red-shifted to 1078 cm^{-1} in the N-doped TiO_2 sample, indicating the formation of C-O-Ti bond, which suggests to the chemisorption of DEG on the nanocrystal surface.[41,42]

Previous reports demonstrated that chemically-bounded organic groups are more effective as SEDs than simply mixing organic SEDs and titanium dioxide.[40,43–45] Figure 2.6b schematically illustrates the main reasons for the superior holes scavenging of chemically-bonded glycol groups in the N-doped TiO_2 system. As shown in Figure 2.6b, DEG molecules chemisorbed onto the N-doped TiO_2 surface as alkoxide species, while they physically absorbed onto the nanocrystal surface through hydrogen bonding. Alcohol molecules are known to probe reactive sites on semiconductor metal oxides. Particularly, polyhydroxy alcohols such as polyols molecules are more effective in scavenging h^+ than monohydroxy alcohols, due to the presence of more reactive sites. In

the case of the N-doped TiO_2 system, surface-bound DEG molecules are believed to scavenge the photogenerated h^+ through a deprotonation process:[43–45] Although both chemisorbed and physisorbed glycol groups work as SEDs in the TiO_2 photocatalytic system, the chemisorbed molecules are known to be more effective in scavenging photogenerated h^+ on titania surfaces. The reason could be understood by looking at the rate of recombination, hole trapping, and scavenging processes of the photocatalytic system. As shown in Figure 2.6b, in both cases, the scavenging process starts with the excitation step by light (1). Generally, the rate of h^+ and e^- recombination on titania surfaces takes 10-20 ps[45] (2). In the physisorption case, the hole trapping process (3) takes 100-300 fs, which precedes the scavenging reaction (4) that takes several ns. However, when the polyols are chemically bound onto titania surfaces, the h^+ will be directly trapped by the bridging oxygen of the alkoxide complex (ketyl radical), which will quickly lose C-H proton to the environment, producing a metastable titanium-bound-olyl radical.[45] Overall, the hole scavenging process by the chemisorbed polyhydroxy molecules (5) is much faster (< 100 fs) than the hole scavenging by the physisorbed ones (several ns) and the recombination of e^- and h^+ (2) (10-20 ps).[45]

Based on the above results, we concluded that the N-doped TiO_2 system obtains rapid color-switching response due to its more effective chemisorbed polyol molecules that produce a higher number of e^- than the pristine titanium dioxide. By superior scavenging of h^+, the generated e^- will effectively diffuse into N-doped TiO_2 surface lattice to reduce Ti^{4+} to Ti^{3+}, yielding the observed black/dark blue color. However, the reduced surface of N-doped TiO_2 nanocrystals is significantly more stable than all

reported UV-light reduced TiO_2 materials (which were shown to oxidize in atmospheric air instantly). To further investigate this phenomenon, we studied the effects of the physisorbed polyol molecules on the N-doped TiO_2 system. The coloring process of the nanocrystals under UV-light irradiation was studied when the physisorbed polyols are removed through washing the nanocrystals with acetone for several cycles. The removal process was monitored by FTIR measurements. The coloring process and its stability were observed before and after UV irradiation. Figure 2.6c shows the digital images of the N-doped TiO_2 nanocrystals dispersed in water after each number of acetone washings. As shown in Figure 2.6d, the peaks of N-doped TiO_2 corresponding to -C-O stretching, OH bending, and -CH_2 bending, that well-matched with DEG characteristic peaks, gradually decreased with two consecutive cycles of washing with acetone, confirming the gradual removal of polyol molecules from the nanocrystal surface. However, the characteristic peaks did not show any further significant change after the fourth cycle of acetone washing, suggesting the complete removal of physisorbed DEG molecules. The N-doped TiO_2 nanocrystals remained well-dispersed in aqueous solution even after the complete removal of the physisorbed polyol molecules (i.e., after four times washing with acetone). The N-doped TiO_2 nanocrystals could not disperse at all after calcining the sample at 600 ^oC for 4 h in an ambient atmosphere, which is due to the complete removal of the chemisorbed polyol molecules from the material through combustion. These results indicate that the chemisorbed polyol molecules are responsible for the excellent dispersion of the N-doped TiO_2 nanocrystals, with very minimal contribution from the physisorbed ones. The existence of chemisorbed polyols on the N-

doped TiO_2 surface after four cycles of acetone washing is also consistent with the presence of the C-O stretching characteristic peak in the FTIR spectra in Figure 2.6d.

The color-switching behavior of the N-doped TiO_2 nanocrystal dispersion varies with the degree of washing, with the intensity of the black-coloring becoming lesser after two cycles of washing, as shown in Figure 2.6c (ii). After the complete removal of the physisorbed polyol groups by four times of washing, the nanocrystal dispersion did not turn black after UV irradiation. It only showed a slight yellowish color (Figure 2.6c (iii)). Interestingly, we could still obtain a modest color-change from white to black of N-doped TiO_2 nanocrystals dispersion under UV irradiation after two times of washing, as seen in Figure 2.6c (ii). However, we found that this color-change is extremely unstable, vanishing entirely in less than 5 min in an atmospheric environment (Figure 2.6e). These observations demonstrate the contributions of the physisorbed DEG molecules in stabilizing the trapped electrons in the $-Ti^{3+}-O^{2-}$ configuration after UV irradiation. The stabilization of the reduced Ti species helps to substantially maintain the black-coloring of the N-doped TiO_2, which could be attributed to the physisorbed polyols limiting the diffusion of oxygen molecules onto the TiO_2 surface, thereby reducing the oxidation rate of the Ti^{3+} species and slowing down their decoloration process.

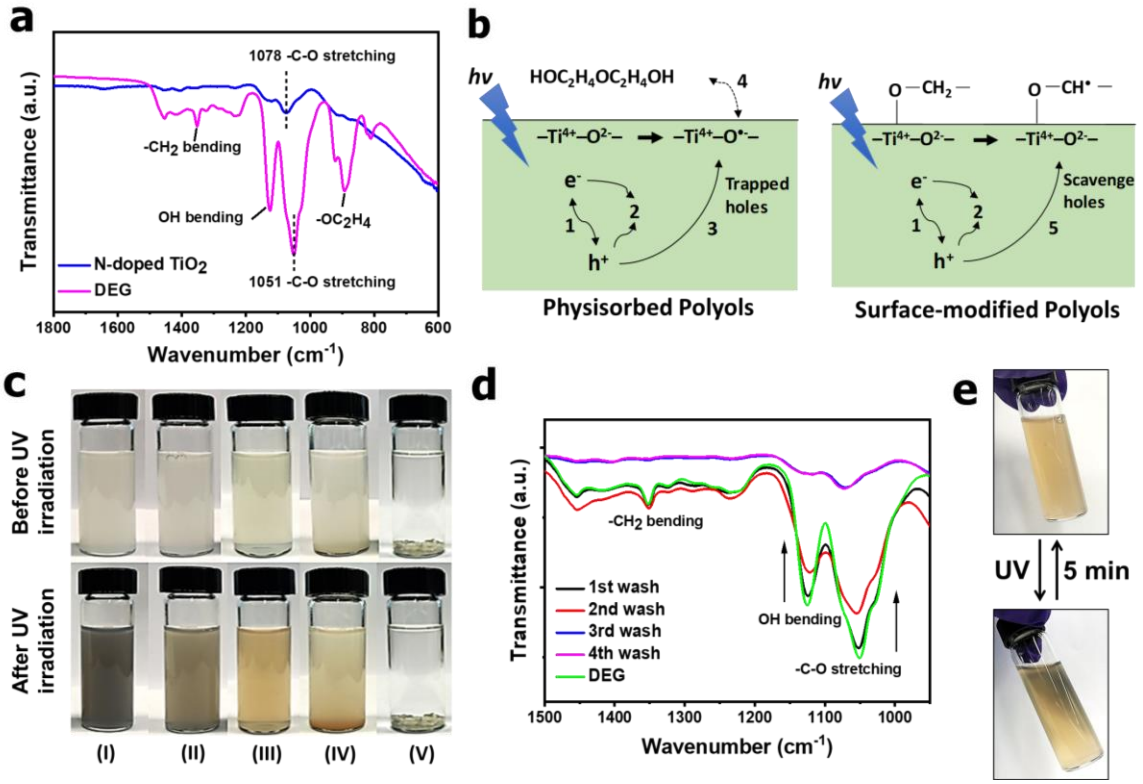

Figure 2.6 (a) FTIR spectra of N-doped TiO_2 nanocrystals after three cycles of washing with acetone (blue) and DEG (pink). (b) Mechanism of electron holes scavenging by physisorbed polyol and chemisorbed polyol molecules. (c) Digital images of N-doped TiO_2 aqueous solution before and after UV-light irradiation with (i) no acetone washing, (ii) two times washing with acetone, (iii) three times washing with acetone, (iv) four times washing with acetone, and (v) after calcination at 600 ^{o}C for 4 h in air. (d) FTIR spectra for DEG as a reference and N-doped TiO_2 nanocrystals after a certain number of washing with acetone. (e) an aqueous solution of N-doped TiO_2 nanocrystals after two times of acetone washing under UV-light irradiation, showing its unstable coloring that vanishes within 5 minutes.

XPS O1s spectra and the color-switching performance of the N-doped TiO_2 system indicate that the number of physisorbed DEG molecules is considerably higher in N-doped TiO_2 than the undoped TiO_2 nanocrystals, which could be attributed to the high absorption affinity of N-doped TiO_2 lattice towards polyhydroxy alcohols than the undoped nanocrystals due to the presence of many defect sites (oxygen vacancies) after nitrogen doping.[14,15] Generally, defect sites number increases with increasing the doping of nitrogen atoms. For example, previous studies reveal that ethylene glycol molecules can capture up to 85% of the undercoordinated defect sites on the titania surface. [43,44] Additionally, the holes scavenging rate was found to be directly proportional to the number of absorbed alcohol groups (SEDs) in the TiO_2 surface. Therefore, the N-doped TiO_2 showed superior color-switching performance than undoped TiO_2 nanocrystals.[43,44]

Overall, the color-switching mechanism of N-doped TiO_2 nanocrystals is based on two oxidation states of Ti exhibiting different optical properties. The overall mechanism of the photocatalytic color-switching of N-doped TiO_2 nanocrystals is depicted in Figure 2.7. Titania, as a semiconductor material, is known to absorb photons when excited with light energy that equals or larger its bandgap energy, leading to the generation of e^- in its conduction band and h^+ in its valence band. In the absence of electron and hole scavengers, most of the generated electrons and holes will recombine within a few nanoseconds. However, in the N-doped TiO_2 system, most e^- will move freely on the material's surface due to the effective scavenging of holes by the chemically-attached polyol molecules, leading to the photoreduction and trapping of the

generated e^- by Ti(IV). A possible overall mechanism for the photoreversible color-switching of N-doped TiO_2 is as following:

$$\text{N-doped } TiO_2 + h\nu \longrightarrow e^-_{CB} + h^+_{VB} \quad (1)$$

$$e^-_{CB} + \text{Ti(IV)} \longrightarrow \text{Ti(III)} \quad (2)$$

$$(HOC_2H_4OC_2H_4OH) + h^+_{VB} \longrightarrow (HOC_2H_4OC_2H_4OH)^+ \quad (3)$$

$$\text{Ti(III)} + O_2 \longrightarrow \text{Ti(IV)} + O_2^- \quad (4)$$

Photoexcitation of N-doped TiO_2 nanocrystals results in the generation of electrons and holes (eq 1). The electrons will reduce Ti(IV) into Ti(III) (eq 2), while the surface-modified polyol molecules will act as holes scavengers (eq 3). Finally, oxygen molecules will oxidize Ti(III) species to Ti(IV) (eq 4). The excellent overall efficiency of Ti(IV) to Ti(III) conversion is attributed to the doping of TiO_2 with nitrogen atoms and the superior holes scavenging by the chemically-attached polyol molecules. However, the reversible oxidation process of Ti(III) to Ti(IV) is prolonged due to the stabilizing effects by the physisorbed polyols molecules that will minimize the diffusion of oxygen molecules to the surface of the nanocrystals.[21,25]

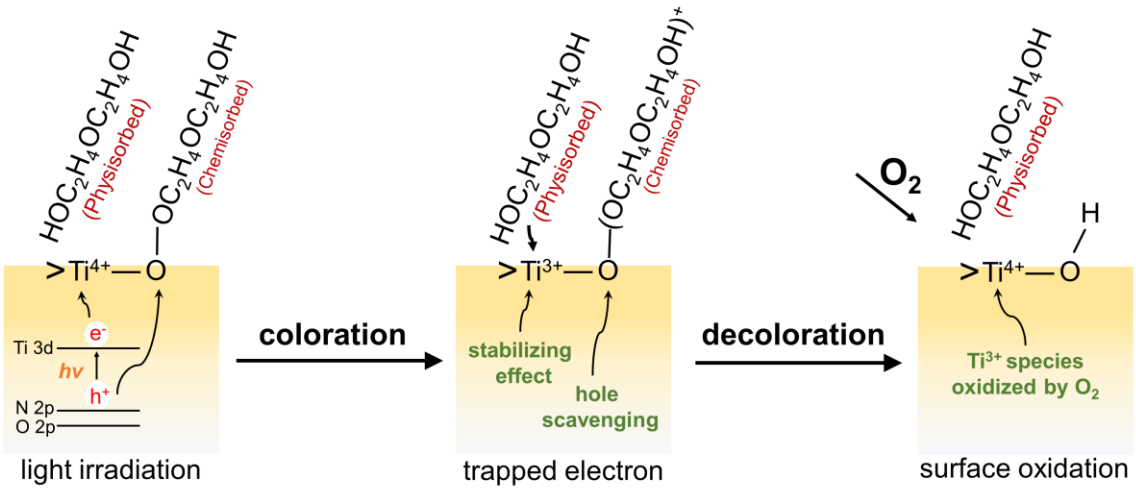

Figure 2.7 Representative drawing for the overall photoreversible color-switching mechanism of N-doped TiO_2 nanocrystals.

2.3.4 A rewritable paper based on N-doped TiO_2 nanocrystals

The new catalytic color-switching system was employed as a responsive-material for rewritable light-printing applications. N-doped TiO_2 has considerable advantages over other rewritable paper materials, namely because of its facile synthesis, rapid response, low toxicity, low price, and the absence of organic dyes or inorganic metals. A coated film of N-doped TiO2/HEC mixture was drop-casted onto a glass substrate (5 cm x 6.5 cm) to form the rewritable platform. Various letters and patterns were printed on the N-doped TiO_2/HEC film by UV-light irradiation in accompanying with a photomask, which was pre-produced by ink-jet printing on a transparent plastic film (Figure 2.8a). As seen in Figure 2.8b-e, the exposed areas of the photomask turned to black/dark blue after light printing. At the same time, the unexposed regions retained their colorless appearance, hence replicating the letters/patters from the photomask onto the rewritable film. This rewritable process demonstrated high-resolution printing through producing complex shapes and letters, even replicating letters with a font size of less than 10. The durability of the printing was tested in Figure 2.9, where it showed excellent stability and eligibility for reading under office light conditions even after 12 hours. This system is therefore suitable for temporary recording applications, such as temporary labels and writing boards for restaurants, conference rooms, and others. The letters will disappear entirely after maintaining the film in ambient condition for ~24 h. However, the erasing process could be accelerated by heating the film at 50 ^{o}C for ~15 min (Figure 2.9). We will dedicate more efforts to further enhance the printing lifespan by covering the top surface

of the rewritable paper with more layers of non-toxic HEC or other materials such as PDMS, which will help in further reduction of oxygen diffusion into the rewritable paper.

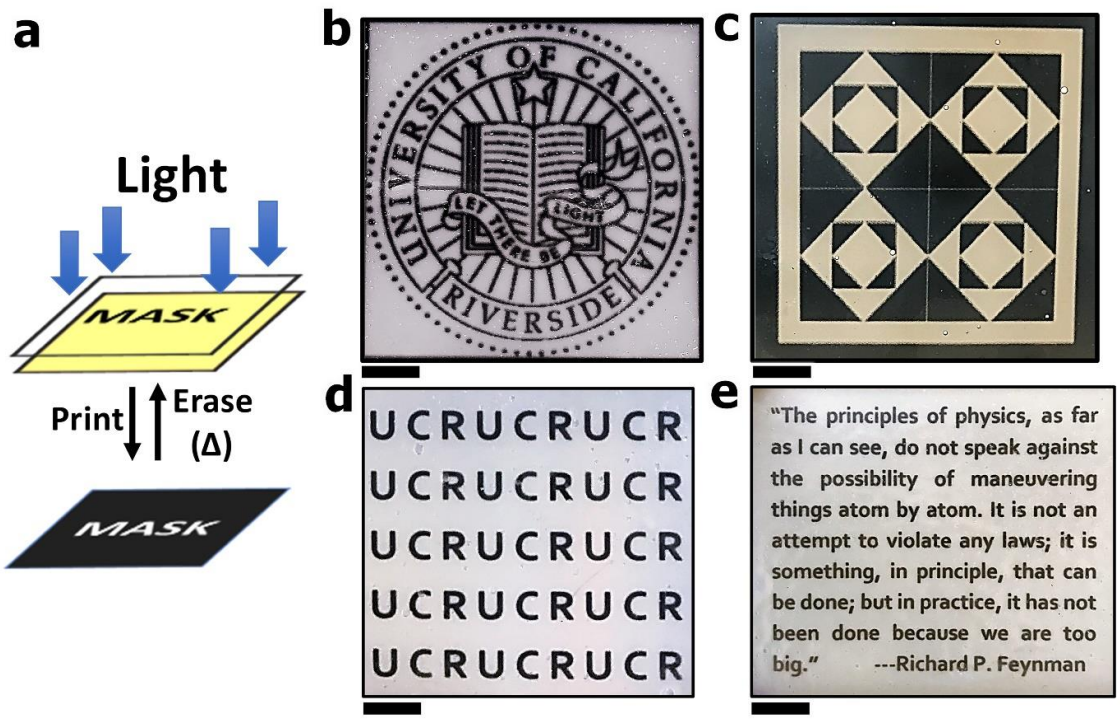

Figure 2.8 Light-printing with 360 UV lamp using intricate patterns on the rewritable paper (glass as a substrate). Scale bar is 1 cm.

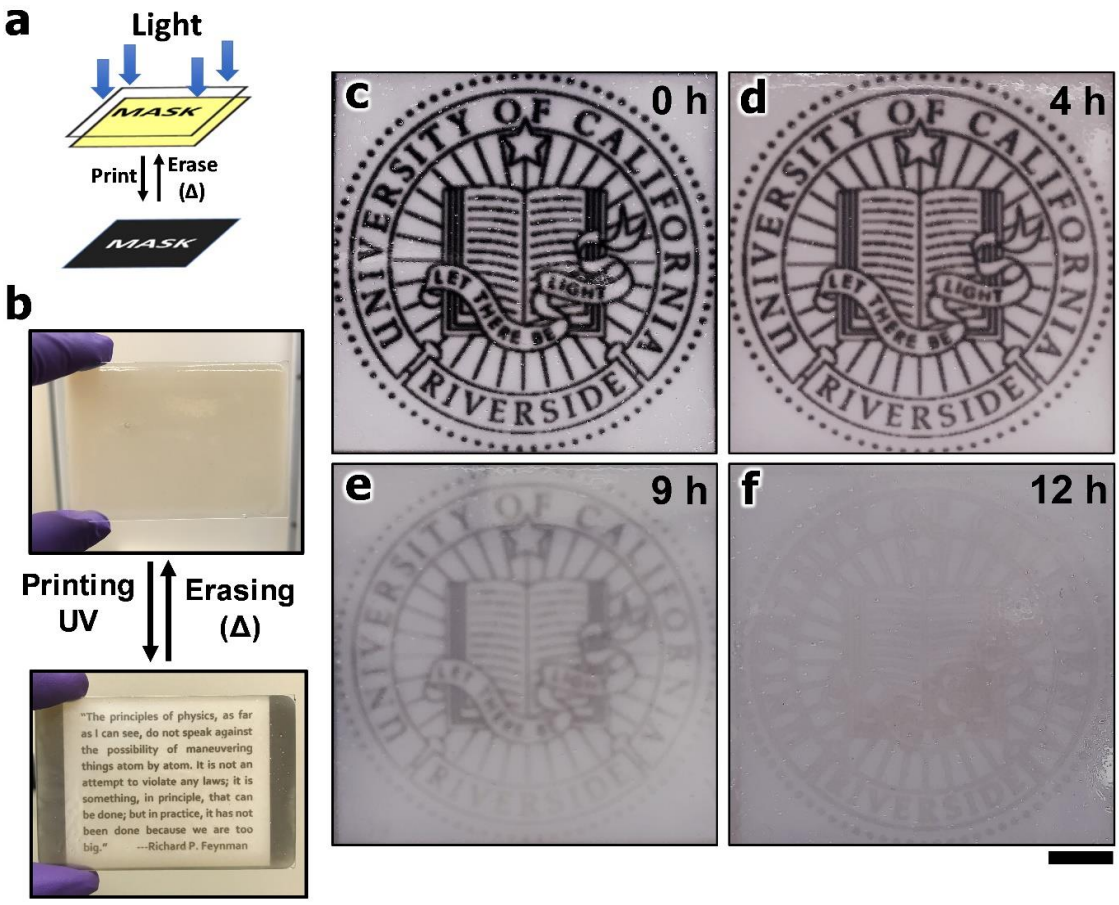

Figure 2.9 (a) Schematic representation of the rewritable paper printing with UV-light on a glass substrate through a photomask. (b) digital images of the rewritable paper writing and erasing on the glass as a substrate. (c) a printed patter on the rewritable paper coated on glass substrate showing the fading of color with a different interval of times under ambient conditions. Scale bar is 1 cm.

The applicability of the N-doped TiO_2 system as a rewritable paper was also investigated with methylene blue (MB) dye mixture. Similar to previous reports, the N-doped TiO_2 could be used as a photocatalyst that will reduce MB to its leuco methylene blue (LMB) upon irradiation with UV-light.[9,14,15] The printing was produced using a photomask as illustrated in Figure 2.10. The regions exposed to light irradiation rapidly turned to the colorless form of LMB, while the unexposed areas retained their original color of MB (Figure 2.10). The N-doped TiO_2/HEC/MB film showed superior performance than all reported MB based rewritable paper, where the system achieved rapid writing with excellent resolution and coloration lifetime for more than one week (Figure 2.10).

The coating of N-doped TiO_2/HEC mixture could be extended into a commercial paper substrate because of the high dispersity and low toxicity of the N-doped TiO_2 nanocrystals. In contrast to previous coating methods that involved additional pretreatments and highly toxic materials, a mixture of N-doped TiO_2/HEC/EG was directly coated onto a paper substrate (5 cm X 6.5 cm) without any additional treatments. Complicated letters and patters could also be light-printed onto the commercial paper substrate using a pre-printed photomask (Figure 2.11a &d). The printed letters showed excellent resolution and contrast. We further demonstrated the applicability of N-doped TiO_2 based rewritable paper by using a blue laser beam pen (405 nm) for freehand writing (Figure 2.11b&c). Instant freehand writing was performed on the paper substrate, which produced a good contrast writing of the word (NANO), as shown in Figure 2.11c. The writing with a laser pen also confirms the excellent absorption of the N-doped TiO_2

nanocrystals in the visible-light region. The cyclability of the N-doped TiO_2 paper-based substrate was investigated, as shown in Figure 2.11e. Although a very complex pattern with small features was used, there was only a slight decrease of color contrast and writing quality after 50 cycles of writing and erasing, confirming the excellent cyclability of the N-doped TiO_2 paper-based rewritable film.

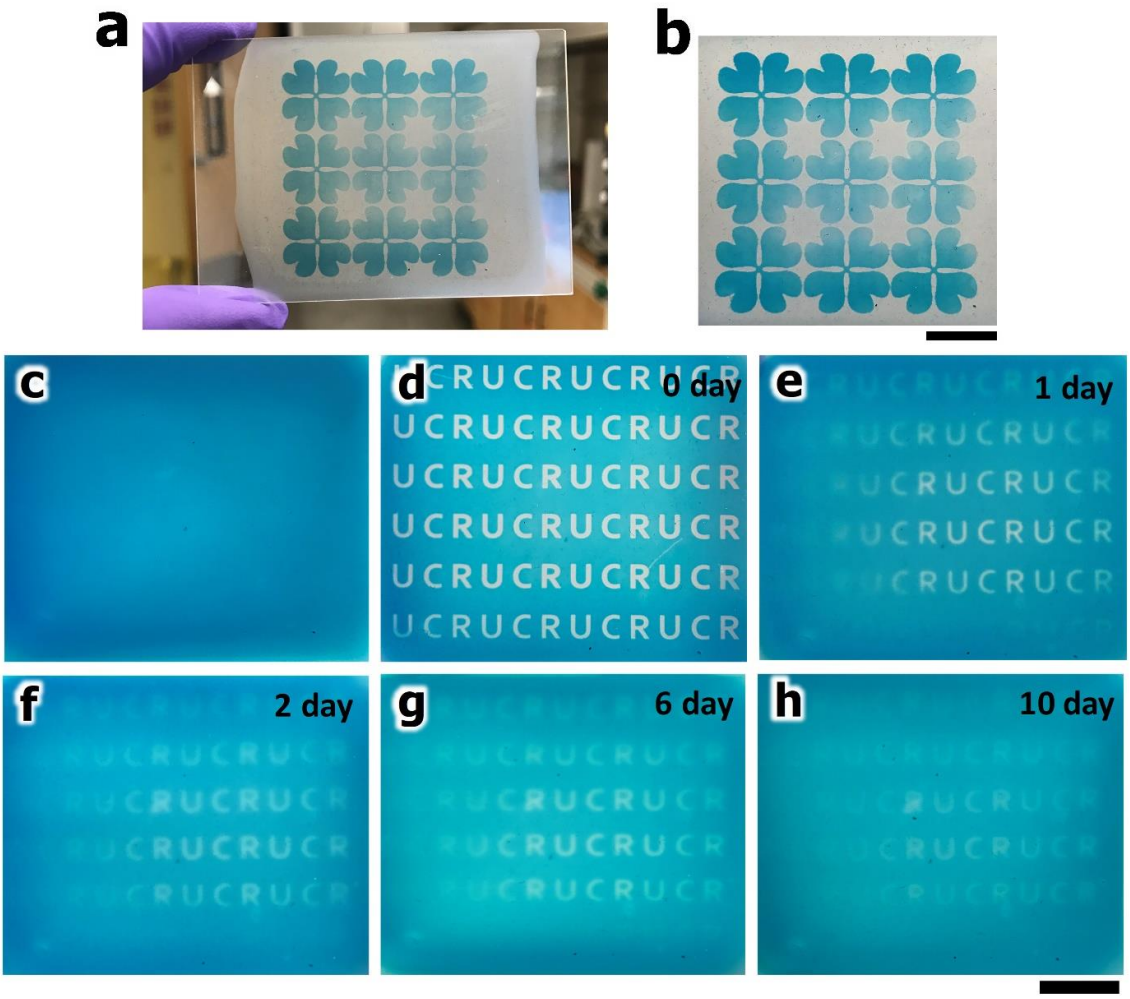

Figure 2.10 (a) and (b) digital images of prints on MB/N-doped TiO_2 film on a glass substrate. (c-h) images of the printed letters after several days under ambient conditions. Scale bar is 1 cm.

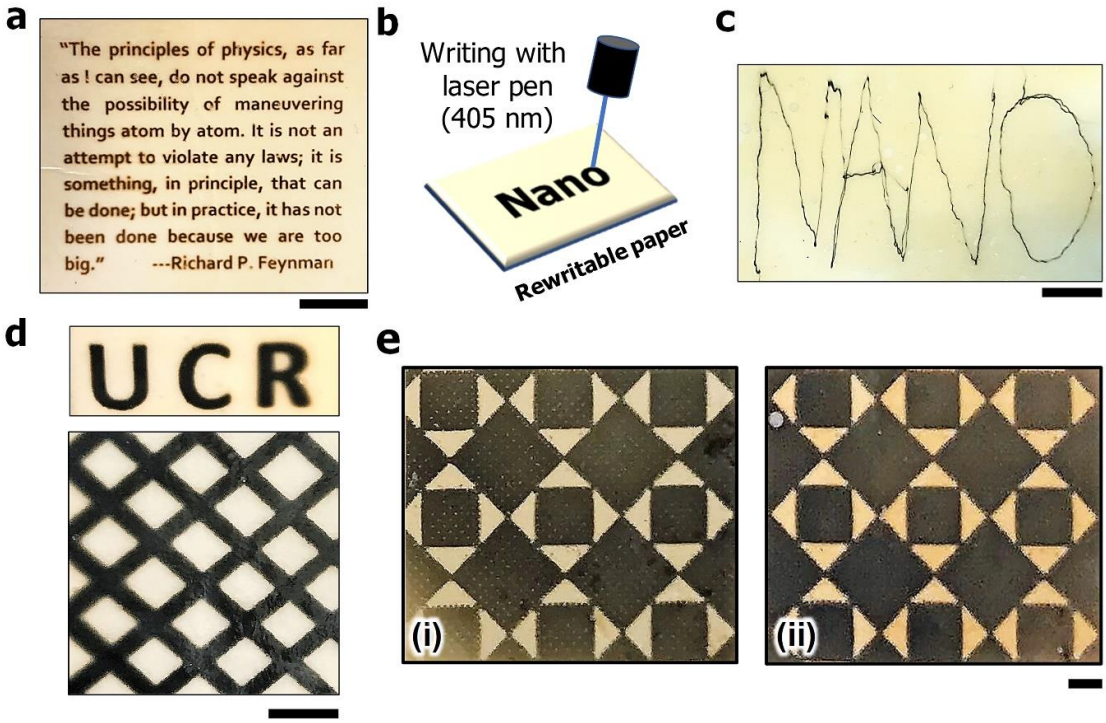

Figure 2.11 (a) Light-printing with 365 UV lamp on the rewritable paper substrate. (b) schematic illustration of the instant freehand writing using a laser pen on the rewritable paper (paper as a substrate). (c) Letters written using a violet laser beam (405 nm) on the rewritable paper (paper as a substrate) under ambient condition. (d) digital images of photo-printed complex patterns and letters on the rewritable paper using commercial paper as the substrate. (e) digital photos of a photo-printed complex pattern (i) first printing (ii) and same printing after 50 consecutive writing and erasing cycles using commercial paper as the substrate. Scale bar: 1 cm.

2.4 Conclusions

We reported herein the synthesis of new N-doped TiO_2 nanocrystals that can undergo photoreversible color-switching from black/dark blue to colorless state quickly and stably. The coloring-decoloring mechanism is attributed to the redox reaction of Ti(III) to Ti(IV) on the titania surface. Our results confirm that upon irradiating the N-doped TiO_2 system with UV-light, the photogenerated electrons will reduce Ti(III) species into Ti(IV). At the same time, the reversible oxidation process occurs in the presence of oxygen molecules. The rapid response and excellent stability of the coloration process have never been reported to any TiO_2 photo-reduced system. We attributed this superior performance to the following reasons: (i) the nitrogen doping and the chemisorbed polyol groups on the nanocrystal surface that induced during the high-temperature hydrolysis reaction in the presence of urea and DEG, which significantly contribute to the material strong absorption and superior h^+ scavenging(faster coloration response); (ii) higher physisorption of polyol molecules due to the presence of many defects (oxygen vacancies) on the nanocrystals that reduces the oxidation rate of Ti(III) by limiting the contact between the reduced species and oxygen molecules (diffusion limiting step). A rewritable paper film was fabricated based on N-doped TiO_2 nanocrystals, which could be deposited onto various substrates such as glass, plastic, and paper. The printing on the rewritable paper using glass as a substrate produced various intricate patterns and letters in excellent resolution and long duration. With regular paper as a substrate, the writing could be performed by a laser pen (405 nm), demonstrating instant freehand writing with excellent stability. The low toxicity, low price, scalability of

material production, excellent dispersion, and the elimination of dyes or inorganic materials make the N-doped TiO_2 system a superb candidate not only for rewritable paper applications but also for optical data recording, smart window, light and oxygen sensors, and many others.

2.5 References

[1] Worldwatch Institute, "Paper production levels off," can be found under http://www.worldwatch.org/paper-production-levels-environmental-footprint-still-high, **2015**.

[2] Green America's better paper project, "Paper Production and Consumption Facts," can be found under http://www.thepaperlessproject.com/facts-about-paperthe-%0Aimpact-of-consumption/, **2017**.

[3] M. I. Khazi, W. Jeong, J. M. Kim, *Adv. Mater.* **2018**, *30*, 1–22.

[4] K. C. Naeem, A. Subhakumari, S. Varughese, V. C. Nair, *J. Mater. Chem. C* **2015**, *3*, 10225–10231.

[5] A. Kishimura, T. Yamashita, K. Yamaguchi, T. Aida, *Nat. Mater.* **2005**, *4*, 546–549.

[6] Y. Wang, M. Li, Y. Zhang, J. Yang, S. Zhu, L. Sheng, X. Wang, B. Yang, S. X. A. Zhang, *Chem. Commun.* **2013**, *49*, 6587–6589.

[7] H. Wu, Y. Chen, Y. Liu, *Adv. Mater.* **2017**, *29*, 1–5.

[8] R. Klajn, P. J. Wesson, K. J. M. Bishop, B. A. Grzybowski, *Angew. Chemie - Int. Ed.* **2009**, *48*, 7035–7039.

[9] W. Wang, N. Xie, L. He, Y. Yin, *Nat. Commun.* **2014**, *5*, 1–7.

[10] L. Sheng, M. Li, S. Zhu, H. Li, G. Xi, Y. G. Li, Y. Wang, Q. Li, S. Liang, K. Zhong, et al., *Nat. Commun.* **2014**, *5*, 1–8.

[11] Y. Ma, P. She, K. Y. Zhang, H. Yang, Y. Qin, Z. Xu, S. Liu, Q. Zhao, W. Huang, *Nat. Commun.* **2018**, *9*, 1–8.

[12] W. Wang, M. Ye, L. He, Y. Yin, *Nano Lett.* **2014**, *14*, 1681–1686.

[13] W. Wang, L. Liu, J. Feng, Y. Yin, *Small Methods* **2018**, *2*, 1700273.

[14] W. Wang, Y. Ye, J. Feng, M. Chi, J. Guo, Y. Yin, *Angew. Chemie - Int. Ed.* **2015**, *54*, 1321–1326.

[15] D. Han, B. Jiang, J. Feng, Y. Yin, W. Wang, *Angew. Chemie - Int. Ed.* **2017**, *56*, 7792–7796.

[16] U. Joost, S. Andris, M. Oja, K. Smits, N. Do, A. Loot, M. Hirsima, M. Ja, *Chem Mater* **2018**, *30*, 8968–8974.

[17] M. Takeuchi, G. Martra, S. Coluccia, M. Anpo, *J. Phys. Chem. C* **2007**, *111*, 9811–9817.

[18] J. M. Coronado, A. J. Maira, J. C. Conesa, K. L. Yeung, V. Augugliaro, J. Soria, *Langmuir* **2001**, *17*, 5368–5374.

[19] S. Livraghi, M. Rolando, S. Maurelli, M. Chiesa, M. C. Paganini, E. Giamello, *J. Phys. Chem. C* **2014**, 22141−22148.

[20] Q. Zhu, Y. Peng, L. Lin, C. M. Fan, G. Q. Gao, R. X. Wang, A. W. Xu, *J. Mater. Chem. A* **2014**, *2*, 4429–4437.

[21] L. Bin Xiong, J. L. Li, B. Yang, Y. Yu, *J. Nanomater.* **2012**, *2012*, DOI 10.1155/2012/831524.

[22] M. S. Hamdy, R. Amrollahi, G. Mul, *ACS Catal.* **2012**, *2*, 2641–2647.

[23] J. N. Schrauben, R. Hayoun, C. N. Valdez, M. Braten, L. Fridley, J. M. Mayer, *Science (80-.).* **2012**, *336*, 1298 LP – 1301.

[24] A. I. Kuznetsov, O. Kameneva, A. Alexandrov, N. Bityurin, K. Chhor, A. Kanaev, *J. Phys. Chem. B* **2006**, *110*, 435–441.

[25] X. Wang, X. Li, S. Aya, F. Araoka, Y. Ishida, A. Kikkawa, M. Kriener, Y. Taguchi, Y. Ebina, T. Sasaki, et al., *J. Am. Chem. Soc.* **2018**, *140*, 16396–16401.

[26] X. Wang, X. Li, S. Aya, F. Araoka, Y. Ishida, A. Kikkawa, T. Aida, *J. Am. Chem. Soc.* **2018**, *140*, 16396–16401.

[27] X. Jiang, T. Herricks, Y. Xia, *Adv. Mater.* **2003**, *15*, 1205–1209.

[28] D. Mitoraj, H. Kisch, *Chem. Eur. J.* **2010**, 261–269.

[29] P. M. Schaber, J. Colson, S. Higgins, D. Thielen, B. Anspach, J. Brauer, *Thermochim. Acta* **2004**, *424*, 131–142.

[30] M. Factorovich, L. Guz, R. Candal, *Adv. Phys. Chem.* **2011**, *2011*, DOI 10.1155/2011/821204.

[31] C. B. Xiaobo Chen, *Am. Chem. Soc.* **2008**, *130*, 5018–5019.

[32] R. Asahi, T. Morikawa, H. Irie, T. Ohwaki, *Chem. Rev.* **2014**, *114*, 9824–9852.

[33] S. A. Ansari, M. Khan, O. Ansari, *New J. Chem.* **2016**, *40*, 3000–3009.

[34] G. Yang, Z. Jiang, H. Shi, T. Xiao, Z. Yan, *J. Mater. Chem.* **2010**, *20*, 5301.

[35] D. Mitoraj, H. Kisch, *Angew. Chemie - Int. Ed.* **2008**, *47*, 9975–9978.

[36] X. Chen, L. Liu, P. Y. Yu, S. S. Mao, *Science (80-.).* **2011**, *331*, 746–750.

[37] I. Luciu, R. Bartali, N. Laidani, *J. Phys. D. Appl. Phys.* **2012**, *45*, DOI 10.1088/0022-3727/45/34/345302.

[38] R. Ren, Z. Wen, S. Cui, Y. Hou, X. Guo, J. Chen, *Sci. Rep.* **2015**, *5*, 10714.

[39] J. Pan, X. Wu, L. Wang, G. Liu, Q. Max, *Chem. Commun.* **2011**, *47*, 8361–8363.

[40] J. Feng, F. Yang, Y. Ye, W. Wang, X. Yao, Q. Fan, L. Liu, R. M. Aleisa, J. Guo, Y. Yin, *Nanoscale* **2019**, *11*, 19512–19519.

[41] G. Chen, J. Feng, W. Wang, Y. Yin, H. Liu, *Water Res.* **2017**, *108*, 383–390.

[42] D. Cordeiro, L. Vasconcelos, V. C. Costa, E. Henrique, M. Nunes, A. Claret, S. Sabioni, M. Gasparon, W. L. Vasconcelos, *Mater. Sci. Appl.* **2011**, *2*, 1375–1382.

[43] M. H. Du, J. Feng, S. B. Zhang, *Phys. Rev. Lett.* **2007**, *98*, 2–5.

[44] T. Tachikawa, Y. Takai, S. Tojo, M. Fujitsuka, H. Irie, K. Hashimoto, T. Majima, *J. Phys. Chem. B* **2006**, *110*, 13158–13165.

[45] I. A. Shkrob, M. C. Sauer, D. Gosztola, *J. Phys. Chem. B* **2004**, 12512–12517.

Chapter 3. Colorimetric Stress Sensor Based on Nanoparticles Deformation

3.1 Introduction

Pressure sensors are vital technologies used for musical, medical, and industrial applications. They are implemented to assess car crashes, analyze podiatry foot gait, monitor patient sleep patterns, and detect target force accuracy in competitive sports. The commercialized sensors are based on materials that possess resistivity changes or currents generation when a force, pressure, or mechanical stress are induced.[1–7] These materials however, are bulky and rigid (nonflexible), require flat surface contact, need electronic signals processing and electrical power, and cannot be implemented for large surface areas.[8–13] Plasmonic nanomaterials utilized for pressure sensing could overcome these current limitations [7,14,15], owing to their simple fabrication and detection techniques, higher compatibility with various fabrication processes, and comparable sensitivity and lower cost.[16]

Plasmonic pressure sensors are based on nanomaterials' plasmonic peak change and its perceivable color in response to mechanical stress.[14,17,18] Han et al. developed a colorimetric pressure sensor using AuNP chain-polymer composite film that, under mechanical stress, deforms and accordingly disassembles the embedded AuNP chains.[17] The interparticle distance in the AuNP chains expands as the film deforms, weakening the plasmonic coupling of the particles and hence changing the film color. The plasmonic AuNP band position is correlated with the film expansion rate, producing a proportional colorimetric response to mechanical stress. Increasing the applied force intensity and duration led to the increase of film deformation degrees, which is also proportional to the

disassembly extent (i.e., color shift) of the AuNP chains.[17] Fu et al. have developed another colorimetric stress sensor based on the orientational dependence of AuNRs LSPR properties to ordinary light. The sensor consists of a composite polymer matrix comprising highly dispersed AuNRs. The initial orientation of AuNRs changes from random to more ordered states upon applying external pressure, correlating the induced force with the variation of the AuNRs LSPR peak.[18] Another mechanochromic stress sensing approach is proposed by using inverse opals made of the shape-memory polymer matrix, which showed color-change memorization to fingertip pressing.[19]

However, the described pressure sensing technologies depend on composite films life-span, possess slow response time (or long duration of applying stress) and poor contrast, and are prone to environmental changes such as temperature and humidity. We report here the development of a colorimetric pressure sensor based on plasmonic nanoparticles' deformation that overcomes the limitations mentioned above. The pressure sensor consists of changing the color of Au@Ag@void@TiO_2 nanostructured materials by deforming the TiO_2 under a mechanical force. The color change is caused by changing the surrounding environment of the metallic Au@Ag NPs from air to TiO_2 after the deformation of the outer particle shell. TiO_2 and Au@Ag are used as the outer shell and the core-shell NPs because of its high refractive index and pronounced plasmonic properties, respectively. This system showed apparent color-change, especially with Au@Ag core-shell overall size around 55 nm. Simulation results and TEM and SEM images confirmed the change of the refractive-index mechanism. Changing the thickness of TiO_2 showed different color-change thresholds based on the applied force, where

increasing the overall thickness is directly proportional to the increase of the mechanical strength of the material (i.e., withstand higher pressure).

3.2 Materials and methods

3.2.1 Materials

$NH_3 \cdot H_2O$ (28wt%), $HAuCl_4$, acetonitrile, titanium butoxide, NaOH, $AgNO_2$, and ascorbic acid were purchased from Fisher Scientific. Trisodium citrate dihydrate (TSC), tetraethylorthosilicate (TEOS, 98%), ethanol, polyvinylpyrrolidone (PVP, Mw=10000), and hydroxypropyl cellulose (HPC) were purchased from Sigma-Aldrich. All chemicals were directly used without further purification. Solutions were prepared with water (18.2 MΩ/cm) produced from Milli-Q system (Millipore).

3.2.2 Characterizations

Transmission electron microscopy (TEM) was performed using a Tecnai T12 transmission electron microscope operating of 120 kV and JEOL JEM-2100 microscope operating at 200 kV. The samples for TEM observation were prepared by drop-casting a solution on a carbon film supported on a copper grid. Scanning electron microscopy (SEM) was performed on TESCAN Vega3 SBH. Energy-dispersive X-ray spectroscopy (EDS) mapping profiles were collected on a FEI Talos F200X transmission electron microscope operated at 200 kV. Optical absorption spectra were measured by Ocean Optics HR2000CG-UV-NIR spectrometer. The static pressure test was performed on DUKE Utility Press. The impact test was performed on Tubular Impact Tester BGD301. X-ray diffraction (XRD) patterns were measured using a PANalytical Empyream

diffractometer with Cu Kα radiation λ = 1.5406 Å with a graphite monochromator (40 kV, 40 mA).

3.2.3 Synthesis of Au nanoparticles

For the preparation of Au nanoparticles, 18 μl of $HAuCl_4$(2.5M) was added into 30 ml H_2O and heated to its boiling point. Then 1 ml TSC (3wt%) was injected rapidly into the boiling solution. After 1 h, the solution was cooled to room temperature. 3 ml of PVP(5wt%, Mw 10000) was added finally and left under room temperature condition and stirred for 12h. Au nanoparticles were collected by centrifugation and dispersed in 5 ml H_2O.

3.2.4 Synthesis of Au@SiO_2 core/shell nanoparticles

In a typical synthesis of Au@ SiO_2 core/shell nanoparticles, 4.8ml of the Au nanoparticles were mixed with 92 ml of ethanol, 12.4 ml of H_2O, 2.6 ml of $NH_3 \cdot H_2O$(28wt%) under stirring in room temperature. Subsequently, 3.44 ml of TEOS was added. After 4 h of reaction, the resulting Au@SiO_2 core/shell nanoparticles were collected by centrifugation, washed with ethanol and water, and dispersed in 20 ml of ethanol.

3.2.5 Synthesis of Au@void@TiO_2 yolk/shell nanoparticles

50mg of HPC was mixed with 32 ml of ethanol at room temperature. Meanwhile, 6 ml of ethanol, 2 ml of ACN, and 2 ml TBOT were mixed as a precursor. Then, 10ml of Au@SiO_2 core/shell nanoparticles, 14 ml of ACN, and 0.4 ml of $NH_3 \cdot H_2O$ (28wt%) was added to the HPC mixture. The precursor has added to the solution afterward. After 2 h of reaction, the resulting Au@SiO_2@TiO_2 core/shell nanoparticles were collected by

centrifugation, washed with water, and dispersed in 40 ml of water. Finally, 0.3 g of NaOH was added to the final solution and agitated for 12 h at room temperature. The resulting Au@void@TiO_2 yolk/shell nanoparticles were collected by centrifugation, washed with water, and dispersed in 40 ml of H_2O.

3.2.6 Synthesis of Au@Ag@void@TiO_2 yolk/shell nanoparticles

2 ml of Au@void@TiO2 yolk/shell nanoparticles were mixed with 10 ml of water, 10 ml of PVP (5 wt%, Mw 10000), 10 ml of ACN, and 0.5 ml of AA (0.1M) in room temperature. Then different volume (ml) of AgNO3 (0.1M) was injected dropwise into the solution using a digital flow pump at a rate of 35 μl/min with continuous stirring. After completing the injection, the mixed solution was stirred for 1 h. The resulting Au@Ag@void@TiO2 yolk/shell nanoparticles were collected by centrifugation, washed with water and ethanol, and dispersed in 20 ml of ethanol.

3.2.7 Fabrication of the pressure sensor film

The pressure sensor film based on the yolk/shell nanoparticles was made using air spray coating (airbrush). Transparent polyvinyl chloride (PVC) sheet (22×22×0.17mm) was used as a substrate film. Au@Ag@void@TiO2 yolk/shell nanoparticles were sprayed onto the substrate film with a total of 1ml volume. The distance between the tip of the airbrush nozzle and the substrate was around 200 mm.

3.2.8 Impact and static force test

The impact test of the sprayed film was performed using BGD301 DuPont impact tester. The film was placed at the bottom of the machine and then released the drop weight to hit the specimen. Impact energy was controlled by the drop height and weight

of the object. The drop height was 5, 10, 15, 20, 30, 40, and 50 cm. The impact weight is 250 g, 500 g, and 1000 g. The diameter of the pressure head was 5mm. The static test of the film was made with a manual press machine. The press was 1, 2, 3, and 4 tons. The diameter of the pressure head of the static test was 10mm.

3.3 Results and discussion

3.3.1 Principal design of the colorimetric pressure sensor

The overall mechanism of the colorimetric stress sensor is schematically represented in Figure 3.1. The primary mechanism is based on changing the LSPR properties of nanostructured materials in response to mechanical stress. Yolk-shell nanostructures are utilized as the responsive components of the sensor. These nanostructures are coated onto a substrate such as glass, plastic, and aluminum, to create a colorimetric pressure-responsive film. The design of the yolk-shell nanostructure comprises of yolk plasmonic nanoparticles such as Au, Au, or Au@Ag core-shell structure, and outer shell materials with a high refractive index such as TiO_2 and ZnO.

According to Mie theory, the optical absorption α of plasmonic NPs embedded in a medium of refractive index n is:

$$\alpha = \frac{18\pi Q n^3 \varepsilon_2/\lambda}{(\varepsilon_1 + 2n^2)^2 + \varepsilon_2^2}$$

where Q is the volume fraction of nanoparticles, and ε_1 and ε_2 are the cluster-size dependent dielectric constants, which are functions of the radius (r) and wavelength (λ). Mie's theory indicates that changing the refractive index (n) surrounding a plasmonic metallic NP will dramatically alter the optical properties of the NPs. Taking 70 nm AuNP

as an example, its extinction peak position gradually red-shifted from 530 nm up to 630 nm upon increasing the refractive index of its surrounding medium from n= ~1.0 (air) up to n=1.9 respectively.[20] As shown in Figure 3.1, the yolk plasmonic nanoparticles are surrounded by air (n= ~1.0) in a pre-deformed state (before applying mechanical stress). If an impact force is induced to the nanostructures' surface, the outer shell is expected to deform, resulting in the complete covering of the yolk plasmonic particles with the outer shell materials, hence changing the environment (i.e., refractive index) surrounding the plasmonic yolk particles from the air to the shell material. TiO_2 is used as the outer shell in the yolk-shell nanostructure owing to its high refractive index (1.9 – 2.5).[21] A higher refractive index will induce a greater red-shift of the plasmonic peak position, resulting in more pronounced optical change.

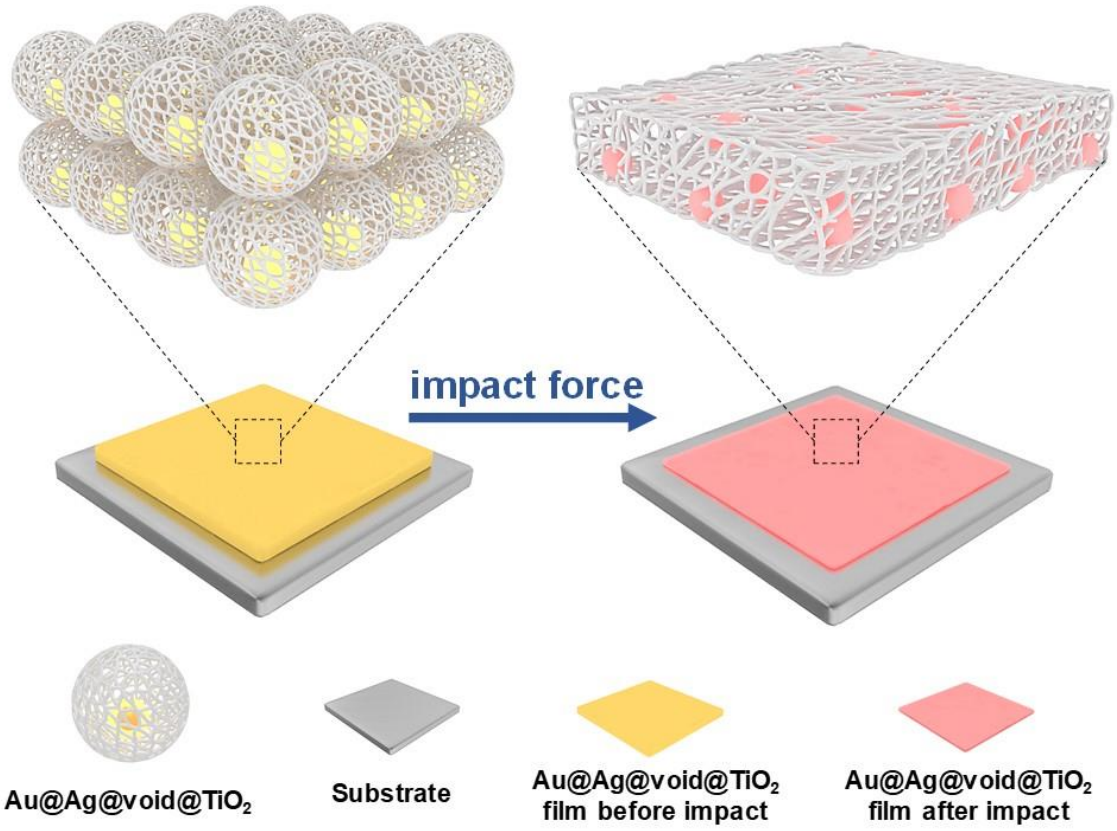

Figure 3.1 Schematic illustration of the colorimetric impact sensor based on the deformation of Au@Ag@void@TiO_2 nanostructured materials.

3.3.2 Synthesis of Au@Ag@void@TiO_2 nanostructures

The synthesis of the nanostructured materials follows a reported procedure.[22,23] As shown in Figure 3.2a, AuNPs (~20 nm) are coated first with SiO_2 followed by TiO_2 coating to form Au@SiO_2@TiO_2 NPs. A void inside the nanostructure is created by etching SiO_2 using NaOH solution. The final nanostructure of Au@Ag@void@TiO_2 is produced by the confined growth of Ag on Au. The deposition of Ag in the final structure is intended to blue-shift and increase the intensity of the plasmonic peak of AuNP, which will enhance the color-change contrast of the colorimetric film, as it will be illustrated later. TEM images of Au@SiO_2, Au@void@TiO_2, and Au@Ag@void@TiO_2 NPs are shown in Figure 3.2b, c, and d, respectively. EDS mapping and XRD analysis were obtained for Au@Ag@void@TiO_2 NPs, as shown in Figure 3.2(e-h) and Figure 3.3, respectively. The EDS maps of Ag and Au in Figure 3.2g and h confirm the coating of Ag on AuNP within the void space. XRD results also revealed the formation of Au@Ag core-shell structure, where all diffraction peaks are indexed with Au-Ag crystal structures. Additionally, the UV-vis absorption measurements revealed a plasmonic peak at 530 nm for Au@void@TiO_2 NPs (Figure 3.4), matching the plasmonic peak absorption of individual AuNP with ~ 20 nm size.[22,23] However, an increase in the plasmonic peak intensity and a blue-shift of its position is observed with the coating of Ag on Au, as shown in Au@Ag@void@TiO_2 UV-vis extinction. This indicates the uniform coating of Ag shell on AuNPs, as reported previously.[24,25] The blue-shift of Au plasmonic peak from 530 nm to 450 nm after Ag coating is responsible for the NPs

colloidal solution color-change from pink to yellowish color (inset images in Figure 3.2c and d).

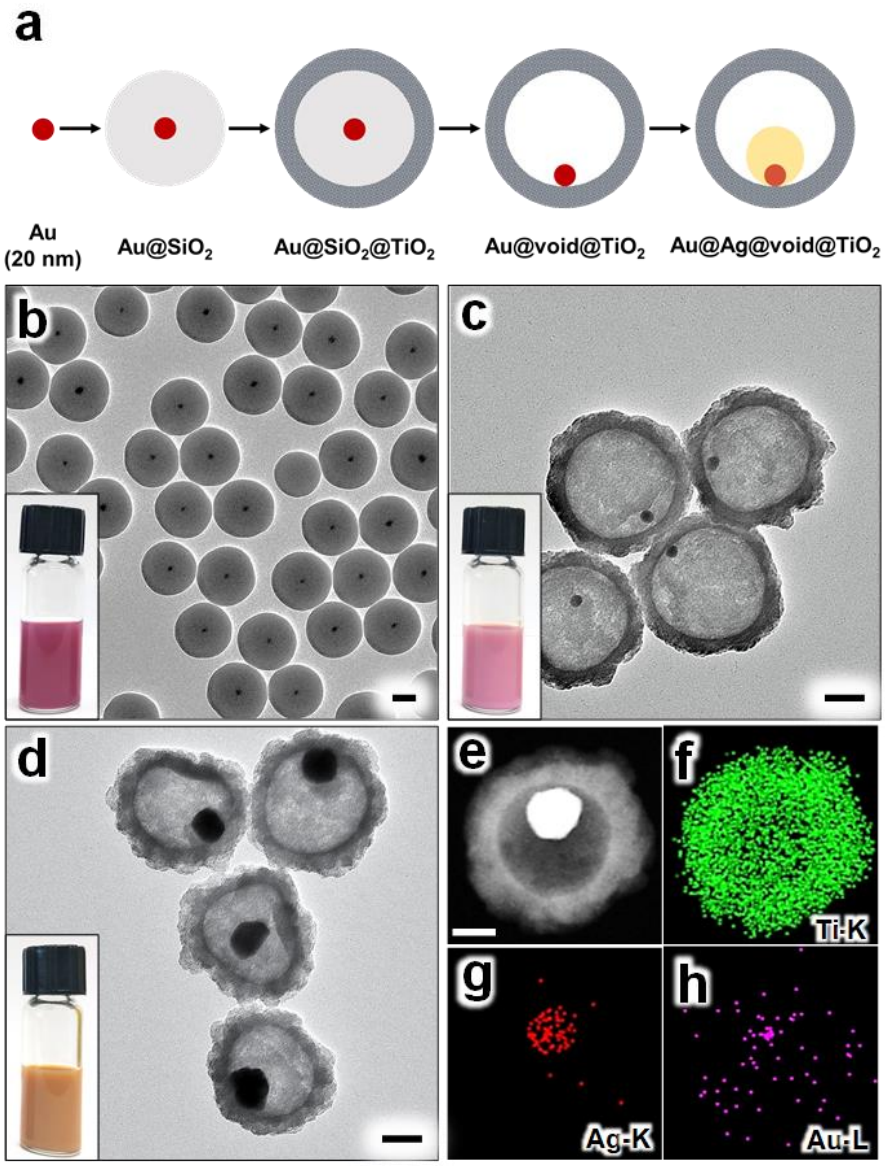

Figure 3.2 (a) Schematic representation of the synthesis procedure of Au@Ag@void@TiO_2: AuNPs sequentially coated with SiO_2 and TiO_2, followed by etching of SiO_2, and the confined growth of Ag shell on Au. TEM images and digital images of the aqueous solutions of (b) Au@SiO_2 NPs (c) Au@void@TiO_2 yolk-shell NPs (d) Au@Ag@void@TiO_2 yolk-shell NPs. (e) TEM image of Au@Ag@void@TiO_2 and its EDS maps of (f) Ti, (g) Ag, and (h) Au. Scale bar 50 nm.

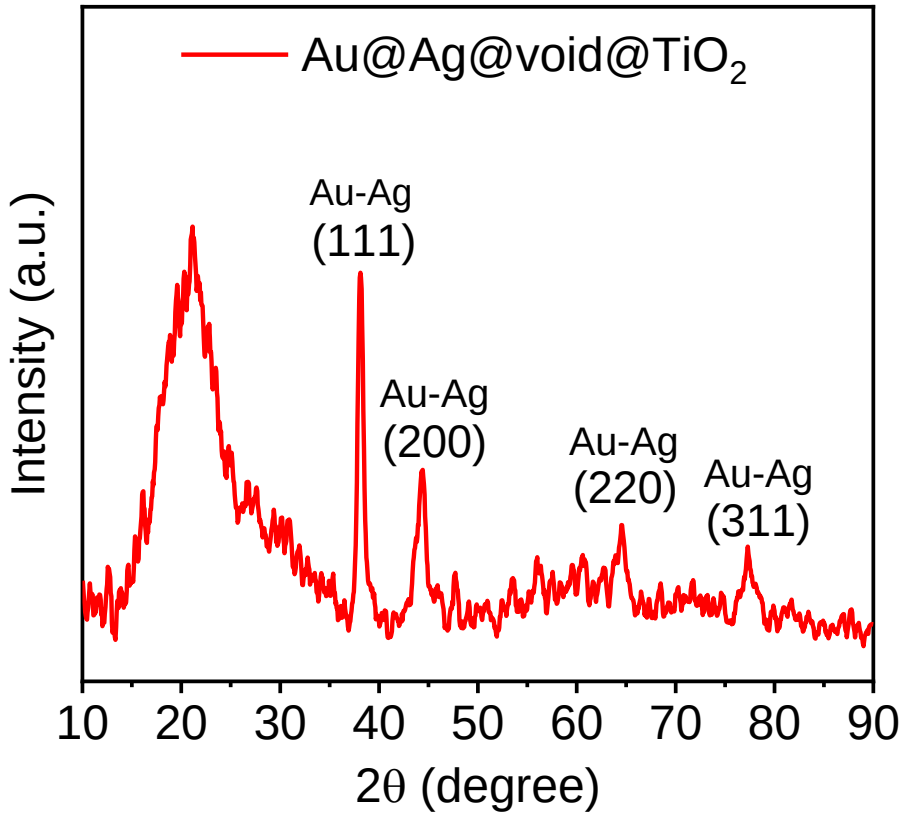

Figure 3.3 XRD pattern of Au@Ag@void@TiO_2 yolk-shell NPs indexed with Au-Ag crystal structures.

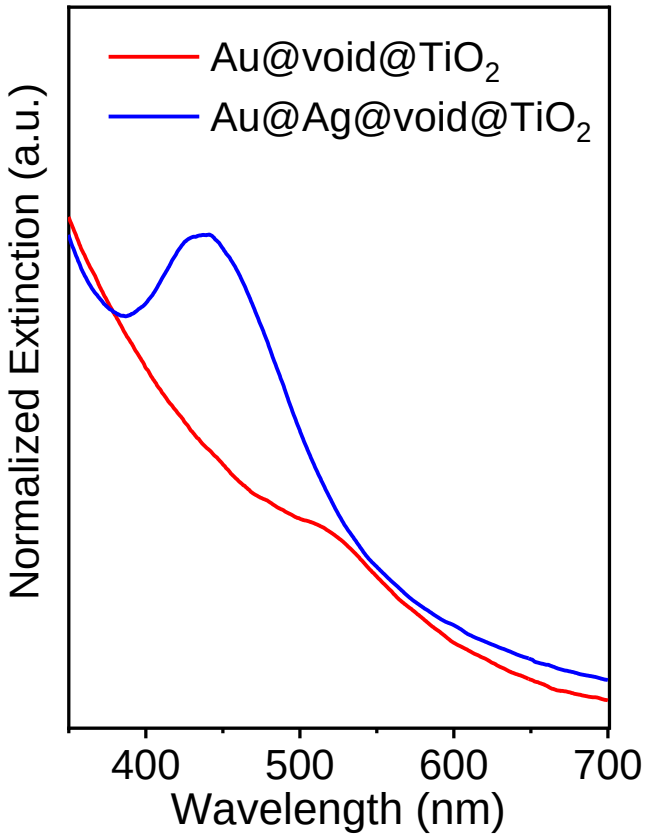

Figure 3.4 UV-vis normalized extinction spectra of Au@void@TiO_2, and Au@Ag@void@TiO_2 yolk-shell NPs.

.

3.3.3 Confined-growth of Ag in the Au@void@TiO_2 nanostructure

The confined growth of Ag on Au within the confined space of Au@void@TiO_2 NPs follows a reported procedure.[24] The Ag growth solution includes $AgNO_3$ as Ag precursor, acetonitrile, ascorbic acid, PVP, and H_2O. Due to the porous structure of TiO_2 shells, the growth solution can penetrate the confined space to grow on the Au surface. The lattice-match between Au and Ag crystals allows the preferential deposition of Ag on Au NPs.[24,25] Controlling the overall size of Ag growth is governed by adjusting the Ag precursor amount during the synthesis. As seen in the TEM images in Figure 3.5a, b, and c, three different overall sizes of Au@Ag were grown by varying the added amount of Ag precursor. A systematic study consists of adding a known amount of Ag precursor, and measuring the produced overall size of Au@Ag core-shell structure was conducted to obtain a controllable growth synthesis of Ag, as shown in Figure 3.5b and c. The size of AuNP was fixed as 20 nm in all experiments. A consistent increase of the plasmonic peak intensity was noticed with each increment of Au@Ag core-shell NPs overall size until the peak starts broadening after reaching 65 nm size (Figure 3.5b). These results are consistent with the growth behavior of Ag on Au as core-shell NPs.[25] A linear correlation of Ag precursor amount vs. the average Ag shell thickness (nm) was obtained for the Au@Ag@void@TiO_2 nanostructure, indicating the excellent controllability of Ag thickness in this confined growth method.

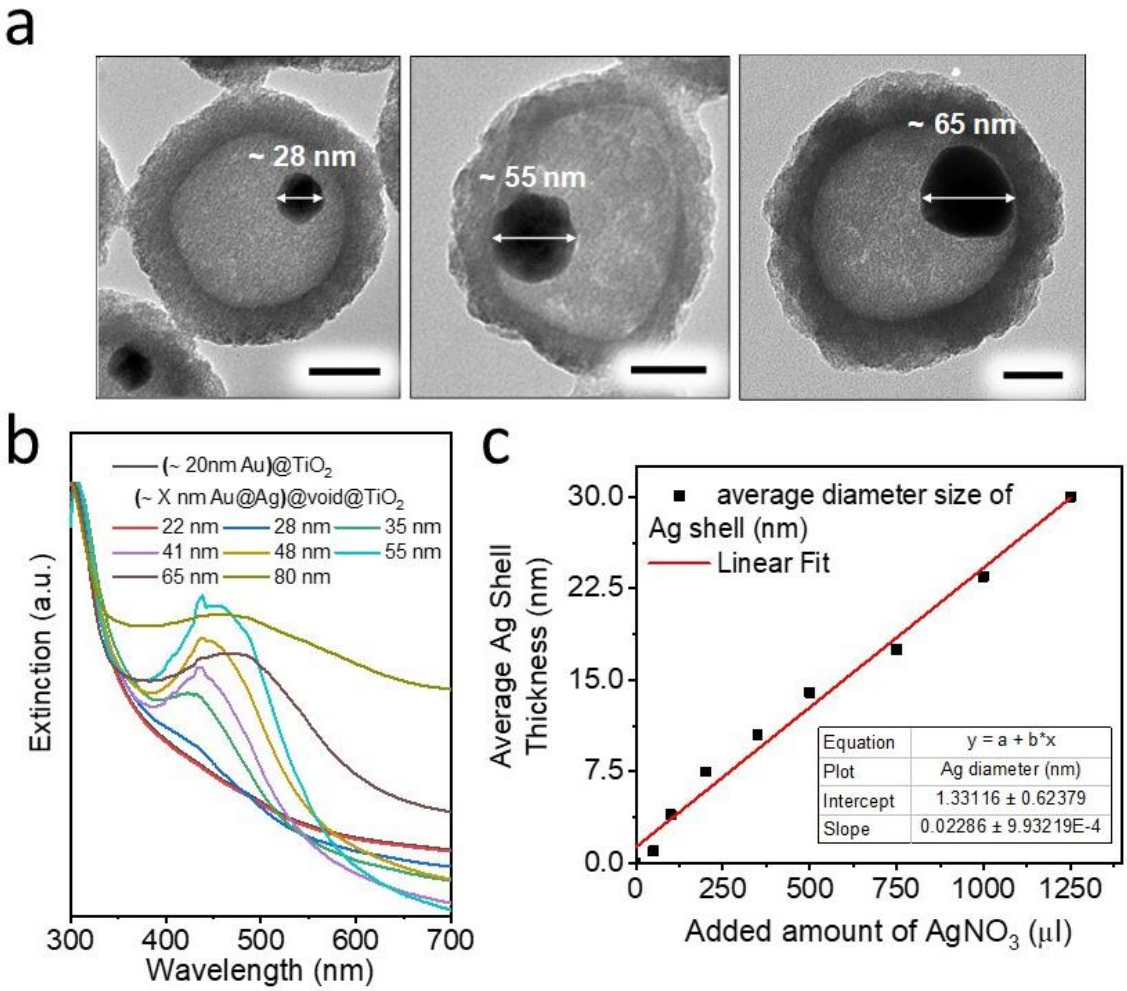

Figure 3.5 (a) Representative TEM images of Au@Ag thickness with 28, 55, and 65 nm. (b) UV-vis extinction spectra of the growth of different Au@Ag shell thickness through controlling the added amount of $AgNO_3$ precursor in the confined space of Au@void@TiO_2. (c) Correlation relation between the added amount of Ag precursor and the average Ag shell thickness in Au@Ag@void@TiO_2 NPs growth synthesis. Scale bar 50 nm.

3.3.4 Development of the colorimetric pressure sensor

The fabrication of the colorimetric pressure sensor involves the spray coating of the nanostructured materials on a PET transparent substrate followed by its covering with another PET substrate to form a sandwiched film. The function of the second substrate is to protect the coated layer of Au@Ag@void@TiO_2 from dispatching and to enhance the stability of the colorimetric pressure sensor film (as it will be demonstrated later). The performance of the film was examined, as shown in Figure 3.6a. An endured pressure was applied using an object placed on top of the fabricated film. Based on the colorimetric pressure sensing mechanism, the color under the pressed area should change immediately after removing the object (Figure 3.6a).

Various nanostructures were tested first to examine their color-change contrast and performance. Au(20 nm)@void@TiO_2 did not show any color-change after applying mechanical pressure, as seen in the film image (Figure 3.6b), which is attributed to the weak plasmonic property of small AuNPs (20 nm), where their plasmonic peak is impeded within the TiO_2 extinction (Figure 3.4). However, an apparent color-change was noticed in every pressed area when Ag was gradually grown on Au@void@TiO_2 (Figure 3.6b). The color-change was also consistent with the intensity enhancement and red-shifting of the plasmonic peak (Figure 3.6c). These results are indicative of the proposed improvement of the sensor performance by growing Ag on Au. The blue-shifting of the initial plasmonic peak of Au@void@TiO_2 helps in obtaining higher color-change contrast by creating a yellowish background of the pre-pressed film (rather than the red color of Au@void@TiO_2). The pressed area will endow a red-shift of the

Au@Ag@void@TiO_2 plasmonic peak to the 500-550 nm range, displaying an orangish/reddish color. This color-change from yellowish to orangish/reddish observes better color-contrast than changing from reddish to pinkish color (Figure 3.6b). Additionally, the increase of the plasmonic peak intensity due to the more apparent plasmonic properties of Ag displays brighter color-change in the Au@Ag@void@TiO_2 films.

The Au@Ag@void@TiO_2 films with 35 and 42 nm overall size of Au@Ag have shown obvious color-change in the impacted area with an increase in their corresponding plasmonic peaks' intensity (Figure 3.6b and c). The contrast of the color-change was significantly improved with overall sizes of 55 and 65 nm Au@Ag. The increase of the plasmonic peak intensity is directly proportional to the increase in the overall size of Au@Ag (Figure 3.6c). When the overall size of Au@Ag reaches above 80 nm, the color-change becomes darker (dark red), which leads to poorer color-contrast, attributed to the scattering effect of a larger Au@Ag core-shell structure above 70 nm, exemplified from the broadening of the plasmonic peak of (80 nm Au@Ag)@void@TiO_2 film (Figure 3.6c).[25] Based on the above results, the (55 nm Au@Ag)@void@TiO_2 film has shown the optimum performance and color-contrast comparing to other films; hence it will be used as a prototype for the further investigations in this study.

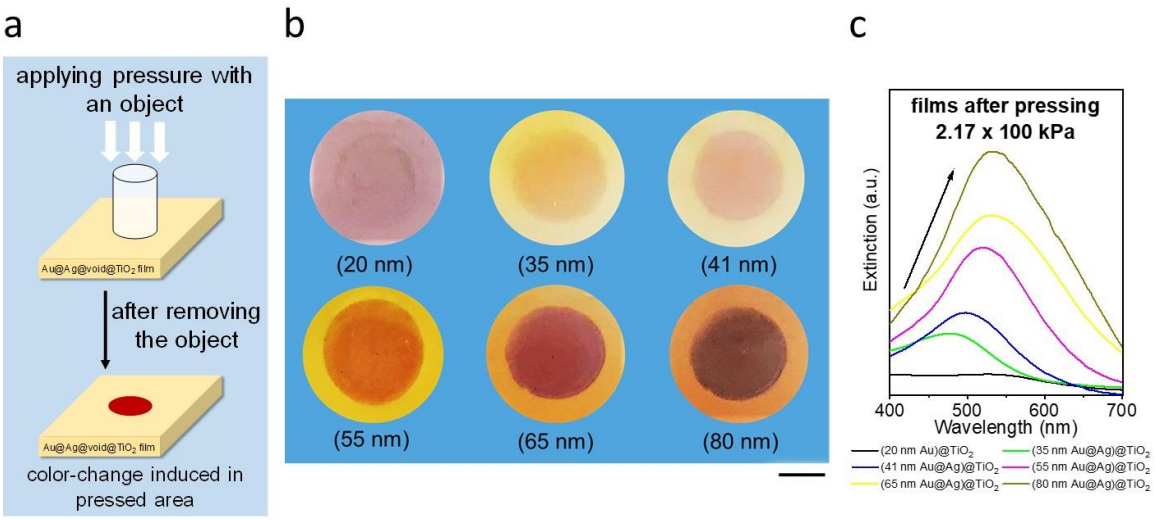

Figure 3.6 (a) Schematic representation of the color-change mechanism based on applying static pressure with an object on Au@Ag@void@TiO_2 film. (b) Color-changes of different Au@Ag(thickness)@void@TiO_2 after inducing static pressure. Scale bar 5 mm. (c) UV-vis spectra of Au@Ag@void@TiO_2 film with different thicknesses of Au@Ag after applying 2.17 x100 kPa of static pressure.

3.3.5 Mechanism of the colorimetric pressure sensing

To confirm that the colorimetric pressure sensing mechanism of Au@Ag@void@TiO_2 film is based on the deformation of TiO_2 and the embodying the plasmonic Au@Ag NPs within the TiO_2 material, systematic simulated and experimental analysis were conducted as seen in Figure 3.7-3.10. The TEM images in Figure 3.7a and b show the Au@Ag@void@TiO_2 nanostructures before and after TiO_2 shell deformation, respectively. Figure 3.7b confirms that TiO_2 porous materials completely cover the plasmonic Au@Ag NPs after their deformation. The SEM images in Figure 3.8a-d show lower magnification images of the nanostructures before and after applying an impact force. Figure 3.8a and b represents a side-view of Au@Ag@void@TiO_2 nanostructures before and after TiO_2 deformation, respectively. The deformation of the spherical shape of Au@Ag@void@TiO_2 nanostructures is apparent in Figure 3.8b, where the particles transformed into one layered surface after removing the pressed object. The same is observed from the SEM top-view of Au@Ag@void@TiO_2 nanoparticles in Figure 3.8c and d, before and after their deformation, respectively.

The finite-element analysis was used to simulate the optical properties of Au@Ag@void@TiO_2 nanostructures, before and after their deformation. The overall size of Au@Ag NPs and TiO_2 thickness was fixed as 60 and 30 nm, respectively. The Au@Ag@TiO_2 nanostructure was used to simulate the materials after applying the mechanical force, where the TiO_2 are entirely covering the core-shell NPs. The distribution of the electric field intensity in the proximity of the (I) Au@Ag@void@TiO_2 and (II) Au@Ag@TiO_2 nanostructures are represented in Figure 3.9a. The simulated and

experimental UV-vis absorption of the nanostructured materials (I) before and (II) after applying a mechanical force are shown in Figure 3.9b. The plasmonic peak positions of the simulated and experimental UV-vis absorption of the nanostructured materials (I) before and (II) after the deformation of the particles are well-matched (Figure 3.9b). These findings agree with the proposed mechanism of changing the environment surrounding the plasmonic nanoparticles in Au@Ag@void@TiO_2 from air to TiO_2 after the outer shell's deformation.

Another mechanism based on the shape-change of plasmonic nanoparticles from spherical to plates under a mechanical force could be postulated for the color-change of Au@Ag@void@TiO_2-based stress sensor. The mechanical deformation of silver nanoparticles has produced a red-shift of the Ag plasmonic peak from 470 to 650 nm owing to their transformation into nanoplate structures.[26], the average particles size of Au@Ag core-shell NPs in the Au@Ag@void@TiO_2 nanostructures were measured before and after applying mechanical stress (Figure 3.10a) to examine the above hypothesis. As shown in Figure 3.10b, the average particle size of Au@Ag was ~53.8 and 54.2 nm before and after applying mechanical pressure, respectively. There was no noticeable change (i.e., deformation) of Au@Ag NPs shape before and after the breakage of TiO_2 shells (Figure 3.10c). Therefore, we can conclude than the main reason behind the color-change of Au@Ag@void@TiO_2-based stress sensor is the change of the refractive index (i.e., environment) surrounding the plasmonic Au@Ag NPs after TiO_2 shells deformation.

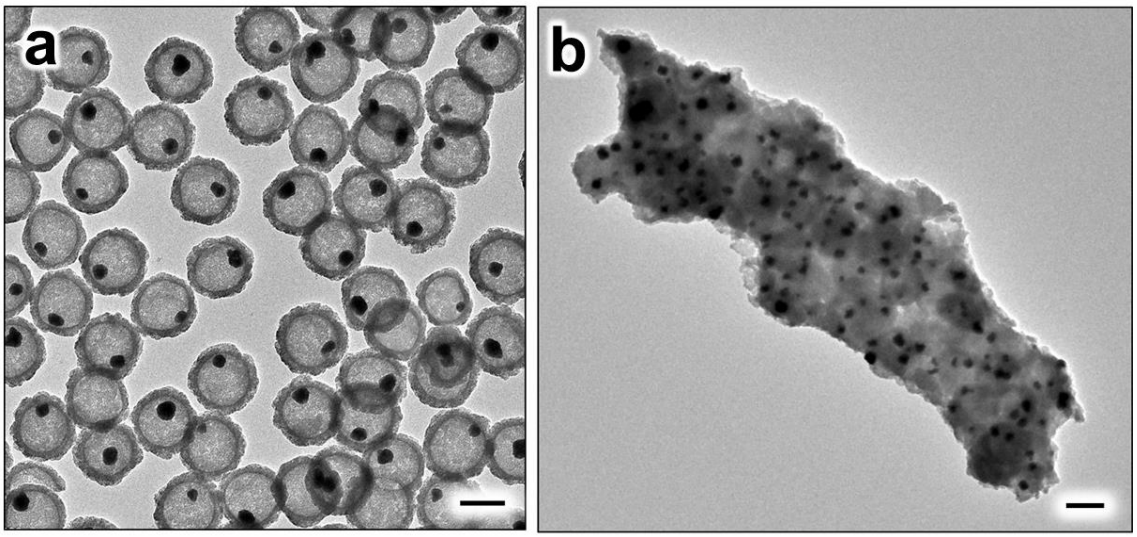

Figure 3.7 TEM images of Au@Ag@void@TiO_2 nanostructures (a) before deformation and (b) after deformation caused by applying an impact force. Scale bar 50 nm.

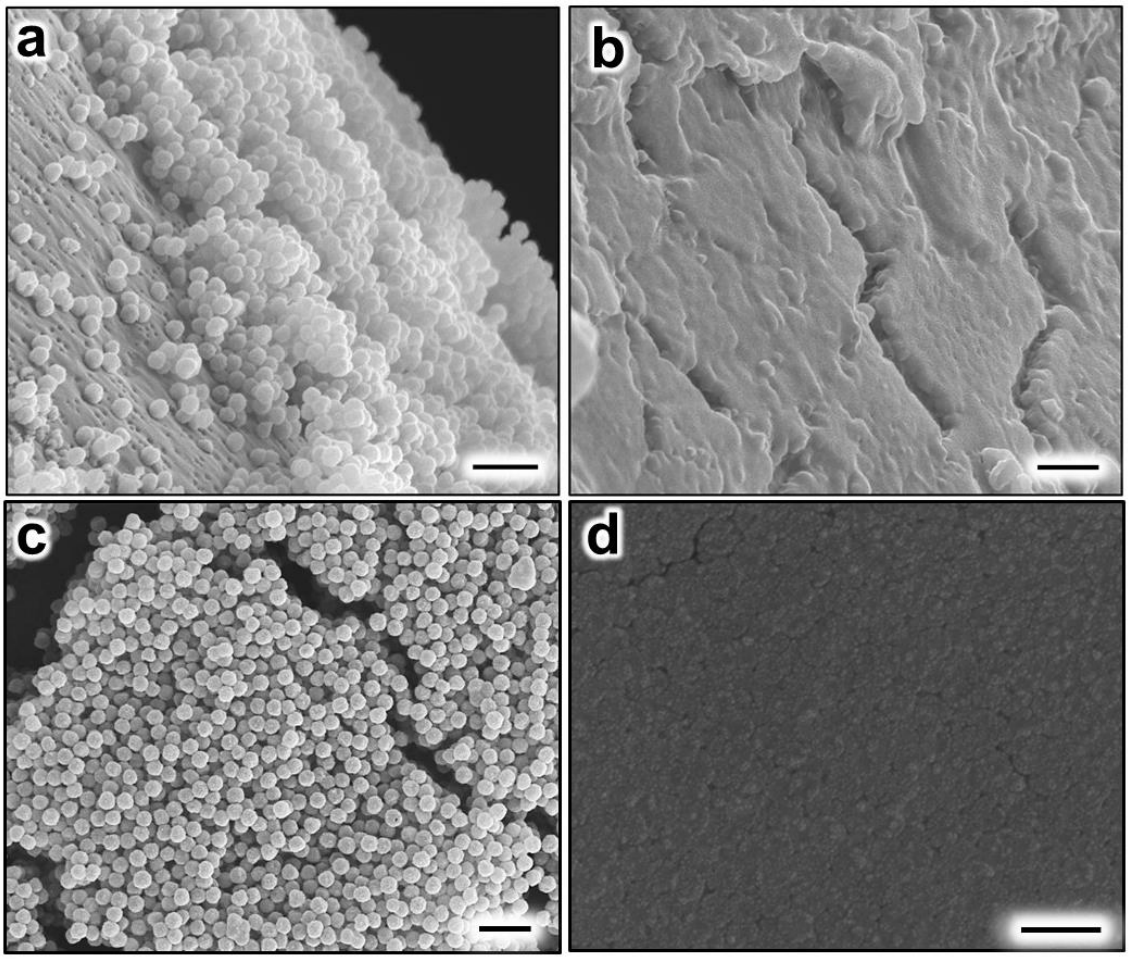

Figure 3.8 SEM images of Au@Ag@void@TiO_2 nanoparticles (a) before deformation and (b) after deformation caused by applying an impact force. SEM images of top-view of Au@Ag@void@TiO_2 nanoparticles (a) before deformation and (b) after deformation caused by applying an impact force Scale bar 1000 nm.

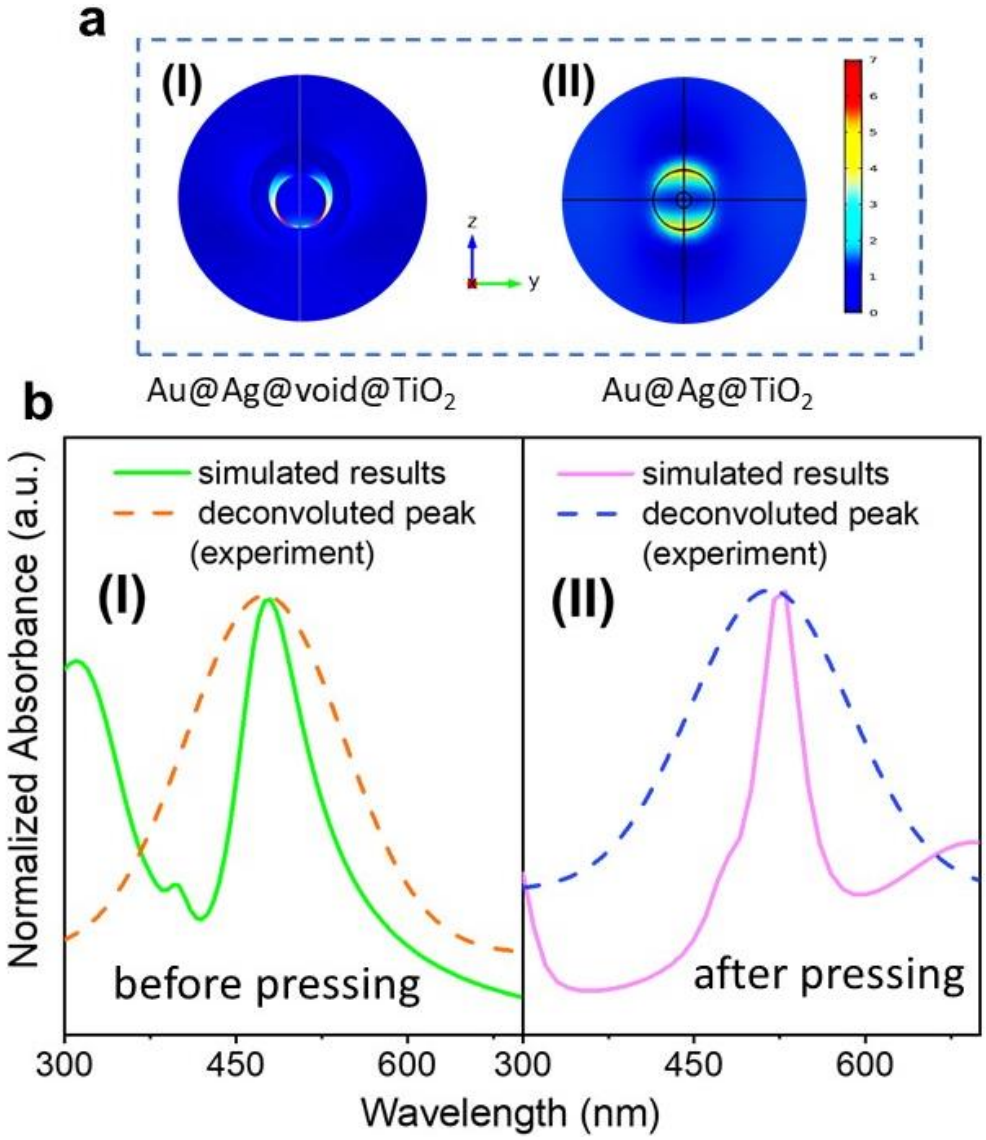

Figure 3.9 (a) Distribution of the electric field intensity in the proximity of Au@Ag@void@TiO_2 yolk-shell nanostructure representing the particles before applying pressure (I) and the Au@Ag@TiO_2 core-shell nanostructure representing the particles after applying pressure (II). (b) Comparison of the simulated and experiments UV-vis absorptions of the nanoparticles before (I) and after (II) applying pressure.

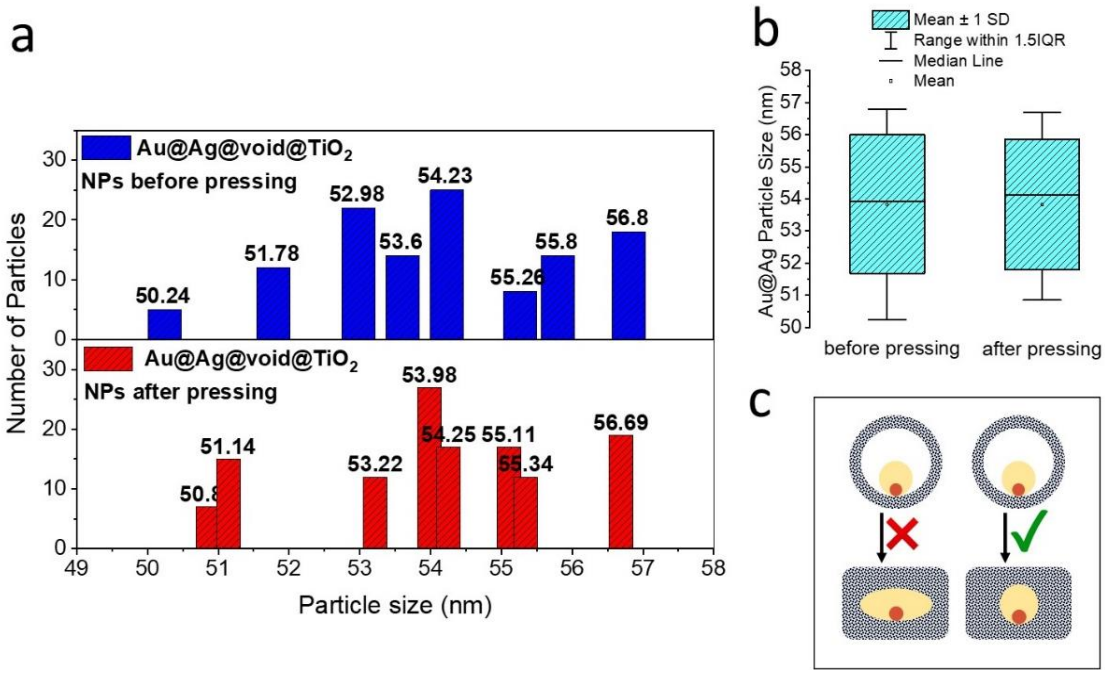

Figure 3.10 (a) Particle size distribution vs. the number of particles of Au@Ag core-shell NPs within (55 nm Au@Ag)@void@TiO_2 yolk-shell nanostructures before and after their pressing. (b) Calculated Au@Ag core-shell size in (55nm Au@Ag)@void@TiO_2 nanostructures before (I) and after (II) applying pressure. (C) Schematic representation of the response of Au@Ag NPs during the yolk-shell deformation.

3.3.6 Performance and stability testing

The performance of the colorimetric pressure sensor was measured while applying a static and dynamic force, as seen in Figures 3.11 and 3.12, respectively. By applying a continuous pressure for a fixed period, the (55nm Au@Ag)@void@TiO_2 film showed a colorimetric response directly proportional to the increase of the static pressure (Figure 3.11a). The UV-vis spectra of the film also demonstrated similar observations, where the plasmonic peak of the film initially positioned at 475 nm endured a red-shift to 510 nm when a static pressure of 2.17 x100 kPa was applied (Figure 3.11b). The plasmonic peak intensity gradually increased by the continuous increase of static pressure from 2.17 until 8.66 x100 kPa. The red-shift of the SPR position was monitored and plotted against the pressed pressure, as seen in Figure 3.11c. The red-shift of the SPR position reached a plateau after applying a static pressure of 6.50 x100 kPa.

Schematic representation of the set-up for testing the colorimetric film response to an impact force is shown in Figure 3.12a. A weighted object in a cylindrical shape (1 Kg) is dropped from a measured height on top of the film. The impact force is measured based on the weight and height used. The (55nm Au@Ag)@void@TiO_2 film illustrated an apparent color-change in response to the dropping object, as seen in Figure 3.12b. The UV-vis extinction (Figure 3.12c) of the (55nm Au@Ag)@void@TiO_2 film was measured in correlation with the increase of the impact force (i.e., fixed object weight with increasing the dropping height). The SPR positions of the film were also recorded against the object dropping heights (Figure 3.12d). In the low impact force range between 0 and 10 cm height, the SPR position did not show a significant red-shift. However, a dramatic

response represented in higher SPR position shifts was noticed between 10 and 20 cm height. A plateau of the colorimetric film response was noticed after 20 cm height. These results indicate that initially, at 0 to 5 cm object heights, the TiO_2 shells do not deform because their mechanical strengths can withhold the induced forces. The rapid SPR positions shift between 5 and 20 cm heights demonstrates the incremental breakages of TiO_2 shells with the higher forces, up to the destruction of the shells after 20 cm height (i.e., reaching a plateau of SPR peak shift).

Additionally, the stability of the colorimetric pressure sensor film was investigated by analyzing the variation of the film UV-vis extinction in 30 days. The film was analyzed in a sandwiched structure of two PET substrates (Figure 3.13a) and without a top PET substrate (Figure 3.13b). The UV-vis extinction profile of the sandwiched (55nm Au@Ag)@void@TiO_2 film did not show significant change after 30 days of measuring (Figure 3.13a), unlike the second structure, which endured a substantial change in its extinction profile (Figure 3.13b). These results prove the importance of the sandwiched structure in stabilizing the colorimetric pressure sensor film. The UV-vis extinction profile change of the film shown in Figure 3.13b is presumably attributed to the oxidation of Ag surfaces by O_2 molecules. The sandwiched PET substrates covering the coated layer of (55nm Au@Ag)@void@TiO_2, reduce the penetration of O_2 into the nanostructured materials and hence prevent the oxidation of Ag NPs. The sandwiched film stability was also tested by investigating its color-change response to an impact force after keeping the film in ambient conditions for 30 days. The performance of the film in the first day and after one month is shown in Figure 3.13c. No significant changes were

noticed in the film response or contrast after keeping the film in ambient conditions for one month, which also indicates the excellent stability of the sandwiched structured film.

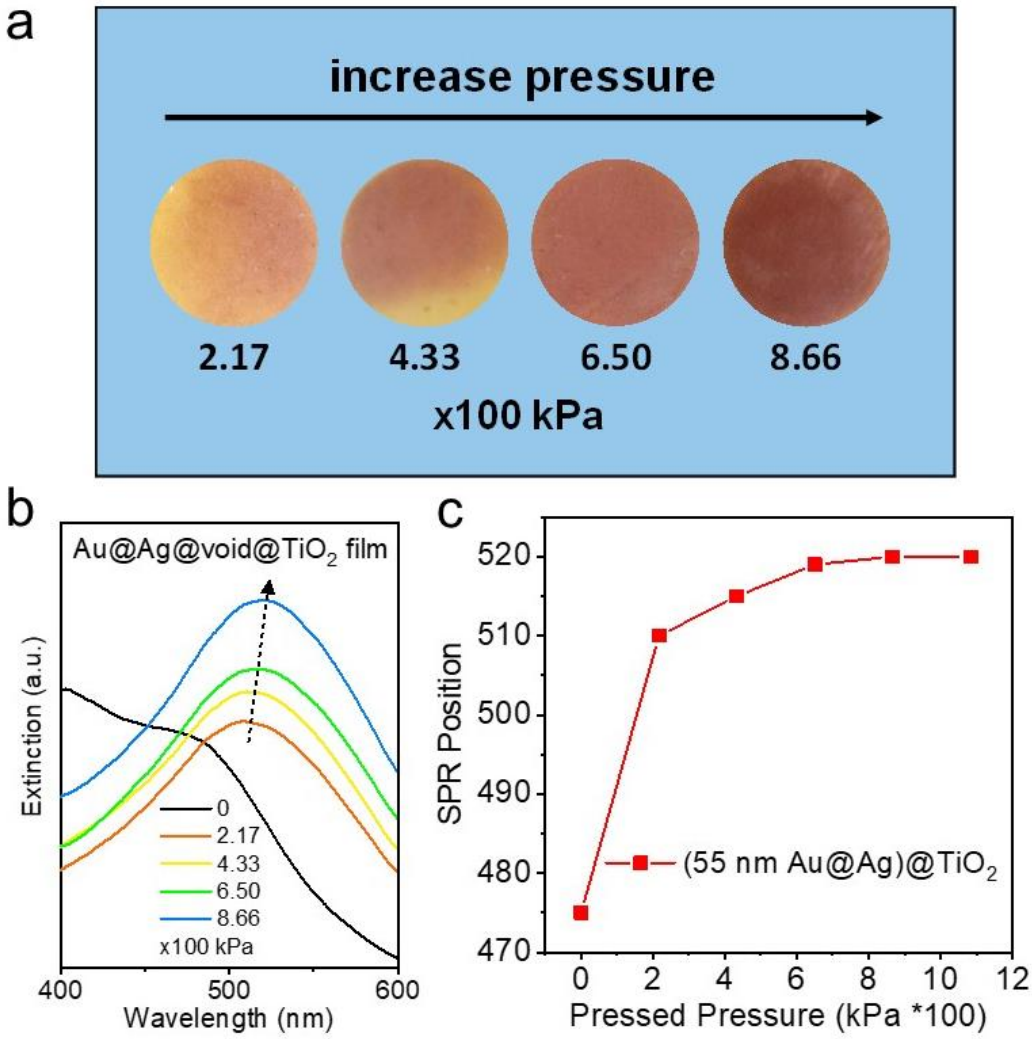

Figure 3.11 (a) Colorimetric response of (55nm Au@Ag)@void@TiO_2 film with increasing the applied static pressure. (b) The corresponding UV-vis spectra of (55nm Au@Ag)@void@TiO_2 film with increasing the applied static pressure. (c) The response of SPR positions of (55nm Au@Ag)@void@TiO_2 film vs. the applied static pressure.

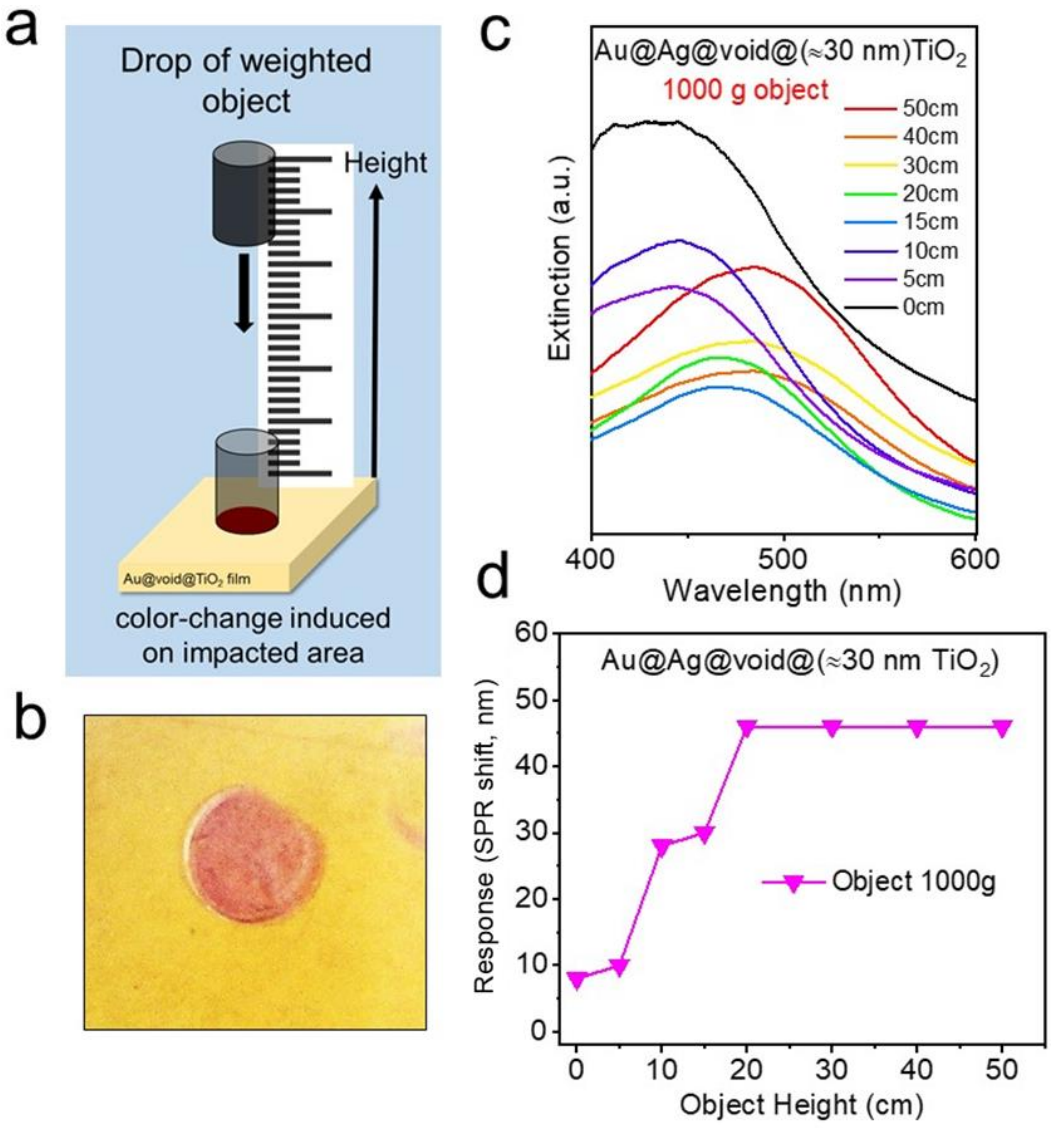

Figure 3.12 (a) Schematic representation of the impact force testing setup. (b) UV-vis extinction spectra of the evolution of (55nm Au@Ag)@void@TiO_2 film with 30 nm thickness of TiO_2 shell under dropping height of an object with 1000 g weight. (c) Image of (55nm Au@Ag)@void@TiO_2 film with 30 nm thickness of TiO_2 after conducting the impact force test. (d) The correlation between the object height and the response (SPR position) of the (55nm Au@Ag)@void@TiO_2 film with 30 nm thickness of TiO_2.

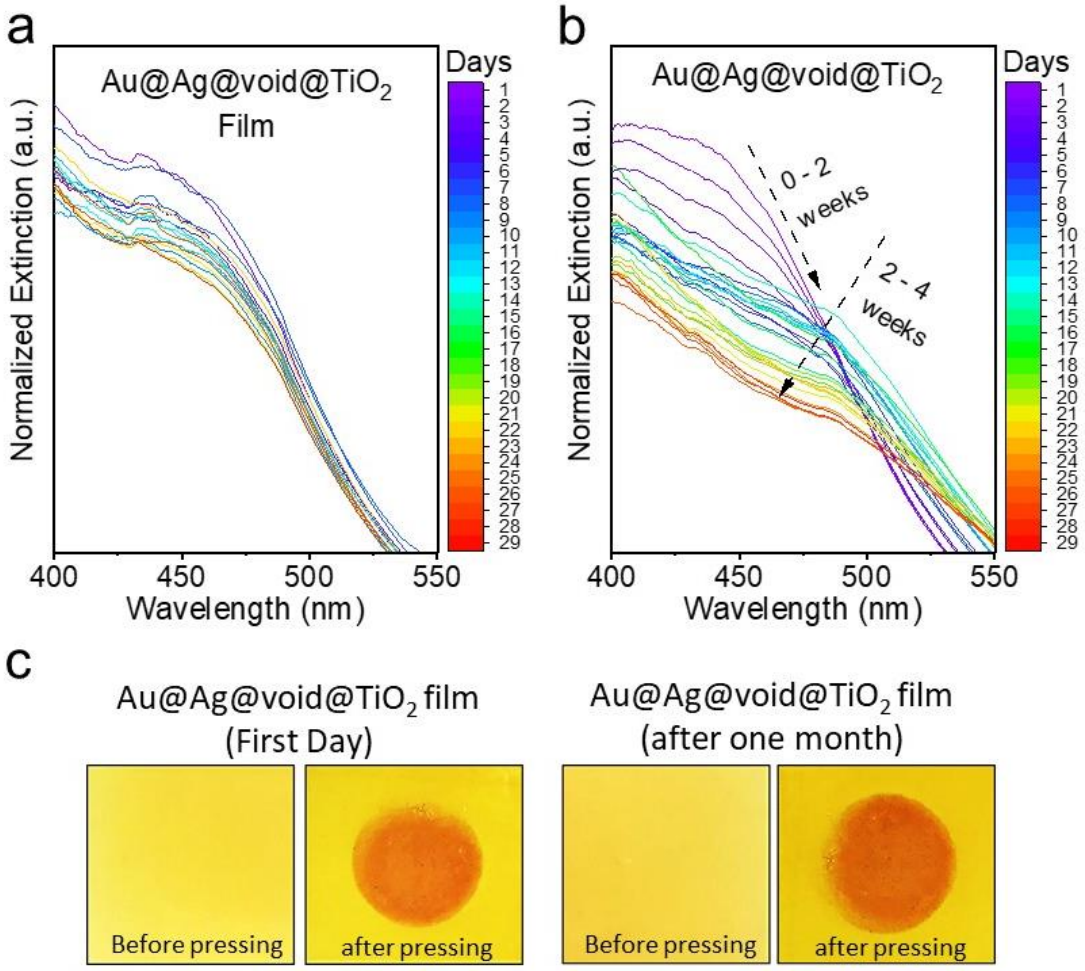

Figure 3.13 (a) Stability measurements of (55nm Au@Ag)@void@TiO_2 sandwiched between two plastic substrates via measuring the evolution of UV-vis spectra of the film for one month. (b) Stability measurements of (55nm Au@Ag)@void@TiO_2 coated on one side of a plastic substrate via measuring the evolution of UV-vis spectra of the film for one month. (c) Images of (55nm Au@Ag)@void@TiO_2 film sandwiched between two plastic substrates before and after applying static pressure in day one and after leaving the film for one month in ambient conditions.

3.3.7 Applications

Different TiO_2 thickness could be used to vary the mechanical strength of the nanostructured materials. Molecular dynamics (MD) simulations of hollow nanospheres proved that the overall mechanical strength of the NPs could be enhanced by increasing the thickness of their outer shells.[27] Therefore, different thicknesses of TiO_2 in Au@Ag@void@TiO_2 NPs are expected to obtain different pressure thresholds. In this way, an impact test paper similar to a pH test paper could be fabricated, where each strip on the paper represents Au@Ag@void@TiO_2 film with different TiO_2 thickness that displays a different measure of impact forces. Figure 3.14 demonstrates the TEM images and the correlation between objects heights and the SPR shifts of (55nm Au@Ag)@void@TiO_2 film with (a) 30, (b) 48, and (c) 73 nm thickness of TiO_2 shell. (55 nm Au@Ag)@void@TiO_2 film with 30 nm TiO_2 thickness reached a maximum threshold with an object weighted 1000g and dropped from 20 cm height, while the 73 nm TiO_2 thickness did not reach the maximum threshold with even 1000g object and 50 cm dropping height. These results demonstrate that a pressure test paper could be developed with three strips representing the Au@Ag)@void@TiO_2 film with 30, 48, and 73 nm TiO_2 thickness, where the color-change after an impact on each strip displays low, high, and severe impact level, respectively.

Another application of the technique includes mechanical force printing. Figure 3.15 shows the images of instantaneous mechanical printing on (55nm Au@Ag)@void@TiO_2 film with 30 nm TiO_2 thickness consists of stamping a stainless-

steel pattern on the film using a hammer. The produced images illustrate the instantaneous printing of the technique with a high resolution of writing.

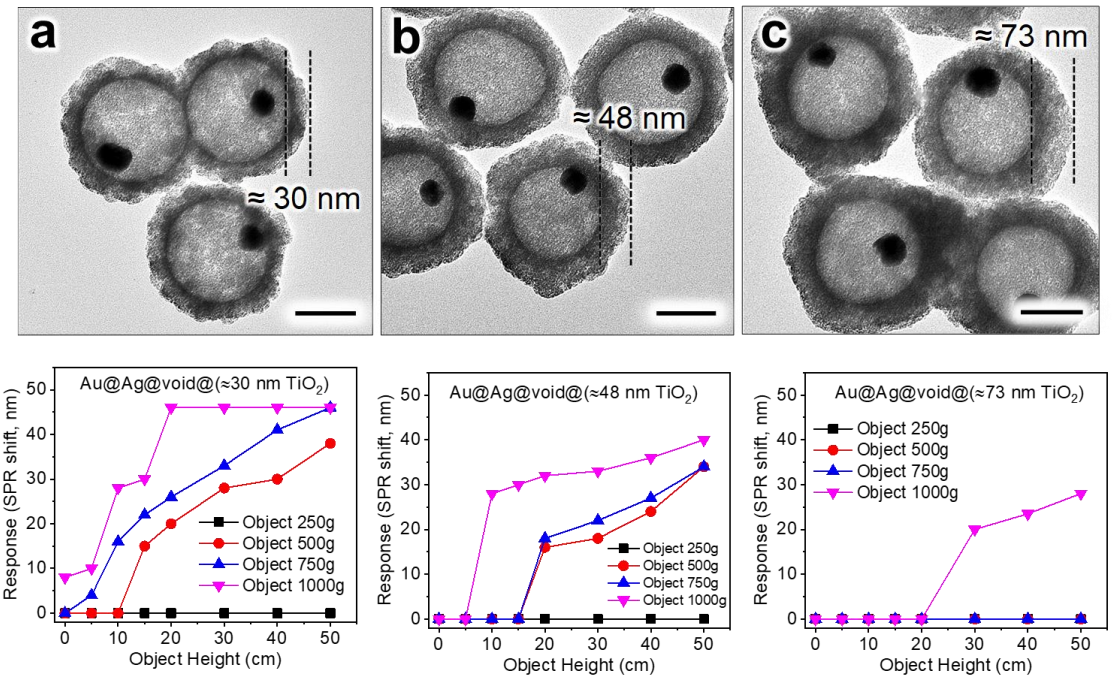

Figure 3.14 TEM images and the correlation between the objects' heights and SPR shifts of (55nm Au@Ag)@void@TiO_2 film with (a) 30, (b) 48, and (c) 73 nm thickness of TiO_2 shell.

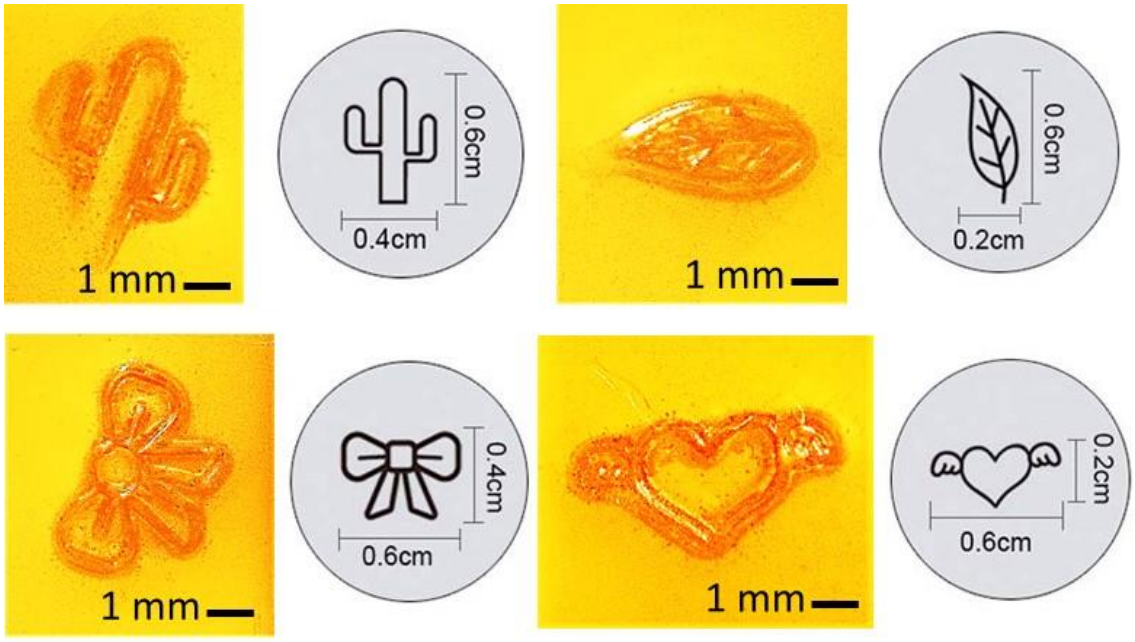

Figure 3.15 Representative images of the mechanical printing on (55nm Au@Ag)@void@TiO_2 film with 30 nm thickness of TiO_2 shell consists of stamping a stainless-steel pattern on the film using a hammer.

3.4 Conclusions

A colorimetric pressure sensor based on the deformation of Au@Ag@void@TiO_2 nanostructured particles was developed. A color change from yellow to dark orange/red was induced on the Au@Ag@void@TiO_2 film after applying a mechanical force. The color-change mechanism is based on the deformation of the TiO_2 shell after encountering mechanical stress, causing the refractive index around the plasmonic nanoparticles to change from air to TiO_2. The colorimetric pressure sensor applies to static and dynamic force. Different thickness of TiO_2 showed different thresholds for the colorimetric pressure response. The developed Au@Ag@void@TiO_2 colorimetric sensor could be used for a wide range of applications, including instantaneous impact detectors in sports helmets, bicycle helmets, sports mouthguards, and automobile crash dummies to indicate the occurrence and force of an impact or to monitor the impact of fragile, expensive, specialized electronics and computers shipments. The instantaneous stress detection, excellent color-contrast, flexibility, and stability against environmental changes are the main advantages of the new colorimetric stress sensor.

3.5 References

[1] V. Maheshwari, R. F. Saraf, *Science (80-.).* **2006**, *312*, 1501 LP – 1504.

[2] S. C. B. Mannsfeld, B. C.-K. Tee, R. M. Stoltenberg, C. V. H.-H. Chen, S. Barman, B. V. O. Muir, A. N. Sokolov, C. Reese, Z. Bao, *Nat. Mater.* **2010**, *9*, 859–864.

[3] S. Lee, A. Reuveny, J. Reeder, S. Lee, H. Jin, Q. Liu, T. Yokota, T. Sekitani, T. Isoyama, Y. Abe, et al., *Nat. Nanotechnol.* **2016**, *11*, 472–478.

[4] S. Dong, L. Shen, H. Li, G. Pang, H. Dou, X. Zhang, *Adv. Funct. Mater.* **2016**, *26*, 3703–3710.

[5] Y. Zang, F. Zhang, D. Huang, X. Gao, C. Di, D. Zhu, *Nat. Commun.* **2015**, *6*, 6269.

[6] T. Yamada, Y. Hayamizu, Y. Yamamoto, Y. Yomogida, A. Izadi-Najafabadi, D. N. Futaba, K. Hata, *Nat. Nanotechnol.* **2011**, *6*, 296–301.

[7] D. A. Davis, A. Hamilton, J. Yang, L. D. Cremar, D. Van Gough, S. L. Potisek, M. T. Ong, P. V Braun, T. J. Martínez, S. R. White, et al., *Nature* **2009**, *459*, 68–72.

[8] M. Kaltenbrunner, T. Sekitani, J. Reeder, T. Yokota, K. Kuribara, T. Tokuhara, M. Drack, R. Schwödiauer, I. Graz, S. Bauer-Gogonea, et al., *Nature* **2013**, *499*, 458–463.

[9] Y. S. Rim, S.-H. Bae, H. Chen, N. De Marco, Y. Yang, *Adv. Mater.* **2016**, *28*, 4415–4440.

[10] S. Takamatsu, T. Lonjaret, E. Ismailova, A. Masuda, T. Itoh, G. G. Malliaras, *Adv. Mater.* **2016**, *28*, 4485–4488.

[11] D. Kang, P. V Pikhitsa, Y. W. Choi, C. Lee, S. S. Shin, L. Piao, B. Park, K.-Y. Suh, T. Kim, M. Choi, *Nature* **2014**, *516*, 222–226.

[12] D. J. Lipomi, M. Vosgueritchian, B. C.-K. Tee, S. L. Hellstrom, J. A. Lee, C. H. Fox, Z. Bao, *Nat. Nanotechnol.* **2011**, *6*, 788–792.

[13] S. Gong, W. Schwalb, Y. Wang, Y. Chen, Y. Tang, J. Si, B. Shirinzadeh, W. Cheng, *Nat. Commun.* **2014**, *5*, 3132.

[14] H. Fudouzi, T. Sawada, *Langmuir* **2006**, *22*, 1365–1368.

[15] J. Tong, Y. Wang, J. Mei, J. Wang, A. Qin, J. Z. Sun, B. Z. Tang, *Chem. – A Eur. J.* **2014**, *20*, 4661–4670.

[16] Z. Li, W. Wang, Y. Yin, *Trends Chem.* **2020**, DOI https://doi.org/10.1016/j.trechm.2020.03.008.

[17] X. Han, Y. Liu, Y. Yin, *Nano Lett.* **2014**, *14*, 2466–2470.

[18] L. Fu, Y. Liu, W. Wang, M. Wang, Y. Bai, E. L. Chronister, L. Zhen, Y. Yin, *Nanoscale* **2015**, *7*, 14483–14488.

[19] M. Quan, B. Yang, J. Wang, H. Yu, X. Cao, *ACS Appl. Mater. Interfaces* **2018**, *10*, 4243–4249.

[20] Y. Bai, Structural Engineering of Optical Nanomaterials, University of California Riverside, **2017**.

[21] W. Shimizu, S. Nakamura, T. Sato, Y. Murakami, *Langmuir* **2012**, *28*, 12245–12255.

[22] J. B. Joo, R. Dillon, I. Lee, Y. Yin, C. J. Bardeen, F. Zaera, *Proc. Natl. Acad. Sci.* **2014**, *111*, 7942 LP – 7947.

[23] I. Lee, J. B. Joo, Y. Yin, F. Zaera, *Angew. Chemie Int. Ed.* **2011**, *50*, 10208–10211.

[24] C. Gao, Y. Hu, M. Wang, M. Chi, Y. Yin, *J. Am. Chem. Soc.* **2014**, *136*, 7474–7479.

[25] Y. Chen, H. Wu, Z. Li, P. Wang, L. Yang, Y. Fang, *Plasmonics* **2012**, *7*, 509–513.

[26] F. S. Ameer, S. Varahagiri, D. W. Benza, D. R. Willett, Y. Wen, F. Wang, G. Chumanov, J. N. Anker, *J. Phys. Chem. C* **2016**, *120*, 20886–20895.

[27] L. Yang, J. J. Bian, H. Zhang, X. R. Niu, G. F. Wang, *AIP Adv.* **2015**, *5*, 77162.

Chapter 4. Anchoring Magnetic Iron Oxide through Molybdenum Sulfide Transitional Layer: A Universal Magnetizing Method

4.1 Introduction

The ability to magnetize nanostructured materials has expanded their applications into various fields, including drug delivery, biomedical imaging, actuators, smart windows, and display devices.[1–3] Nonmagnetic NPs can be magnetically functionalized by either being coated on a magnetic core (or vice versa) or their surface-attachments with magnetic particles. Metallic, metal oxide, polymeric, and dendrimeric shells can be coated on a magnetic core consists of magnetic materials such as Co, Ni, Mn, Fe, and their alloys and oxides. A strong affinity between the magnetic core and the nonmagnetic materials must exist to induce this coating process, which could be achieved either by performing surface modification of the magnetic core or adding a translational layer that binds both materials.[4–6] For instance, doxorubicin (DOX), a chemotherapy drug, can be attached to FePt@Fe_2O_3-PEG core-shell magnetic NPs for targeted drug-delivery using a magnetic field.[7] Polyethyleneimine was used as a binding layer between Au and iron oxide in the synthesis of Au@PEI-Fe_3O_4 core-shell NPs to develop a nano-heater NPs for hyperthermia applications.[8] Surface attachment of magnetic nanostructures into nonmagnetic materials also follows surface modification of either material, which involves utilizing ligands and polymers such as thiols, amine-functionalized ligands, PEI, and polyacrylic acid for surface functionalization.[4–6]

However, current methods of magnetizing nonmagnetic NPs require multiple steps of coating and surface modifications, which substantially increase the cost and time

of the fabrication process. The utilization of surface ligands could also increase the toxicity of the materials, especially considering their applications in biomedical fields.[9] Additionally, each colloidal coating methods or attachment of magnetic NPs follow different synthetic protocols and reaction conditions. These limitations become substantial for larger particles (micro-scale), where the synthetic procedures and surface modifications are not easily controlled. Therefore, there is a great need for a universal, simple, quick, cost-effective, and robust method of magnetizing nanostructured materials.

Our previous findings revealed that there is a strong adhering between bulk molybdenum sulfide particles and commercial magnetic iron oxide particles by simply mixing both materials in solution.[10] This interaction happens instantaneously, where both particles aggregate into a composite magnetic mixture. We decided to utilize this feature to develop a universal magnetizing method by using molybdenum sulfide as a transitional layer to anchor magnetic NPs onto the nonmagnetic materials. Because SiO_2 coating is the most established, universal, and simple coating method on several nanostructured materials, we developed first a colloidal coating protocol of molybdenum sulfide on SiO_2. This colloidal process is found to be very simple, scalable, rapid. Additionally, it undergoes in ambient conditions and green solvents (i.e., water), without the involvement of harsh chemicals (e.g., reducing agent) or change in pH and temperature, eliminating the possibilities of etching or alteration of structural properties of the nanostructured materials. The attachment of iron oxide magnetic nanoparticles onto the molybdenum sulfide layer occurs instantaneously by simply mixing both nanoparticles in solution without adding any chemicals or changing the reaction

conditions, owing to the strong interaction between iron oxide and molybdenum sulfide. Various structures and forms of iron oxide (e.g., nanocubes, FeO, etc.) could also be attached using the same technique. The application of the magnetizing method was illustrated by magnetizing Au microplate to fabricate a magnetically-responsive colloidal micromirror. This method reduced the required time of magnetizing Au microplates from approximately 24 h of typical modifications process to less than 15 minutes.

4.2 Materials and methods

4.2.1 Materials

$NH_3 \cdot H_2O$ (28wt%), ammonium tetrathiomolybdate $(NH_4)_2MoS_4$, tetraethylorthosilicate (TEOS, 98%), poly(diallyldimethylammonium) chloride (PDDA, MW = 400,000-500,000, 20 wt% in H_2O), oleic acid, iron pentacarbonyl, and tetramethylammonium hydroxide (TMAH, 25 wt% in H_2O), $HAuCl_4$ trihydrate, (3-aminopropyl)triethoxysilane (APTES), and hydrochloric acid (conc.) were purchased from Sigma-Aldrich. Methanol, denatured ethanol, isopropanol, cyclohexane, and acetone were purchased from Fisher. Salicylic acid was purchased from MP Biomedicals, and agarose was purchased from Biorad. Commercial Fe_3O_4 nanoparticles powder (average particle size: ~20-30 nm) was purchased from US Research Nanomaterials, Inc. All chemicals were directly used without further purification. Solutions were prepared with water (18.2 MΩ/cm) produced from Milli-Q system (Millipore).

4.2.2 Synthesis of SiO_2 spheres

23 ml of ethanol, 3.1 ml of H_2O, 0.86 ml of TEOS, and 0.65 ml of $NH_3 \cdot H_2O$(28wt%) were stirred at room temperature for 4 h. The resulting SiO_2

nanoparticles were collected by centrifugation, washed with ethanol and water, and dispersed in 5 ml of ethanol.

4.2.3 APTES functionalization of SiO_2 spheres

5 ml of SiO_2 in ethanol was mixed with 30 ml EtOH in room temperature in a three-neck round-bottom flask. 2 ml of APTES was added to the mixture. Then it left under stirring at 80 ^oC for 3 h. Finally, the mixture was left overnight in room temperature under stirring. The resulting APTES-SiO_2 was collected by centrifugation, washed three times with ethanol and two times with water, and dispersed in 10 ml H_2O.

4.2.4 Synthesis of APTES-SiO_2@a-MoS_x

The synthesis of a-MoS_x followed the same reported acidification process of $(NH_4)_2MoS_2$ precursor.[11–13] Initially, 10 mg of $(NH_4)_2MoS_2$ was dissolved first in 3 ml H_2O under sonication. Then, 2 ml of APTES-SiO_2 was added to the solution. The mixture was sonicated and agitated under sonication for 2 min. 2 ml of (0.05 M) HCl was then added while keeping the reaction under sonication. The mixture was agitated for another 5 min in the sonicator. The product was collected by centrifugation, washed two times with H_2O and EtOH, and finally dispersed in 5 ml EtOH.

4.2.5 Synthesis of a-MoS_x nanoparticles

10 mg of $(NH_4)_2MoS_2$ was dissolved first in 5 ml H_2O under sonication. The mixture was sonicated and agitated under sonication for 2 min. 2 ml of (0.05 M) HCl was then added while keeping the reaction under sonication. The mixture was agitated for another 5 min in the sonicator. The product was collected by centrifugation, washed two times with H_2O and EtOH, and finally dispersed in 5 ml EtOH.

4.2.6 Synthesis of Au microplates

Au microplates were synthesized using an acid-mediated reduction method reported in the literature.[14] Typically, 70.2 ml of H_2O, PDDA (1.8 ml, diluted to 2 wt % in H_2O), and 8 ml of salicylic acid (18.1 mM) were mixed and heated to 80 °C in a three-neck round-bottom flask under stirring. 3.2 ml of $HAuCl_4$ (48.6 mM) was added to the mixture, after which the solution was stirred for 10 min to yield a turbid golden solution. The product was collected by centrifugation, washed two times with H_2O, and dispersed in 20 ml H_2O. The resulting microplates have an average diameter of 7.28 ± 2.61 μm and a thickness of ~ 75 nm.[14]

4.2.7 Coating a-MoS_x on Au microplates

2 ml of Au microplates were mixed with 8 ml H_2O and 10 μl HCl under stirring at room temperature. Then, 200 μl of stock solution of $(NH_4)_2MoS_2$ (3 mg/ml in H_2O) was added under stirring to the mixture to start the coating process. Continuous addition of 200 μl per minute of $(NH_4)_2MoS_2$ stock solution was performed for 10 min (total 2 ml) until the mixture turned to black color. The reaction was allowed to continue for 15 min. The product was collected by centrifugation, washed two times with H_2O, and dispersed in 20 ml H_2O.

4.2.8 Magnetic functionalization of Au microplates

1:1 v/v ratio of Au@a-MoSx microplate's solution (20 ml) was mixed with Fe_3O_4 solution (1 mg/ml) under sonication for 5 min. The solution was vigorously shaken during sonication. The product was collected by magnetic separation, redisperse again in

H_2O, after which this process was repeated several times to remove non-magnetic Au microplates. The collected microplates were finally dispersed in 4 ml H_2O.

4.2.9 Fabrication of magnetically-responsive micromirror

The microplates solution was mixed first with 5 µl agarose (0.5 wt%, 70 ^oC), which was used to reduce precipitation and aggregation of the microplates. This mixture was injected into a plastic cuvette. Microplates were rotated using a ~ 2900 G rare earth magnet. Optical images and videos were recorded using a phone camera.

4.2.10 Characterizations

Transmission electron microscopy(TEM) was performed using Tecnai T12 transmission electron microscope operating of 120 kV and JEOL JEM-2100 microscope operating at 200 kV. The samples for TEM observation were prepared by drop-casting a solution on a carbon film supported on a copper grid. Scanning electron microscopy(SEM) was performed on TESCAN Vega3 SBH. Optical absorption spectra were measured by Ocean Optics HR2000CG-UV-NIR spectrometer. X-ray diffraction (XRD) patterns were measured using a PANalytical Empyream diffractometer with Cu Kα radiation λ = 1.5406 Å with a graphite monochromator (40 kV, 40 mA). Raman measurements were conducted using ThermoFisher DXR SmartRaman. Zeta potential measurements of the colloidal dispersions were performed using a Beckman Coulter Delsa Nano C Zeta Potential Analyzer. The near-edge (XANES) S *K*-edge, Mo L_3-edge, Fe $L_{2,3}$-edge, and O K-edge spectra were measured at Advanced Light Source (ALS) beamlines 10.3.2 and 8.0.1.1 (iRIXS) in Lawrence Berkeley National Laboratory. The storage ring condition is 1.9 GeV and 500 mA current in a multi-bunch operation mode.

The Xray absorption spectroscopy (XAS) spectra for S *K*-edge and Mo L_3-edge were collected in total fluorescence yield (TFY) mode, and Fe $L_{2,3}$-edge and O *K*-edge were collected in both TFY and total electron yield (TEY) modes. Beamline 10.3.2 used a Si (111) monochromator with energy ranging from 2.1 to 17 keV, a tunable spot size ranging from 0.8 × 0.8 up to 8 × 5 μm^2, and a resolving power ($E/\Delta E$) of 7000 at 10 keV. The solid samples measured at room temperature were positioned at a normal incidence of the X-ray beam. The fluorescence signal was collected using a silicon drift fluorescence detector placed at 45^o to the X-ray beam. Baseline I_0 was measured using an in-line nitrogen-filled ionization chamber situated in front of the sample. The raw data were processed and normalized using Athena software.[15] The undulator beamline 8.0.1 offers a high flux beam at 100 × 35 μm^2 with an energy region of 80-1200 eV. All spectra were normalized to the incident photon flux after delicate calibrations to the reference samples. Both TEY and TFY spectra were collected simultaneously in the main chamber of iRIXS, with a base pressure of 8×10^{-10} Torr.

4.3 Results and discussion

4.3.1 Colloidal coating of a-MoS_x on SiO_2

The proposed method employs molybdenum sulfide as a transitional coating layer to anchor magnetic iron oxide particles. We take advantage of the instantaneous and straightforward attachment of both materials that do not require special solvents or chemical reagents, change in reaction conditions, or supplying power to the reaction (e.g., currents). However, coating molybdenum sulfide on nanostructured materials is not a well-established technique, where different coating conditions and procedures might be

required depending on the core nanomaterials' physical and chemical properties. Instead, we developed a general colloidal coating method of molybdenum sulfide on SiO_2 coating owing to the university and simplicity of the latter coating method. In this design, SiO_2 could be coated first on the nonmagnetic materials, followed by coating a transitional layer of molybdenum sulfide that will anchor the magnetic iron oxide particles.

The molybdenum sulfide NPs used on the colloidal coating method is based on sulfur-rich amorphous molybdenum sulfide (a-MoS_x) materials. This class of amorphous materials includes chemical compounds comprising Mo to S ration between 2 and 6. These sulfur-rich MoS_x compounds are semiconductor materials with narrow band gaps reaching 1.2 eV.[16] The typical synthesis of a-MoS_x particles involves the acidification process of $(NH_4)_2MoS_4$.[16–19] The thermal decomposition of $(NH_4)_2MoS_4$, or the thermally-assisted transformation of amorphous a-MoS_x leads to the formation of MoS_2 particles.[19] Dissolution of $(NH_4)_2MoS_4$ in aqueous solutions produces tetrathiomolybdate anion (MoS_4^{2-}) that reacts with mineral acids to form a-MoS_x. There is no consensus in the literature concerning the number of molybdenum atoms in the molybdenum sulfide structure. MoS_3 structure was initially thought to form as the final product; however, further analysis revealed the formation of many structures in the form of short-range metal-sulfur macromolecules. These quasi-one-dimensional compounds consist of either inorganic polymeric, oligomeric, or monomeric structures.[16,20]

Figure 4.1 represents the colloidal coating procedure of amorphous molybdenum sulfide on SiO_2 nanoparticles. This colloidal process is also based on the acidification of ammonium tetrathiomolybdate. The process starts with modifying the SiO_2 surface with

amine groups using APTES molecules, followed by the absorption of $n[MoS_x]S^{2-}$ complexes on the surface of APTES- SiO_2. The acidification of $n[MoS_x]S^{2-}$ complexes by lowering the pH level in the reaction induces the coating of a-MoS_x nanoparticles on SiO_2. The TEM image in Figure 4.2a confirms the colloidal coating of a-MoS_x layer on SiO_2 nanospheres. XRD pattern of SiO_2@a-MoS_x shown in Figure 4.2b agrees with the amorphous nature of a-MoS_x with only two broad peaks centered at ~14° and ~20° corresponding to a-MoS_x and SiO_2 pattern, respectively.[21] Raman spectrum in Figure 4.2c demonstrates the vibration bands of MoS_x in good agreement with previous results.[21] The absorption bandgap of the synthesized SiO_2@a-MoS_x was measured to be 1.24 eV by plotting the Tauc plot of its UV-vis-NIR absorption in Figure 4.2d, which is in excellent agreement with the reported bandgap of a-MoS_x.[16]

XPS analysis of SiO_2@a-MoS_x shown in Figure 4.3a & b represents the sulfur 2p region and molybdenum 3d region, respectively. A single peak associated with terminal disulfide ligands $(S\text{-}S)_t$ (162.5 eV), and two singlet peaks associated with bridging or shared disulfide ligands $(S\text{-}S)_{br/sh}$ (163.8 eV and 164 eV) are observed in the sulfur 2p region. The proximity of the terminal ($S2p_{3/2}$) and bridging or shared disulfide ($S2p_{1/2}$) peaks is responsible for the triplet-like appearance of SiO_2@a-MoS_x sulfur XPS peak. A single peak appeared in the molybdenum 3d region (Figure 4.3b) associated with S 2s signal, where its broadness feature is indicative of the presence of various oxidation states of sulfur atoms.[16] Two doublet peaks corresponding to Mo-S and Mo-O bonds are present in the Mo 3d XPS of SiO_2@a-MoS_x. This presence of oxygen defects is a typical feature of a-MoS_x structure.[16] The composition ratio of sulfur to molybdenum was

calculated based on XPS results, attaining a ratio of 78:22 of S:Mo, which indicates a stoichiometry close to $MoS_{3(2/3)}$.[16,21–23]

The electrostatic interactions are believed to be responsible for the preferential deposition of a-MoS_x on APTES-SiO_2.[13] When we performed the same colloidal coating of a-MoS_x on bare SiO_2 (without APTES modification), self-nucleation of a-MoS_x into amorphous sheets was observed without any deposition on the silica surface, indicating the essential role of APTES on their interaction (Figure 4.4a). Zeta-potential measurements were performed to assess this hypothesis. Zeta potential is a measure of the magnitude of electrostatic charges (repulsion/attraction) between two materials. Bare SiO_2 colloidal particles produced -67 mV zeta potential value (Figure 4.4b), which is consistent with the reported value of SiO_2 colloids prepared via the Stöber method.[24] The negatively charged value is attributed to the presence of hydroxyl groups on the SiO_2 surface. APTES-SiO_2 showed +20 mV zeta potential value because of the positively charged amine groups on APTES molecules (Figure 4.4b). However, bare a-MoS_x nanoparticles possessed negative zeta potential of around -50 mV, which is attributed to the existence of negatively charged sulfur atoms in the material's structure. These opposite charges create an electrostatic attraction between a-MoS_x and APTES-SiO_2, ensuring their binding during the colloidal coating process. The zeta potential of the final product APTES-SiO_2@a-MoS_x (-33 mV) also revealed the successful coating of negatively charged a-MoS_x on APTES-SiO_2 (Figure 4.4b).

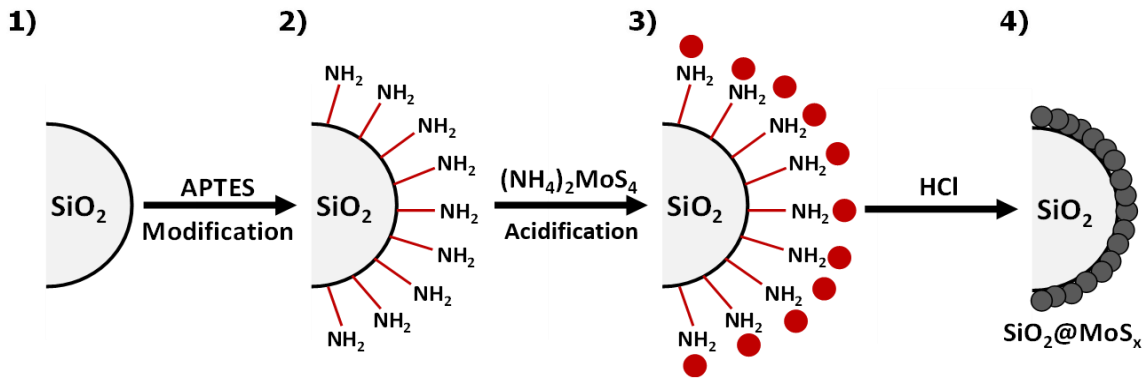

Figure 4.1 Schematic illustration of the colloidal coating of molybdenum sulfide on SiO_2 nanoparticles. (2) The modifying of SiO_2 surface with amine groups using APTES. (3) Absorption of $n[MoS_x]S^{2-}$ complexes on the surface of APTES modified SiO_2. (4) Acidification of $n[MoS_x]S^{2-}$ complexes to coat amorphous MoS_x nanoparticles on SiO_2.

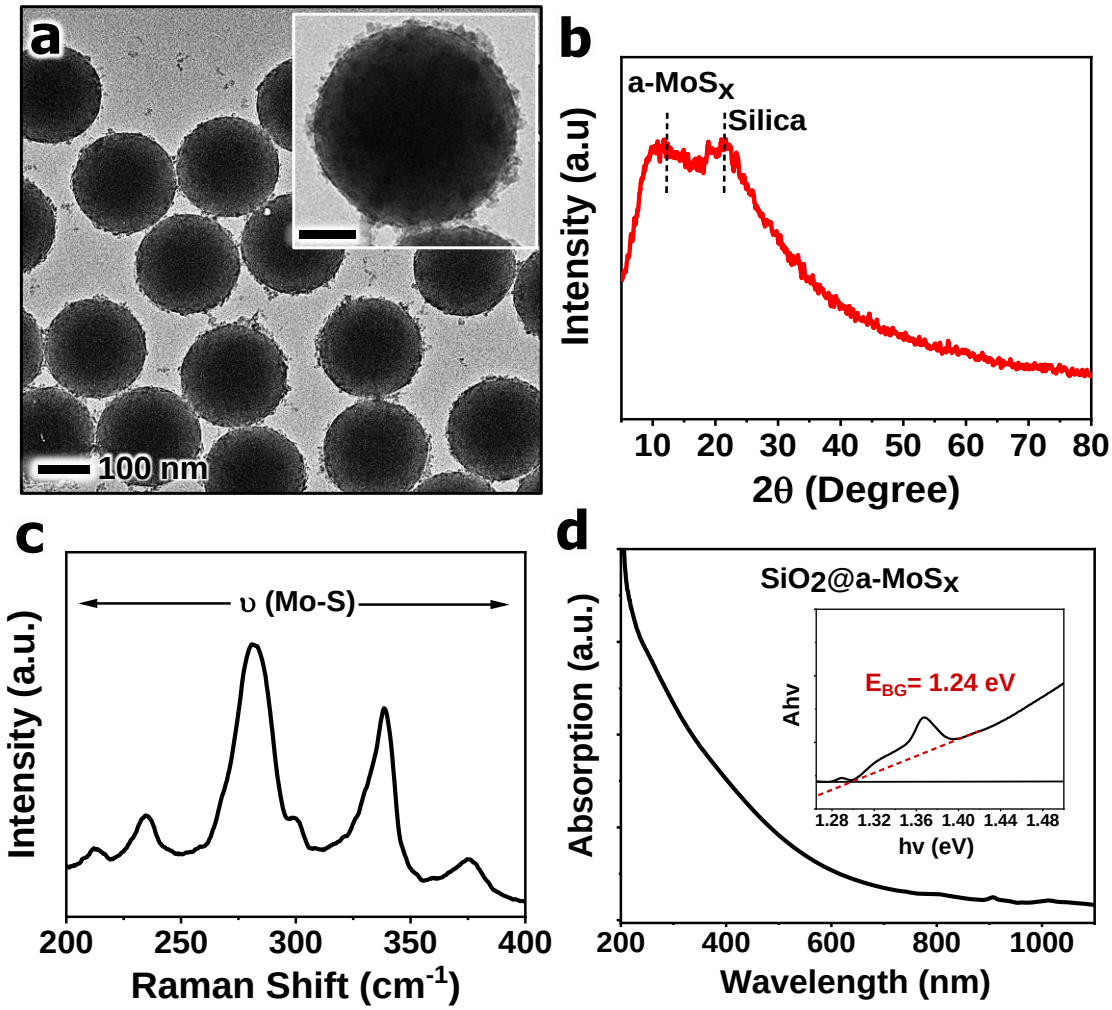

Figure 4.2 (a) TEM image of SiO_2@a-MoS_x NPs. Inset image scale 50 nm. (b) XRD diffraction of SiO_2@a-MoS_x NPs. (c) Raman spectra of SiO_2@a-MoS_x NPs. (d) UV-vis-NIR absorption of SiO_2@a-MoS_x; and the corresponding Tauc plot (inset).

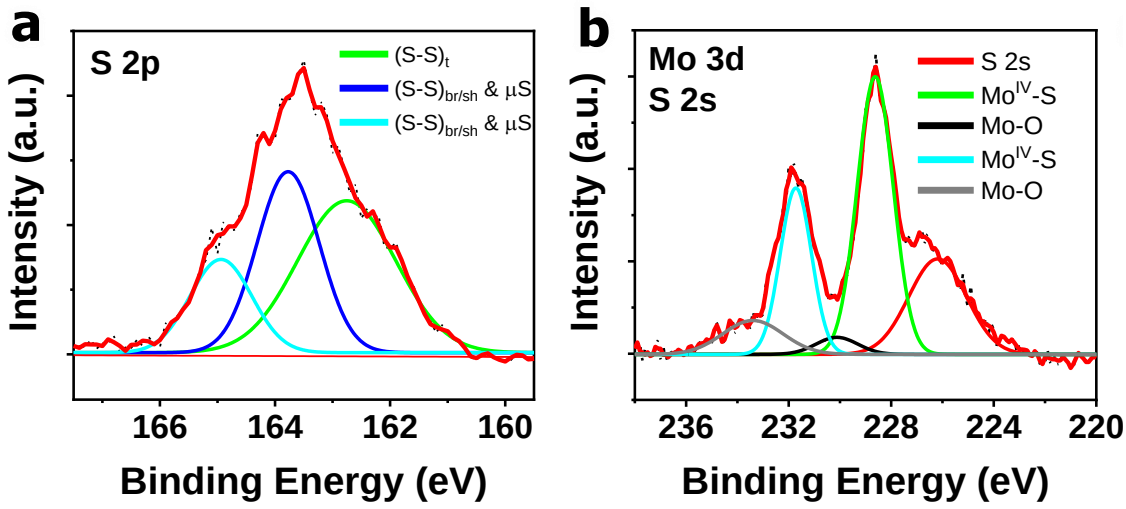

Figure 4.3 XPS spectra of SiO_2@a-MoS_x NPs (a) S 2p and (b) Mo 3d regions.

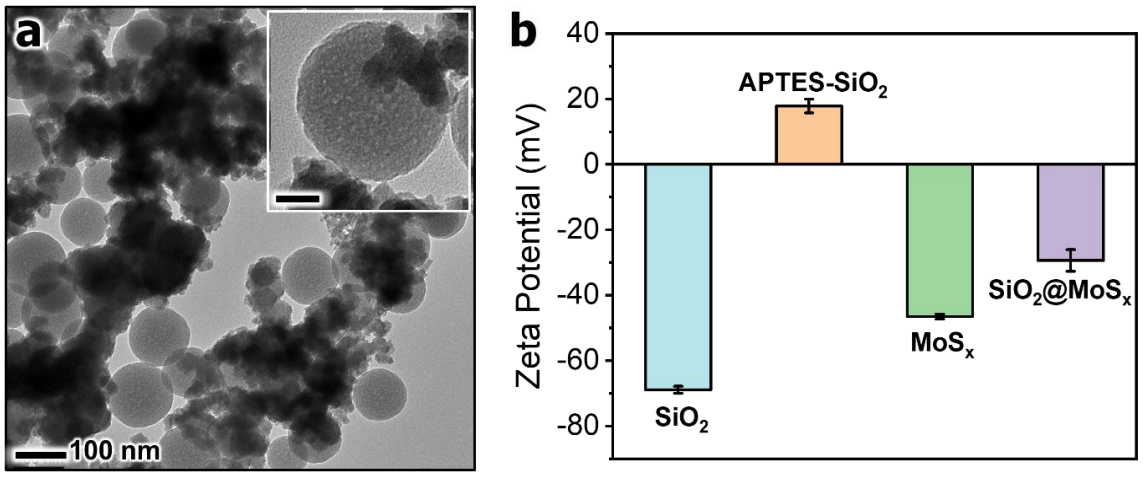

Figure 4.4 (a) TEM image of bare SiO_2 mixed with a-MoS_x. Inset images scale bar 50 nm. (b) Zeta-potential measurements of SiO_2, APTES-SiO_2, MoS_x, and APTES-SiO_2@MoS_x.

The formation of the a-MoS_x layer is based on the acidification reaction of $(NH_4)_2MoS_4$, which is known to endure various formation mechanisms and kinetics under different alkalinity.[20] UV-vis absorption was performed to understand the characteristics of $(NH_4)_2MoS_4$ suspension solution at different pH levels by HCl adjustment (Figure 4.5). In an acidic environment, a distinct peak appeared at around 470 nm attributed to the formation of $n[MoS_x]S^{2-}$ complex (Figure 4.5c).[25] When further decreasing the pH value to below 6, this peak started to evolve until completely vanishing at pH < 3, accompanied by a color change of the solution from red to black and the formation of black particles (a-MoS_x). Excessive HCl (pH < 1.5) leads to the aggregation and precipitation of a-MoS_x particles (Figure 4.5b and c). The kinetics of this reaction are found to be extremely rapid, reaching a complete conversion in less than 60 s, while fixing the pH value at 6.54. The a-MoS_x formation involves the protonation of either terminal S^{2-} (or O^{2-}) in $n[MoS_x]S^{2-}$ complex, leading to an electron transfer from S^{2-} to Mo by altering the stabilized π-systems, and hence the formation of several polynuclear thiomolybdates molecules.[20] During the hydrolysis reaction of $n[MoS_x]S^{2-}$ complex, O^{2-} replaces the terminal or apical S^{2-} atoms. The thiomolybdates and polysulfide products react to form thiomolybdates with high-order of sulfur atoms. These reactions undergo in the presence of protons from acidic solutions or water.[20]

Controlling the thickness of a-MoS_x on APTES-SiO_2 could be achieved by governing the a-MoS_x precursor amount during the acidification reaction. Figure 4.6 represents the investigation of the growth of a-MoS_x coating thickness on APTES-SiO_2 NPs by controlling the precursor amount. Increasing $(NH_4)_2MoS_4$ precursor solution has

led to an increase of a-MoS_x coating thickness, as seen in the TEM images in Figure 4.6a-c. The relationship between a-MoS_x thickness and precursor amount is illustrated in Figure 4.6d. A direct-correlation was noticed between a-MoS_x thickness and the increase of $(NH_4)_2MoS_4$ injection volume; however, this incremental behavior reached a plateau after reaching an average of 18 nm a-MoS_x thickness. These results were consistent with the UV-vis absorptions of APTES-SiO_2@a-MoS_x solutions with various thicknesses of a-MoS_x. The UV-vis absorptions illustrated a gradual broadening and intensity increment with a larger a-MoS_x thickness in APTES-SiO_2@a-MoS_x (Figure 4.6e). This peak broadening is attributed to the optical properties of a-MoS_x evidence by its black color, where increasing the concentration of these materials surrounding APTES-SiO_2 will expand its UV-vis absorption profile.

Additionally, the relation between the reaction time and the colloidal coating of a-MoS_x on APTES-SiO_2 was investigated in Figure 4.7. The colloidal coating step of a-MoS_x was found to be completed in less than 30 seconds (inset in Figure 4.7a). Prolonging the reaction time to even 30 minutes did not result in any change of a-MoS_x coating thickness, indicating the completion of the reaction in the 30 seconds (Figure 4.7a). The TEM images in Figure 4.7b also support these findings, where no significant changes are noticed in the a-MoS_x layer after 1, 15, and 30 min reaction time intervals.

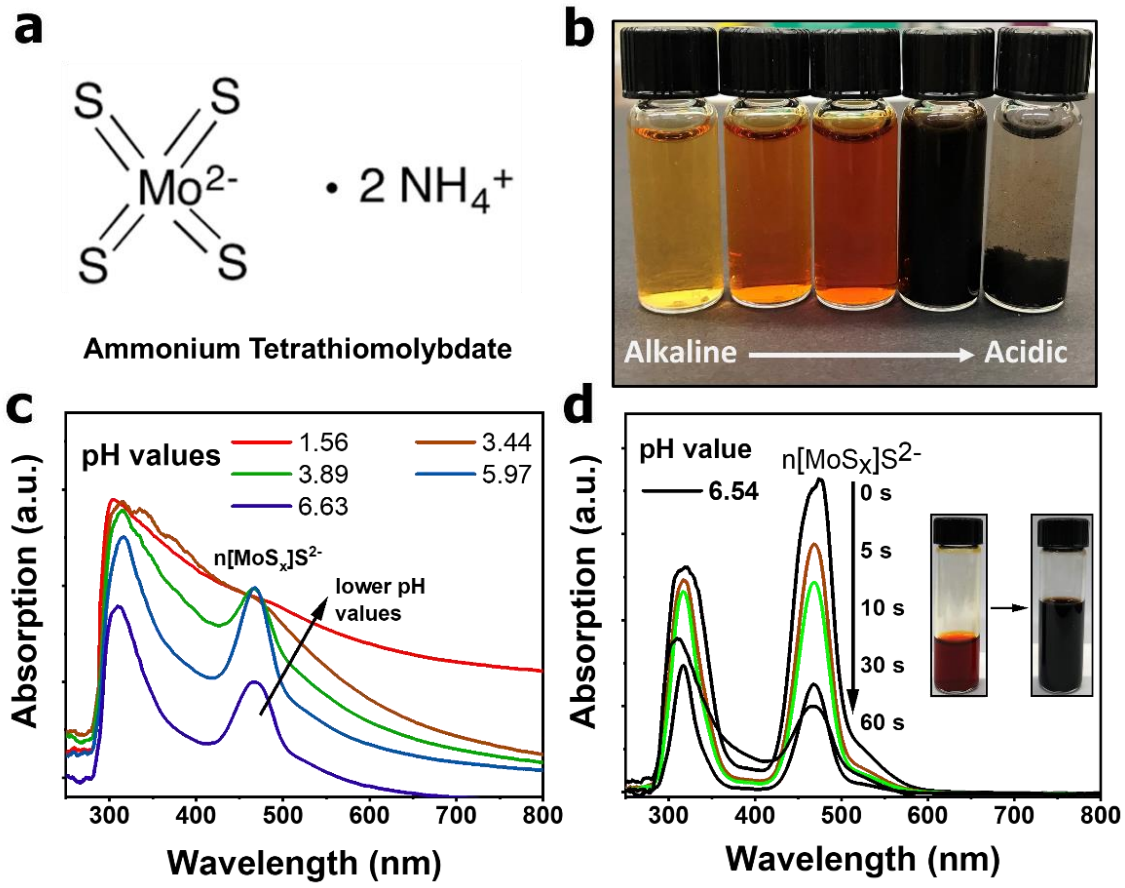

Figure 4.5 (a) Chemical structure of ammonium tetrathiomolybdate precursor. (b) Images of ammonium tetrathiomolybdate solutions with different alkalinity. (c) UV-vis absorptions of ammonium tetrathiomolybdate solutions under different pH values. (d) UV-vis of ammonium tetrathiomolybdate solution with a pH of 6.54 showing the evolution of peak at 475nm in 60 seconds.

.

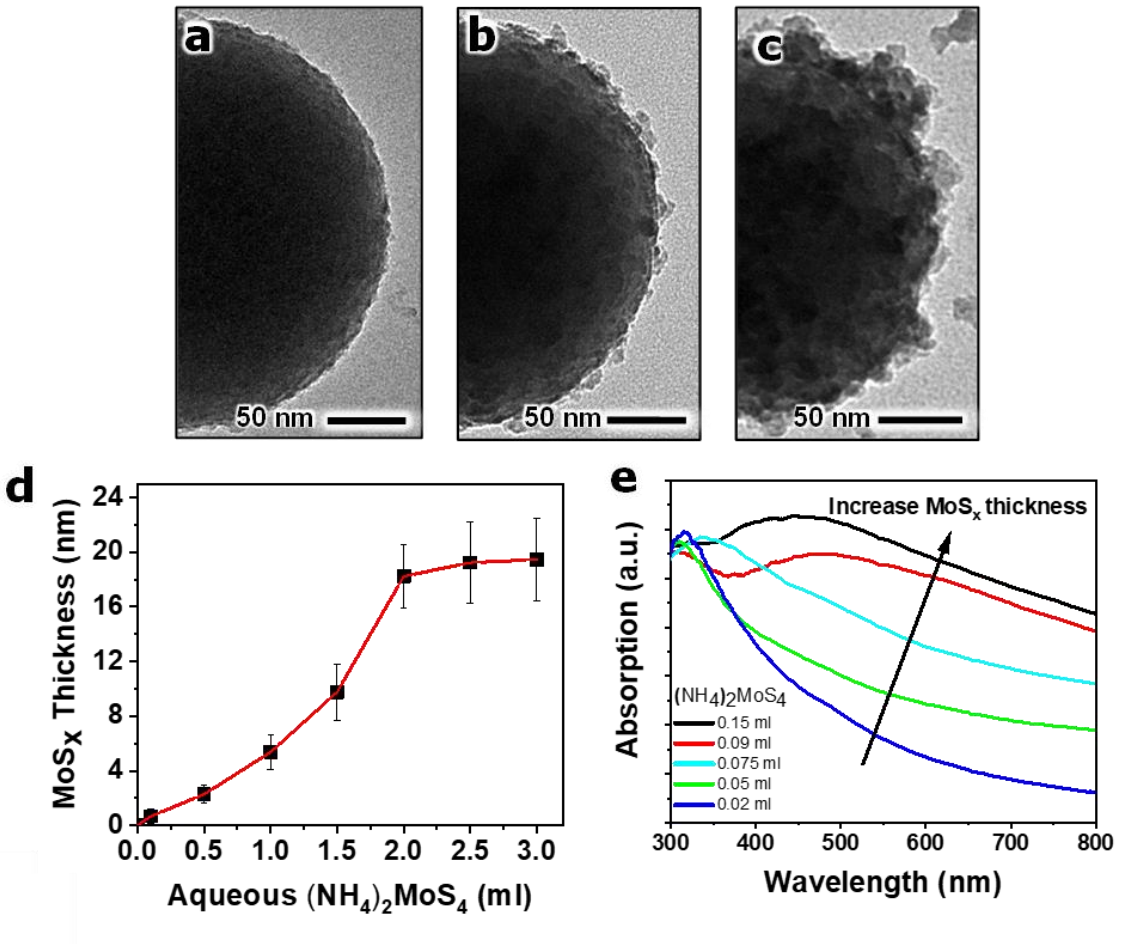

Figure 4.6 (a-c) TEM images of APTES-SiO_2@a-MoS_x with different thicknesses of a-MoS_x. (d) The relationship between a-MoS_x thickness and precursor amount. (e) UV-vis absorptions of APTES-SiO_2@a-MoS_x with different thicknesses of a-MoS_x.

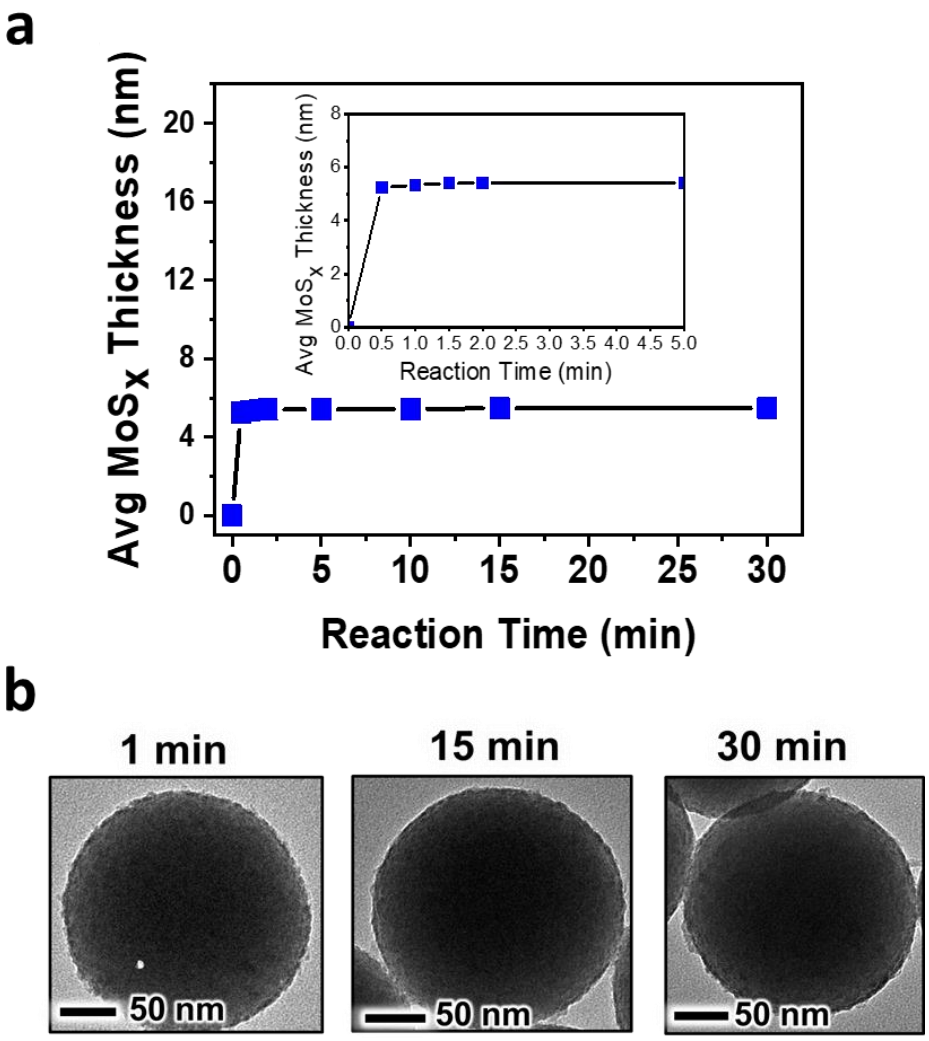

Figure 4.7 (a) The relationship between the reaction time and a-MoS_x coating thickness on APTES-SiO_2. (b) TEM images of APTES-SiO_2@a-MoS_x under different reaction times.

4.3.2 a-MoS_x and Fe_3O_4 interaction mechanism

We decided next to study the underlying interaction mechanism between Fe_3O_4 and a-MoS_x by carrying out a series of surface characterization measurements. Firstly, we tested the binding between a-MoS_x NPs and commercial Fe_3O_4 NPs by mixing both materials in aqueous solution. An immediate aggregation of the two particles was observed (Figure 4.8a & b), confirming the instantaneous and robust interaction between both materials, agreeing with the observation between bulk molybdenum sulfide and commercial iron oxide reported previously. These composite aggregates could be entirely separated by applying an external magnetic field, further demonstrating the strong binding between both materials. FTIR measurements were taken for a-MoS_x, Fe_3O_4, and a-MoS_x/Fe_3O_4 composite to disregard the possibility of a-MoS_x and Fe_3O_4 binding through surface complexation by organic ligands, as shown in Figure 4.8c. The results confirm the absence of organic molecules characteristics FTIR peaks, indicating that the binding between a-MoS_x and Fe_3O_4 might occur through a chemical bonding mechanism. Additionally, we excluded the mechanism of electrostatic attraction between a-MoS_x and Fe_3O_4, since both materials possess negative surface charges (Figure 4.4b).

XPS analysis can give further insights into the chemical and electronic states of a-MoS_x/Fe_3O_4 composite. Figure 4.9 shows the XPS S 2p and Mo 3d of a-MoS_x and a-MoS_x/Fe_3O_4 composite materials. There were no significant differences between the XPS S 2p peaks of a-MoS_x and a-MoS_x/Fe_3O_4, which indicate that the formation of Fe-S bonds between a-MoS_x and a-MoS_x/Fe_3O_4 could be excluded. However, a new peak was observed in the XPS Mo 3d analysis of a-MoS_x/Fe_3O_4 at around 235.5 eV attributed to

the oxidation state of Mo^{6+}.[10] This peak could form due to the oxidation of exposed Mo^{4+} to Mo^{6+} in a-MoS_x structure by forming a Mo-O-Fe bond. Additionally, XAS analysis will provide more understandings of the bond formation owing to its high sensitivity to chemical and electronic structures. There were no significant differences between the XAS S *K*-edge spectra of a-MoS_x and a-MoS_x/Fe_3O_4 composite, as seen in Figure 4.10a, also indicating that no bond formed between the S atoms in a-MoS_x and Fe_3O_4. Figure 4.10b shows the XAS Mo L_3-edge spectra of a-MoS_x and a-MoS_x/Fe_3O_4 composite. The *L*-edge corresponds to the allowed 2p to 4d transitions at Mo, with intrinsic energy resolution higher than *K*-edges, providing higher quantitative measurements of Mo oxidation states.[26] Mo L_3-edge spectrum of a-MoS_x indicated the presence of only t_{2g} corresponding to the Mo oxidation state of +4. However, the Mo L_3-edge spectrum of a-MoS_x/Fe_3O_4 composite confirmed the presence of a second peak at 2528 eV corresponding to the Mo oxidation state of +6.[27] This peak is also observed with the presence of oxygenated molybdenum (Mo-O-) compounds in the mixture.[28] We conclude from these findings that the dominant binding mechanism of a-MoS_x and Fe_3O_4 is based on the chemical bonding between the molybdenum in a-MoS_x and oxygen in Fe_3O_4 in the form of (Mo-O-Fe), which oxidizes the molybdenum from the oxidation state of +4 to +6.

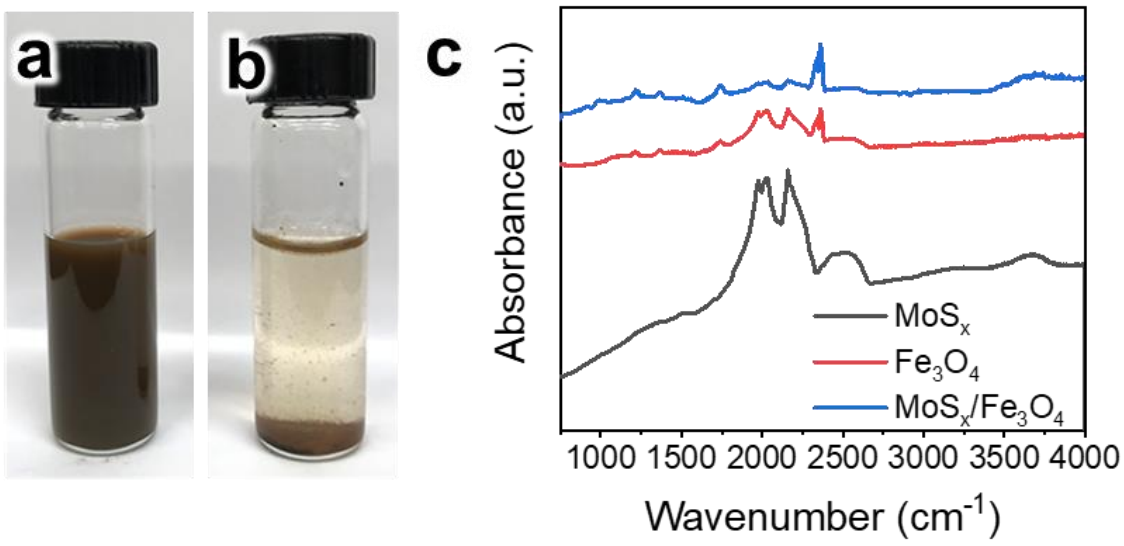

Figure 4.8 Digital images of the aqueous solutions of (a) a-MoS_x NPs mixed with Fe_3O_4 NPs and (b) their aggregated particles. (c) FTIR spectra of a-MoS_x, Fe_3O_4, and a-MoS_x/Fe_3O_4 composite.

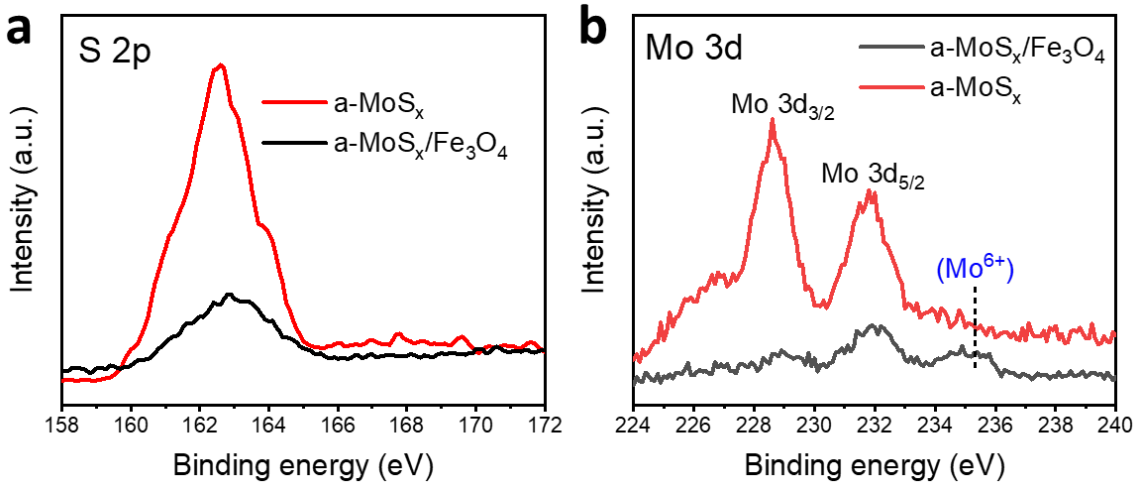

Figure 4.9 XPS spectra of (a) S 2p and (b) Mo 3d regions of a-MoS_x and a-MoS_x/Fe_3O_4 composite.

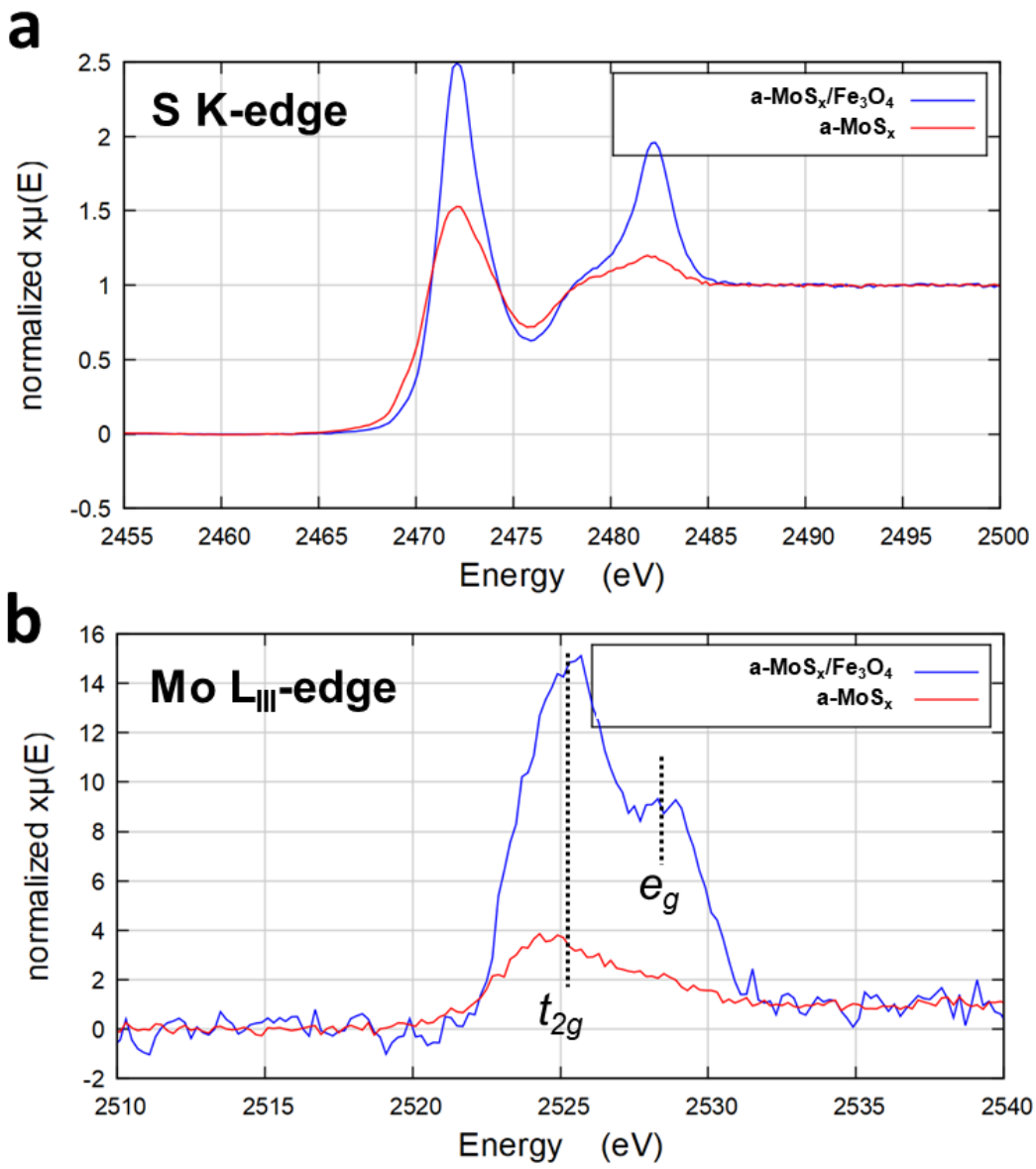

Figure 4.10 Normalized (a) S *K*-edge and (b) Mo L_3-edge XANES spectra of a-MoS_x and a-MoS_x/Fe_3O_4 composite.

4.3.3 Attachment of magnetic iron oxide onto APTES-SiO_2@a-MoS_x

The schematic representation shown in Figure 4.11 demonstrates the attachment process of magnetic iron oxide NPs onto APTES-SiO_2@a-MoS_x. The attachment occurs without adding any chemical reagents or changing the reaction conditions. It only requires the physical mixing of each material in solvents such as water and ethanol. 5 min of agitating was found to be efficient to bind both particles strongly. A comparison study was performed by adding commercial magnetic iron oxide particles into particles suspension of APTES-SiO_2 and APTES-SiO_2@a-MoS_x to demonstrate the importance of a-MoS_x on this process (Figure 4.11(a-d)). As seen in Figure 4.11a & b, Fe_3O_4 NPs were mixed with the aqueous solutions of APTES-SiO_2 and APTES-SiO_2@a-MoS_x, respectively. After 5 min of agitating, each solution was exposed to a magnetic field using a magnet to induce magnetic particle separation. As seen in Figure 4.11c, only the magnetic Fe_3O_4 NPs were separated, while the APTES-SiO_2 NPs were left in the aqueous solution showing a turbid and milky color. However, a transparent aqueous solution was observed for the mixture of Fe_3O_4 and APTES-SiO_2@a-MoS_x NPs after applying a magnetic field, indicating the attachment of the magnetic Fe_3O_4 onto APTES-SiO_2@a-MoS_x NPs (Figure 4.11d). This result was also supported by the TEM image of Fe_3O_4 + APTES-SiO_2@a-MoS_x mixture, which illustrates the attachment of large aggregates of commercial Fe_3O_4 onto the silica spheres (Figure 4.11e). We also found that various shapes and structures of magnetic iron oxide could be used in this binding strategy, including cubic iron oxide, FeO, and Fe_3O_4 nanorods. The strong binding between Fe_3O_4 and a-MoS_x was found to be extremely stable after performing several magnetic

separations and redispersion cycles (Figure 4.12a), in addition to storing the colloidal mixture in the solution for 30 days (Figure 4.12b). No significant changes in the percentage of APTES-SiO_2 attached by Fe_3O_4 were noticed in each case, indicating that disengagement did not occur between the two particles.

4.3.4 Magnetizing Au micromirrors

To demonstrate the applicability of this approach, we attached magnetic iron oxide nanoparticles onto large Au microplates using a-MoS_x and Fe_3O_4 interaction to fabricate magnetically tunable colloidal micromirrors. The previous synthesis method of magnetic Au micromirrors involves tedious chemical modifications of Au microplates and iron oxide nanoparticles. The synthesized Fe_2O_3@SiO_2 NPs must be modified by amine-terminated functional groups to adhere to the Au surface through binding the lone amine pairs and metallic Au bonds. Additionally, this ferrofluid had to undertake several ligand-exchange steps to achieve its aqueous phase transfer. This typical fabrication method could take up to 2 days to synthesize the final magnetically-tunable Au micromirrors.[14] The a-MoS_x magnetizing method could shorten the fabrication time to less than 15 min without utilizing any chemicals, implying high cost-saving and time-saving. This approach consists of only coating the synthesized Au microplate with a-MoS_x and then attaching the magnetic nanoparticles onto the material's surface. Commercial magnetic iron oxide could also be used instead of synthesized ones, portraying the cost advantages of using the described magnetizing method.

Figure 4.13a shows the TEM image of Au microplate coated with a-MoS_x. These results indicate that the colloidal coating method of a-MoS_x is not limited to nanoscale

particles, but it also applies to microscale sizes. The conjugation of magnetic nanoparticles onto Au@a-MoS_x is evident from the TEM and SEM images of Au@a-MoS_x microplate attached with magnetic Fe_3O_4 nanoparticles shown in Figure 4.13b & c, respectively.

These microplates could then be magnetically manipulated to induce optical properties changes that are apparent in bulk solution. In the absence of a magnetic field, the Au@a-MoS_x microplates solution exhibits a turbid, golden color similar to bulk Au color. As seen in Figure 4.14, upon applying a magnetic field parallel to the viewing angle, the microplates rapidly aligned with the applied field, obtaining a transparent solution characteristic because of the minimized cross-section of the microplates.[14] As the angle between viewing direction and magnetic field increases, the microplates solution becomes more opaque and reflective (Figure 4.14b-d), until reaching a maximum reflection at 90^o owing to the maximum projected cross-section of the microplates when the magnetic field is perpendicular to the viewing angle (Figure 4.14d). Despite the coating and attachment of a-MoS_x and Fe_3O_4, the Au microplates maintain its golden and shiny color with minimum darkening, which might be attributed to the small contents of the adhered a-MoS_x and Fe_3O_4 in respect to the Au microplate size.

We believe this system to be valuable for tunable optical applications such as smart windows and thermoregulators. The magnetizing method provides crucial advantages in reducing the time and cost for fabricating such materials, which is critical when applying the system for a large scale.

4.4 Conclusions

A universal magnetizing method of nanostructured materials was developed based on employing a-MoS_x as a transitional layer, which strongly anchors magnetic iron oxide particles. The underlying mechanism relies on the strong binding between molybdenum sulfide and iron oxide through the chemical bonding of (Mo-O-Fe). The oxygenation of the Mo exposed sites in a-MoS_x oxidizes Mo^{+4} into Mo^{+6} during the binding process. To attain higher versatility of the magnetizing technique, we developed a colloidal coating method of a-MoS_x on SiO_2, which could be implemented on various nanostructured materials. The colloidal coating method consists of the surface modification of SiO_2 with APTES, followed by the acidification of $(NH_4)_2MoS_4$. Magnetic iron oxide could adhere directly to APTES-SiO_2@a-MoS_x nanostructures by simply mixing both materials in polar solvents in less than 1 min. We demonstrated the practicality and advantage of this technique by magnetizing Au microplates in ~15 min, tremendously shorter than a prior magnetizing method that required ~2 days of multiple Au microplates' surface functionalizations. The versatility, practicality, rapid functionalization, high stability, and low toxicity and cost are crucial advantages for engineering the magnetic responsiveness in nanostructured materials for applications such as bioimaging and drug delivery.

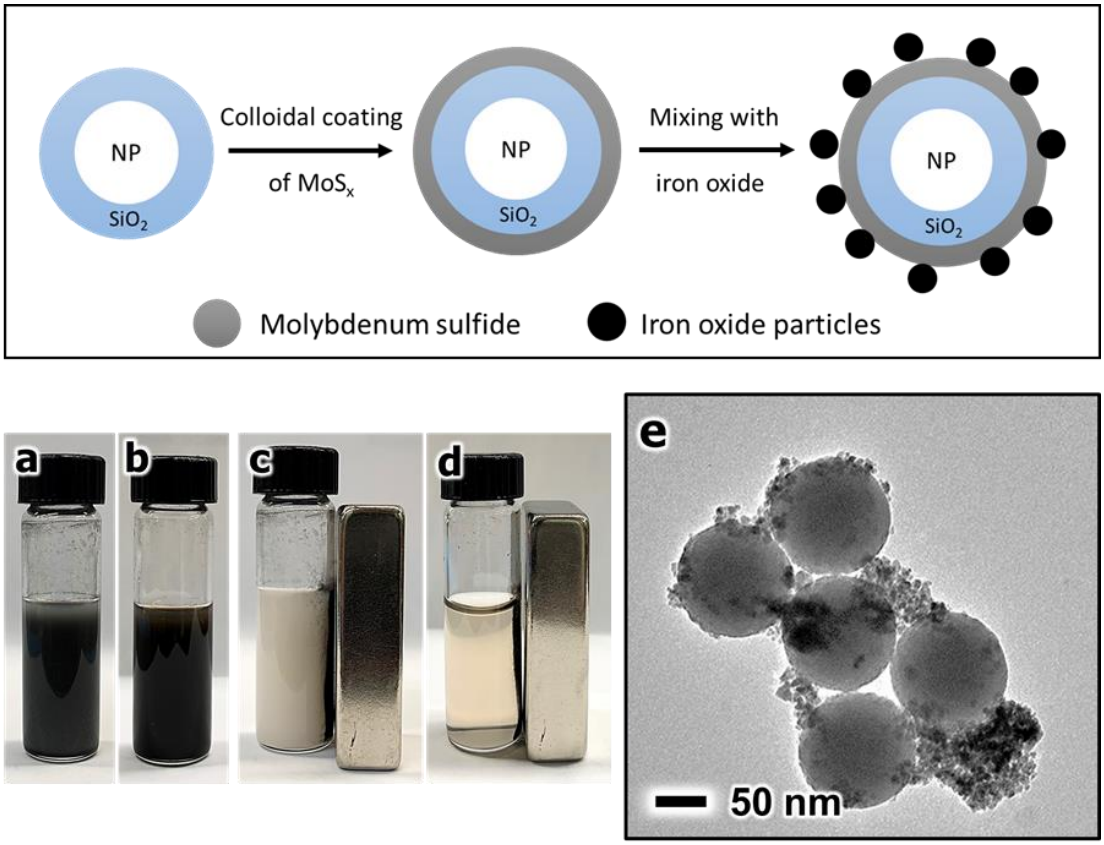

Figure 4.11 Schematic representation of the binding strategy of NP@SiO_2@MoS_x and iron oxide NPs. Digital images of aqueous solutions of (a) APTES-SiO_2+Fe_3O_4, (b) APTES-SiO_2@a-MoS_x+Fe_3O_4, (c) APTES-SiO_2+Fe_3O_4 under a magnetic field, and (d) APTES-SiO_2@a-MoS_x+Fe_3O_4 under magnetic field. (e) TEM image of APTES-SiO_2@a-MoS_x+Fe_3O_4 NPs.

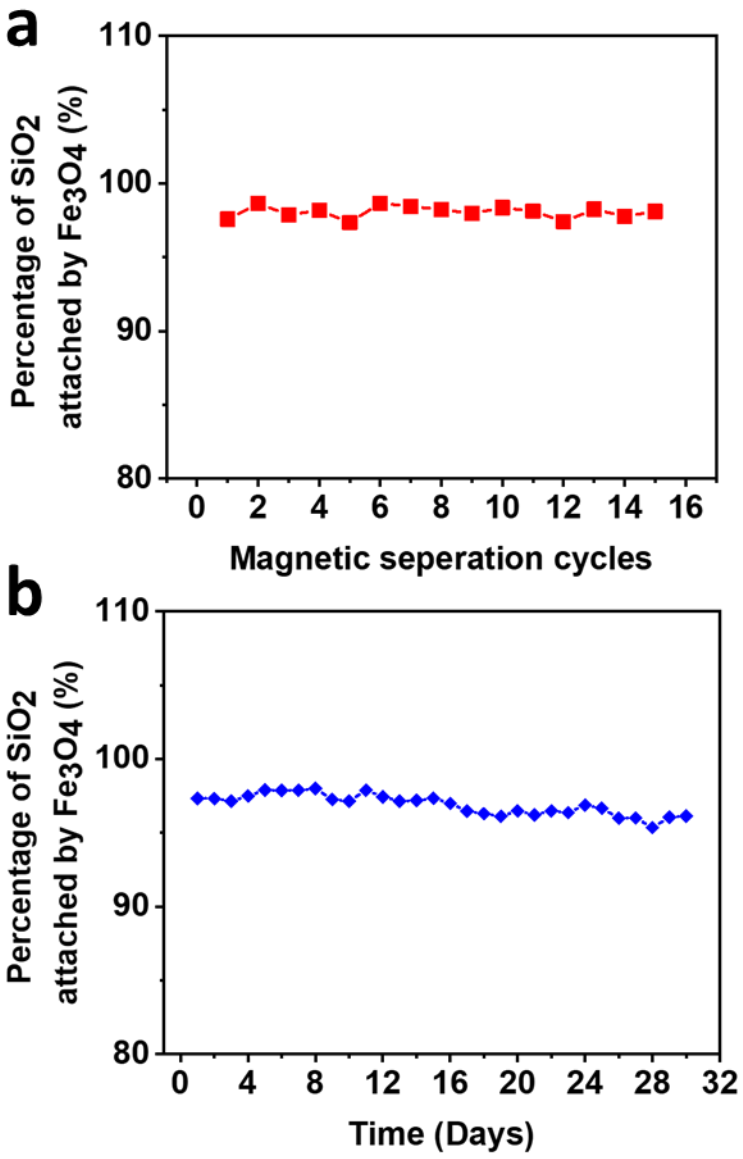

Figure 4.12 (a) The correlation between the percentage of APTES-SiO_2 attached by Fe_3O_4 vs. the magnetic separation and redispersion cycles of APTES-SiO_2/Fe_3O_4 NPs. (b) The change of APTES-SiO_2 attached by Fe_3O_4 vs. time in the same aqueous mixture.

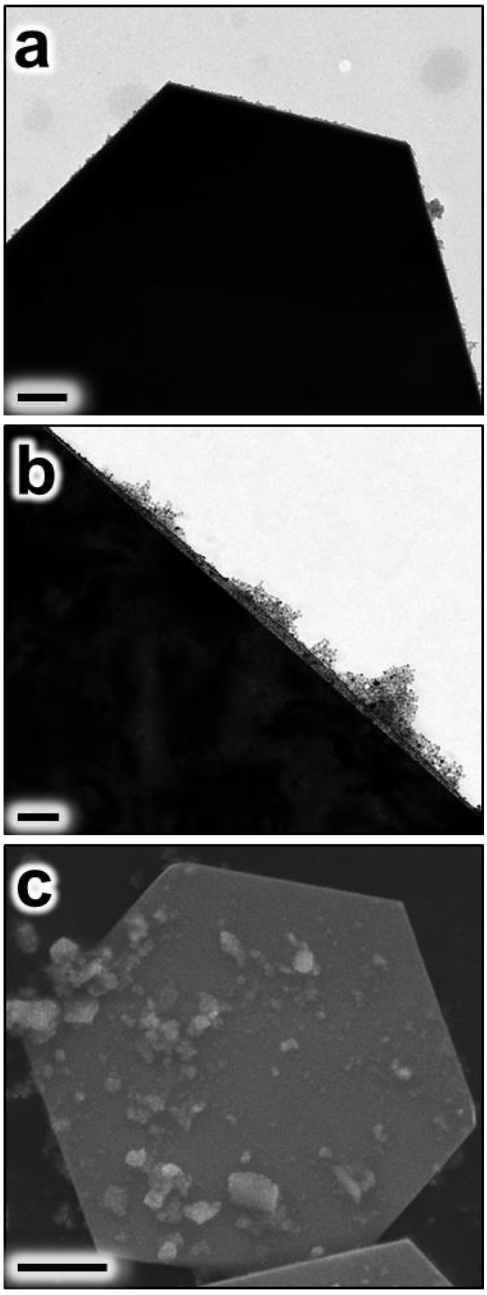

Figure 4.13 (a) TEM image of Au microplate coated with a-MoS_x. (b) TEM image of Au@a-MoS_x microplate attached with magnetic Fe_3O_4 nanoparticles. (c) SEM image of Au@a-MoS_x microplate attached with magnetic Fe_3O_4 nanoparticles. Scale bar 200 nm.

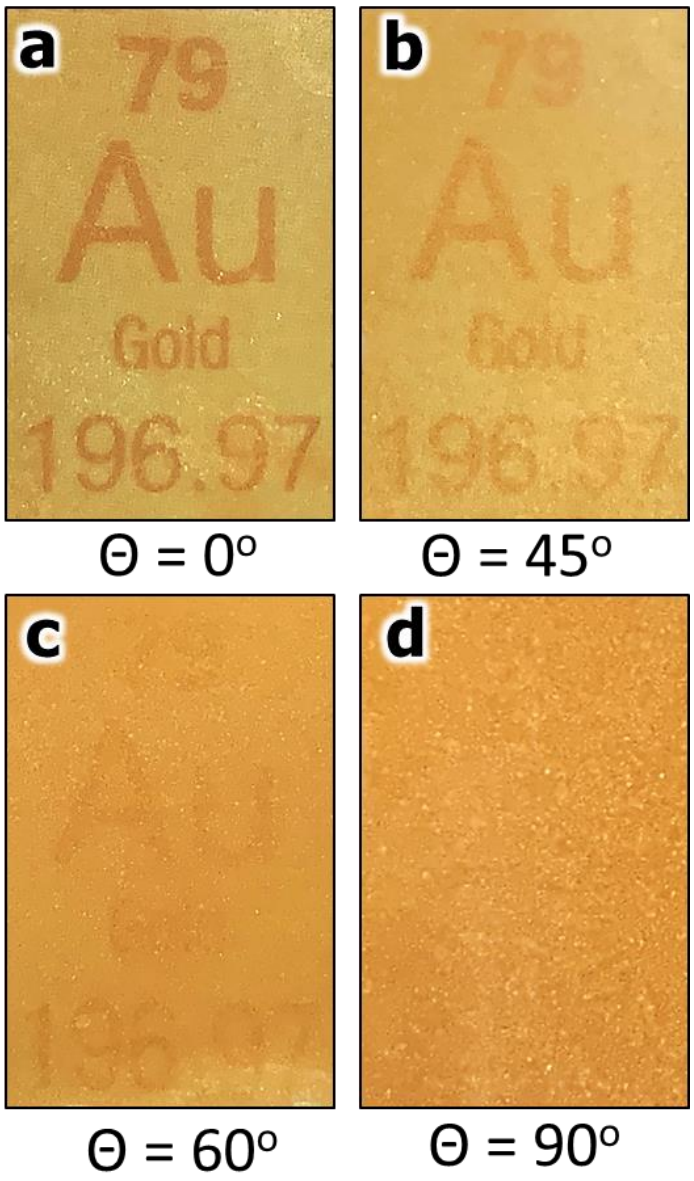

Figure 4.14 (a) Digital images of bulk magnetic microplate solution of Au@a-MoS_x/Fe_3O_4 under an applied magnetic field with various orientations (θ) relative to the viewing angle.

4.5 References

[1] Z. Li, F. Yang, Y. Yin, *Adv. Funct. Mater.* **2020**, *30*, 1903467.

[2] M. Grzelczak, L. M. Liz-Marzán, R. Klajn, *Chem. Soc. Rev.* **2019**, *48*, 1342–1361.

[3] Z. Li, Y. Yin, *Adv. Mater.* **2019**, *31*, 1807061.

[4] J. Alonso, J. M. Barandiarán, L. Fernández Barquín, A. García-Arribas, in *Micro Nano Technol.* (Eds.: A.A. El-Gendy, J.M. Barandiarán, R.L.B.T.-M.N.M. Hadimani), Elsevier, **2018**, pp. 1–40.

[5] S. Gul, S. B. Khan, I. U. Rehman, M. A. Khan, M. I. Khan, *Front. Mater.* **2019**, *6*, 179.

[6] J. Kudr, Y. Haddad, L. Richtera, Z. Heger, M. Cernak, V. Adam, O. Zitka, *Nanomater. (Basel, Switzerland)* **2017**, *7*, 243.

[7] S. Mandal, K. Chaudhuri, *World J. Biol. Chem.* **2016**, *7*, 158–167.

[8] L. León Félix, B. Sanz, V. Sebastián, T. E. Torres, M. H. Sousa, J. A. H. Coaquira, M. R. Ibarra, G. F. Goya, *Sci. Rep.* **2019**, *9*, 4185.

[9] C. Zhou, Y. Bai, F. Yang, T. Sun, L. Zhang, Y. Cai, T. Gu, Y. Liu, M. Gong, D. Zhang, et al., *Mater. Chem. Front.* **2020**, *4*, 1614–1622.

[10] M. Xing, W. Xu, C. Dong, Y. Bai, J. Zeng, Y. Zhou, J. Zhang, Y. Yin, *Chem* **2018**, *4*, 1359–1372.

[11] S. J. Hibble, G. B. Wood, *J. Am. Chem. Soc.* **2004**, *126*, 959–965.

[12] C.-H. Lee, S. Lee, Y.-K. Lee, Y. C. Jung, Y.-I. Ko, D. C. Lee, H.-I. Joh, *ACS Catal.* **2018**, *8*, 5221–5227.

[13] H. Ye, L. Wang, S. Deng, X. Zeng, K. Nie, P. N. Duchesne, B. Wang, S. Liu, J. Zhou, F. Zhao, et al., *Adv. Energy Mater.* **2017**, *7*, 1601602.

[14] J. Goebl, Y. Liu, S. Wong, S. Zorba, Y. Yin, *Nanoscale Horizons* **2016**, *1*, 64–68.

[15] B. Ravel, M. Newville, *J. Synchrotron Radiat.* **2005**, *12*, 537–541.

[16] T. Daeneke, N. Dahr, P. Atkin, R. M. Clark, C. J. Harrison, R. Brkljača, N. Pillai, B. Y. Zhang, A. Zavabeti, S. J. Ippolito, et al., *ACS Nano* **2017**, *11*, 6782–6794.

[17] I. Bezverkhy, P. Afanasiev, M. Lacroix, *Inorg. Chem.* **2000**, *39*, 5416–5417.

[18] T. Weber, J. C. Muijsers, J. W. Niemantsverdriet, *J. Phys. Chem.* **1995**, *99*, 9194–9200.

[19] H. W. Wang, P. Skeldon, G. E. Thompson, G. C. Wood, *J. Mater. Sci. Lett.* **1996**, *15*, 494–496.

[20] E. K. Quagraine, I. Georgakaki, D. Coucouvanis, *J. Inorg. Biochem.* **2009**, *103*, 143–155.

[21] H. Ye, L. Ma, Y. Zhou, L. Wang, N. Han, F. Zhao, J. Deng, T. Wu, Y. Li, J. Lu, *Proc. Natl. Acad. Sci.* **2017**, *114*, 13091 LP – 13096.

[22] Y. Yin, J. Han, Y. Zhang, X. Zhang, P. Xu, Q. Yuan, L. Samad, X. Wang, Y. Wang, Z. Zhang, et al., *J. Am. Chem. Soc.* **2016**, *138*, 7965–7972.

[23] J. Gu, J. A. Aguiar, S. Ferrere, K. X. Steirer, Y. Yan, C. Xiao, J. L. Young, M. Al-Jassim, N. R. Neale, J. A. Turner, *Nat. Energy* **2017**, *2*, 16192.

[24] S. Shibata, T. Taniguchi, T. Yano, M. Yamane, *J. Sol-Gel Sci. Technol.* **1997**, *10*, 263–268.

[25] K. Chang, H. Pang, X. Hai, G. Zhao, H. Zhang, L. Shi, F. Ichihara, J. Ye, *Appl. Catal. B Environ.* **2018**, *232*, 446–453.

[26] R. Bjornsson, M. U. Delgado-Jaime, F. A. Lima, D. Sippel, J. Schlesier, T. Weyhermüller, O. Einsle, F. Neese, S. DeBeer, *Zeitschrift fur Anorg. und Allg. Chemie* **2015**, *641*, 65–71.

[27] D. Hara, H. Ikuta, Y. Uchimoto, M. Wakihara, *J. Mater. Chem.* **2002**, *12*, 2507–2512.

[28] V. N. Bakunin, M. Kasrai, G. N. Kuzmina, G. M. Bancroft, O. P. Parenago, *Tribol. Lett.* **2007**, *26*, 33–43.

Chapter 5. Future Work and Outlook

The past two decades have witnessed remarkable progress in engineering the responsive features in nanostructured materials, which was accompanied by the developments in nanomaterials synthesis, post-synthesis optimization and modifications, fabrication methodologies, and chemical functionalizations. That said, we believe there is still room for substantial developments in the field of stimuli-responsive nanomaterials, especially in performance optimization, enhancing the responsive capabilities and stability, and large-scale production.

For example, as shown in Chapter 2, although the rewritable system of N-TiO_2 has shown outstanding performance in comparison to the pristine TiO_2 system, the poor stability and short coloration lifespan are still significant concerns for deploying this technology in real-practical applications. We believe that these issues could resolve by extending the study of polyols surface modification to other alcohols. Beyond glycol molecules, longer chain polyols present a promising opportunity to tackle such problems. These molecules contain a higher degree of hydroxyl groups, which presumably will enhance the performance of the rewritable paper system by scavenging more h^+ and stabilizing more reduced sites of TiO_2. Additionally, we believe there is a tremendous potential direction in extending the coloration spectrum from only one color to a multi-color rewritable system. Such a system might be developed based on doping other metals in the TiO_2 structure, namely 3d orbitals transition metals such as Mn and Co.

For the project in Chapter 3, we believe that this system might also present some limitations by being only a one-color system. Therefore, we believe that the future

research of this project should focus on developing a multi-color system responding to various thresholds of pressure. An alloy system of Ag and Au, or Au and Cu, is worth exploring to accomplish different colors based on the ratio of each metal to metal during the alloying process. Also, the performance of the system in response to different force thresholds might improve by using more practical methods. Namely, utilizing the crystallization degree of TiO_2 shell by controlling the calcination temperature to tune the shell mechanical strength to uphold a certain measure of force. In this way, a more efficient and practical colorimetric pressure sensor could be developed that does not require precision synthetic methods to control the TiO_2 thickness.

Lastly, the universal magnetizing method described in Chapter 4 could also be utilized for future research, especially for magnetizing anisotropic nanostructures. For example, the properties and behavior of magnetic anisotropic nanomaterials have not been intensively studied before. Anisotropic structures with unique shapes such as nanobowl and nanocup, could provide a captivating interest if they could be magnetized. Their magnetic assemblies could endure unique features that might open the gate for further intriguing research. Also, we believe that the magnetically tunable micromirror could be fabricated with less expensive material other than Au. One example might worth trying is Mica (large silicate sheets), and because it is made of silicate, its surface modification with a-MoS_x will be straight-forward.

We believe that the outlook for engineering responsiveness in nanostructured materials will be mainly focused on adding more responsive features and enhancing the controllability of the materials' stimulation. We also think that the most promising field

for utilizing these materials is in bioimaging and drug delivery. Hence, the research of this field will focus more on developing more practical applications by developing more synthetic methods and functionalization techniques.